Towards the Fundamental Thermal Radiation Sensing Limit using Nanomechanical Resonators

Chang Zhang 张畅

A thesis submitted to the University of Ottawa
in partial fulfillment of the requirements for the degree of
Doctor of Philosophy in Mechanical Engineering

Department of Mechanical Engineering
Faculty of Engineering
University of Ottawa

献词/Dedication

谨以此文献给我挚爱的父母与妻子民智，

你们无私的爱，让这段旅程成为可能。

献给我的女儿 Leah，

你的到来如晨曦之初，赋予我生命以喜悦与方向。

To my mom, dad, and my wife Judy,

it is your unconditional love that made this work possible.

To my daughter Leah,

whose anticipated arrival fills my journey with joy and purpose.

Acknowledgment

I would like to express my deepest gratitude to my PhD supervisor, Dr. Raphael St-Gelais, for his guidance over the years. He not only instilled in me a passion for and appreciation of the scientific investigation, but more importantly, showed me what it means to lead a life of integrity, humility, and kindness.

I would also like to thank all of my past and present colleagues at the Micro and Nano Systems Lab at the University of Ottawa, especially my friend and colleague, Nikaya Snell. I am grateful for her pioneering work on the subject of temperature fluctuation noise, which laid the groundwork for my subsequent investigations.

Abstract

Temperature-sensitive nanomechanical resonators (NMRs) have been intensively investigated in recent years as promising alternatives to traditional electrical thermal radiation detectors. Unlike traditional electrical detectors which sense thermal radiation through temperature-dependent electrical effects, NMRs undergo thermally induced mechanical resonance frequency shifts upon absorbing thermal radiation. Relying on this mechanical sensing scheme, NMRs hold the promise of reaching the fundamental thermal sensing limit set by temperature fluctuation noise, due to their potential immunity to electrical Johnson–Nyquist noise—the primary limiting factor for traditional electrical detectors.

To date, proposed temperature-sensitive NMRs have primarily focused on optimizing the thermal aspects of the resonators, using methods such as suspending NMRs with ultra-thin structures (e.g., thin rods or tethers) to enhance thermal isolation. However, mechanical frequency noises originating from the ultra-small effective and thermal masses of these NMRs has not been prioritized in the design process or clearly understood in the context of thermal radiation sensing. Consequently, existing nanomechanical thermal detectors have systematically shown not to be limited by fundamental temperature fluctuation noise, nor have they demonstrated significant improvements over state-of-the-art traditional thermal detectors.

In this thesis, we first construct a model that incorporates common noise sources in temperature-sensitive NMRs while accounting for the filtering effects imposed by the closed-loop frequency tracking scheme (i.e., a phase-locked loop, PLL). During our preliminary experiments using SiN membrane NMRs, we observe signs that such NMRs can operate in a regime dominated by fundamental temperature fluctuation noise, but only within a very limited range of sampling frequencies. Later, through a more comprehensive series of experiments, we identify and correct inaccuracies in the initially proposed model. Additionally, this more recent work also unveils a crucial benefit of operating NMRs in a temperature fluctuation noise dominated regime. In particular, we experi-

mentally demonstrate that a hierarchically structured, high-Q-factor NMR can operate in the temperature fluctuation noise dominated regime over an unprecedented measurement bandwidth, thereby maintaining peak thermal sensing performance at faster sensing speeds (i.e., up to 30 times the thermal response time of the NMR).

Lastly, we functionalize a relatively large 3.2×3.2 mm square membrane NMR with a localized titanium metasurface absorber, targeting wavelengths ranging 0.5 to 3 terahertz. By striking a balance between frequency stability and thermal responsivity, we experimentally achieve a specific detectivity of $D^* \approx 3.4 \times 10^9$ cm $\cdot \sqrt{\text{Hz}}/\text{W}$ and a noise equivalent power NEP ≈ 36 pW$/\sqrt{\text{Hz}}$, which significantly outperforms the best commercial terahertz pyroelectric detectors. Despite non-idealities in our displacement readout interferometer, this experimentally achieved D^* is well within an order of magnitude of the fundamental thermal detectivity limit imposed by background photon fluctuations (i.e., $D^* \approx 1.8 \times 10^{10}$ cm $\cdot \sqrt{\text{Hz}}/\text{W}$). This work, therefore, creates a pathway to achieving the previously unattained fundamental thermal sensing limit at room temperature.

Contents

1 Introduction **1**

2 Literature Review **5**

2.1 Traditional thermal infrared detectors 6

2.1.1 Thermopiles 6

2.1.2 Pyroelectric detectors 12

2.1.3 Bolometers 16

2.2 Nanomechanical resonator (NMR)-based detectors 20

2.2.1 Resonators supported by thin rod 21

2.2.2 Beam resonators 22

2.2.3 Trampoline resonators 24

2.3 Performance comparison 25

3 Theoretical Background **27**

3.1 Lumped mechanical model 27

3.1.1 Free response 27

3.1.2 Forced response under harmonic excitation 29

3.1.3 Thermomechanical displacement noise 31

3.1.4 Thermomechanical frequency noise 34

3.2 2D continuum mechanical model 36

3.2.1 Effective mass 38

3.3 Dissipation mechanisms 39

3.3.1 Damping Dilution 40

3.4 Thermally induced resonance frequency shift 43

3.5 Lumped thermal model 47
3.6 2D continuum thermal model 50
3.7 Summary of important noise sources in temperature-sensitive nanomechanical resonators 53
3.7.1 Fundamental noise in thermal sensing 53
3.7.2 Non-fundamental noises in thermal sensing 54
3.7.3 Thermomechanical noise 54
3.7.4 Instrument readout noise 54
3.7.5 Critical amplitude for the onset of Duffing nonlinearity 55
3.7.6 Conversion between noise figure conventions 56
3.8 Noise filtering effect of closed-loop frequency tracking 57

4 Temperature Fluctuation Noise **60**
4.1 Article 1: Initial investigation of temperature fluctuation noise 60
4.1.1 Foreword 60
4.1.2 Author Contributions 61
4.1.3 Abstract 61
4.1.4 Introduction 62
4.1.5 Theory 64
4.1.6 Methods & Results 69
4.2 Article 2: Reaching temperature fluctuation dominated noise profile over an extended measurement bandwidth 77
4.2.1 Foreword 77
4.2.2 Author Contributions 78
4.2.3 Abstract 78
4.2.4 Introduction 79
4.2.5 Theory 80
4.2.6 Methods & Results 87

5 Terahertz sensing **97**

5.1 Article 3: Terahertz sensing 97

5.1.1 Foreword 97

5.1.2 Author Contributions 98

5.1.3 Abstract 98

5.1.4 Introduction 99

5.1.5 Theory 100

5.1.6 Methods & Results 106

6 Conclusions & Outlook **117**

A Supplementary for Article 1 **119**

A.1 Finding an optimum range of laser power 119

A.2 Fitting parameters for this study 121

B Supplementary for Article 2 **122**

B.1 Heat transfer simulation 122

B.2 Effective mass and temperature coefficient of fractional frequency shift simulation 123

B.3 Frequency fluctuation under varying probing laser power 124

C Supplementary for Article 3 **126**

C.1 Fractional frequency noise spectral density in angular frequency $S_y(\omega)$ 126

C.2 Transformation between fractional frequency noise spectral density $S_y(\omega)$ and Allan deviation σ_A 126

C.3 Scaling Noise Equivalent Power NEP parameters with SiN membrane resonator sizes 127

C.4 Defining the effective heat transfer area of SiN membrane resonator during terahertz absorption 128
C.5 Estimating thermal responsivity R under localized heating 130
C.6 Mechanical modes, Q-factors and demodulated signal amplitudes 131

List of Figures

2.1 Schematic of thermopile and thermocouple 6
2.2 Seebeck coefficient of silicon 8
2.3 Schematic of two dissimilar leads thermopile 8
2.4 Figure of merit for thermoelectric materials 10
2.5 Graphene thermopile 10
2.6 Carbon nanotube thermopile 11
2.7 Schematic of pyroelectric detectors 12
2.8 Schematic of pyroelectric detector's electrical readout circuit 13
2.9 Optimum voltage responsivity with respect to sampling time 14
2.10 Schematic of a thin-film bolometer 16
2.11 Temperature coefficient enhancement upon annealing 17
2.12 Temperature coefficient of resistance comparison 18
2.13 Schematics of a VOx bolometer 19
2.14 Existing NMRs 21
2.15 Beam resonator 22
2.16 Drum and trampoline resonator 24

3.1 1D lumped model 27
3.2 Mechanical susceptibility block diagram 30
3.3 Mechanical susceptibility plot 30
3.4 Simulated thermomechanical peaks 33
3.5 Displacement to phase noise in phase space 35
3.6 Mode shapes of a vibrating square membrane, generated using *Matplotlib* 37
3.7 1D fundamental mode shape with edge correction 42

3.8 NMR-based thermal sensing . . . 43
3.9 Mode shapes of a vibrating square vs. circular membrane, generated using *Matplotlib* . . . 45
3.10 Thermal block diagram . . . 47
3.11 Temperature fluctuation block diagram . . . 48
3.12 Schematics of SiN radiative heat transfer . . . 50
3.13 Block diagram for closed-loop frequency tracking scheme . . . 58

4.1 Additive phase noise vs. thermal fluctuation . . . 64
4.2 Effect of dimensions on heat transfer quantities in silicon nitride drum resonators . . . 67
4.3 Schematics of the experimental setup . . . 70
4.4 Theoretical Allan deviation for drive variation . . . 73
4.5 Experimental Allan deviation . . . 74
4.6 Frequency tracking setup schematics . . . 83
4.7 Critical intersection frequency . . . 86
4.8 General characterization of the resonator mechanical and thermal response 89
4.9 Frequency fluctuation measurements . . . 91
4.10 Thermal responsivity measurement . . . 93
4.11 Enhanced NEP and D^* bandwidth . . . 95

5.1 Thermal sensing performance simulation . . . 104
5.2 Localized THz absorber . . . 108
5.3 THz detection experimental setup . . . 109
5.4 THz experiential results . . . 112
5.5 Verifying THz detector linearity . . . 114
5.6 Verifying THz detector linearity V.2 . . . 115

A.1 Experimental Allan deviation under laser power change . . . 120

B.1 Heat transfer simulation under uniform heating 122
B.2 Mechanical mode shape 123
B.3 Laser power variation 124

C.1 Localized heat transfer 128

1. Introduction

Traditional thermal-based detectors such as thermopiles, bolometers and pyroelectric detectors are the industry-standard technologies for detecting thermal infrared radiation (i.e., mid to far infrared wavelengths). They primarily rely on electrical sensing schemes, in which the temperature variation of the sensing element upon exposure to incident radiation is inferred via the temperature-dependent electrical properties of the material. For instance, bolometers use sensing element materials that exhibit a change in electrical resistance in response to temperature variations, whereas pyroelectric detectors use materials that undergo a change in electrical polarization due to temperature variations.

Detectors that leverage temperature-dependent electrical properties during thermal sensing are typically limited by Johnson-Nyquist noise, mainly originating from their use of electrical readout [1–4]. This limitation typically places their specific detectivity D^* one to two orders of magnitude below the fundamental limit of a blackbody thermal-based detector at room temperature (i.e., $D^* \approx 1.8 \times 10^{10}$ cm $\cdot \sqrt{\text{Hz}}/\text{W}$).

In theory, this fundamental D^* limit can be reached when three key conditions are simultaneously fulfilled [2, 3, 5]:

1. The total thermal conductance G (in units of W/K) of the detector sensing element with the surrounding environment is solely due to radiative heat transfer G_{rad} (i.e., solid-state conduction and convection are negligible).

2. The detector sensing element absorbs thermal radiation as a blackbody (i.e., its total hemispherical emissivity is $\varepsilon = 1$).

3. The detector's noise profile is solely limited by fundamental temperature fluctuation noise, originating from random thermal exchanges between the detector's sensing element and its surrounding thermal bath.

Although conditions 1) and 2), which are associated with the thermal aspect alone, can be engineered with current technology, condition 3) — achieving a thermal fluctuation-dominated noise profile — has remained infeasible for traditional thermal-based detectors, since Johnson-Nyquist noise is typically the dominant noise source when using the electrical sensing scheme. To address this issue, developing a detector that does not rely on the thermal-electric sensing scheme, and is thus immune to Johnson-Nyquist noise, could significantly outperform traditional thermal-based detectors. Nanomechanical resonators (NMRs) represent a promising technology to fill this gap and are therefore the focus of investigation in this thesis.

Nanomechanical resonators (NMRs) [6–10], have gathered significant interest in various physical sensing applications such as mass [11–15], force [7, 16–18], pressure [19–21], quantum sensing [8, 22, 23]. These NMRs, when placed in a high-vacuum environment, exhibit ultra-narrow linewidth mechanical resonance (i.e., ultra-low mechanical dissipation leads to high Q-factor). By relating external physical perturbations (e.g., mass, force, pressure, temperature) of interest to shifts in mechanical resonance frequency, one can perform physical sensing.

In recent years, temperature-sensitive nanomechanical resonators [24–34] have been investigated extensively as a promising alternative to traditional thermal-based detectors. Unlike traditional thermal-based detectors that rely on thermally induced variations in electrical properties, temperature-sensitive nanomechanical resonators undergo thermally-induced stress variation when absorbing incident radiation, causing a shift in mechanical resonance frequency that can be used to infer the intensity of the incident radiation. With this unique mechanical resonant sensing scheme, NMRs can theoretically reach the temperature fluctuation-dominated noise profile in the absence of Johnson-Nyquist noise when using an optical readout, thereby creating a pathway to reach the fundamental D^* limit. Nevertheless, so far, the performance of existing NMR-based thermal detectors has not shown significant improvement in D^* over state-of-the-art

traditional thermal-based detectors. This underperformance may stem from existing NMR-based thermal detectors prioritizing the optimization of the thermal characteristics of sensing elements (i.e., NMRs), while the mechanical frequency stability of the resonators remains poorly understood and has therefore not been adequately considered in the design.

Although Johnson-Nyquist noise can be feasibly eliminated when using NMRs in conjunction with an optical readout, NMRs are found to be susceptible to a different regime of non-fundamental noise sources. These sources of noise are typically associated with the ultra-small mass nature of the NMRs such as adsorption-desorption, surface diffusion, and thermomechanical noises [35–47]. Among them, thermomechanical noise is typically the fundamental limit for sensing performance in applications such as mass and force sensing [13, 14, 17]. This noise causes random vibrations across all eigenmodes of NMRs following the equipartition theorem due to ambient thermal energy [6, 35, 36]. In recent years, a series of theoretical and experimental works have demonstrated string NMRs made of silicon nitride (SiN) reaching a noise profile limited by thermomechanical noise [38–40, 48, 49] using various frequency tracking methods such as feedback-free, phase-lock loop and self-sustained oscillator frequency tracking. Temperature fluctuation noise, despite being the fundamental limiting noise for thermal-based sensing application and theoretically well-documented in some gold-standard literature in the field of NMRs [36, 37], still lacks the experimental demonstration as the dominant noise source in any existing NMRs.

A recent study from our group (Snell *et al.* [5]) theoretically predicts that temperature fluctuation noise can exceed thermomechanical noise by an order of magnitude for high-Q SiN membrane resonators. Note that these SiN membrane resonators have been investigated extensively in recent years for thermal radiation sensing [25, 27, 33, 50, 51]. This previous work [5], however, does not experimentally demonstrate that temperature fluctuation being the dominant noise source, nor does it model the closed-loop filtering

effect imposed by the PLL on temperature fluctuation.

Building upon our earlier work on radiative heat transfer [33, 50] and on intrinsic frequency noise [5] in temperature-sensitive SiN membrane resonators, the ultimate goal of this thesis is to achieve significant performance gain over the existing NMR-based thermal detectors proposed over the years. Here, we seek to emphasize on frequency noise optimization in the design process. Specifically, by thoroughly investigating commonly encountered noises in temperature-sensitive, high Q-factor NMRs, namely temperature fluctuation, thermomechanical, and instrument readout noises.

The realization of the **ultimate goal of meaningfully improving NMR-based detectors thermal sensing performance** involves a series of intermediate goals that together constitute the body of work of this thesis. Here, the intermediate objectives are:

1. Model temperature fluctuation noise along with other commonly encountered non-fundamental noise sources, while accounting for the filtering effects of the closed-loop frequency tracking scheme.

2. Experimentally demonstrate that temperature fluctuation noise can be the dominant noise in temperature-sensitive nanomechanical resonators.

3. Achieve high-detectivity thermal radiation sensing.

Upon the completion of this thesis, **Objective 1** is achieved in **Chapters 4.1 and 4.2**; **Objective 2** is also achieved in **Chapters 4.1 and 4.2**; and **Objective 3** is achieved in **Chapters 4.2 and 5**.

2. Literature Review

In this chapter, we present a comprehensive literature review divided into two parts, each essential for understanding the fundamentals needed to achieve breakthrough thermal sensing performance with NMRs. First, we explore commonly used thermal infrared sensing technologies (i.e., thermopiles, bolometers, pyroelectric detectors) that utilize traditional electrical thermal sensing. Second, we review existing temperature-sensitive NMRs that leverage mechanical resonant sensing for infrared sensing. In the end, we provide a comprehensive comparison between state-of-the-art traditional electrical detectors and NMR-based detectors. A performance benchmark table for various thermal detectors can be found at the end of the chapter (see Table 2.1).

Note that in the ultra-far infrared (i.e., the THz wavelength range), coherent detection methods such as electro-optic sampling [52, 53], photoconductive antennas [54, 55], and nonlinear up-conversion [56] exist; however, they are beyond the scope of this thesis, which focuses on incoherent power detection, and are therefore not included in this literature review. In addition, many coherent detection methods employ different figures of merit (e.g., minimum detectable electric field), whereas incoherent power detection is characterized by minimum detectable power. Consequently, their performances are difficult to compare directly.

2.1 Traditional thermal infrared detectors

2.1.1 Thermopiles

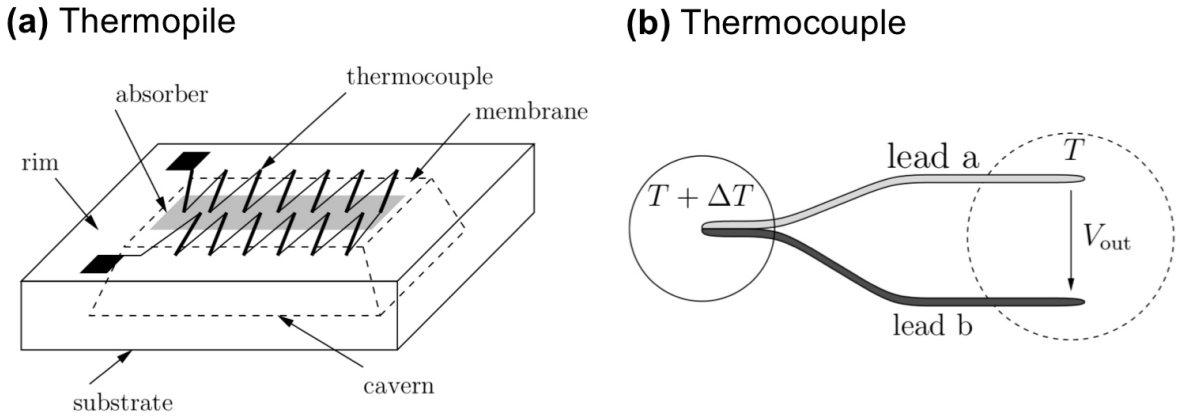

Figure 2.1: (a) Schematic of a bulk micromachined thermopile with anisotropically etched membrane. (b) Schematic of a single thermocouple [57].

The thermopile is commonly regarded as the oldest type of thermal radiation sensing technology, with its invention dating back to the discovery of the Seebeck effect [58, 59]– i.e., voltage generation caused by a temperature gradient at the junction of two distinct conductive materials. Leveraging this effect, the most fundamental element of a thermopile, the thermocouple, can be constructed simply by joining two different conductive materials at a junction [see Fig. 2.1(b)]. However, the Seebeck coefficients are typically on the order of μV/K for most well-studied conductive materials, leading to minuscule voltage signal outputs, making it impractical to use only a single thermocouple for most thermal radiation sensing applications. To improve sensing performance, thermopiles are constructed by connecting multiple thermocouples in series, as shown in Fig. 2.1(a), to generate a significantly higher voltage signal upon the occurrence of a temperature gradient. Typical thermopiles exhibit temperature sensitivity (i.e., Seebeck coefficient) on the orders of tens of mV/K [60, 61]. In this case, thermopiles inherently exhibit far

higher thermal sensitivity than a single thermocouple and are sufficiently capable for many practical thermal radiation sensing applications [57, 62].

It should be noted that although connecting multiple thermocouples increases the voltage signal output at a given temperature gradient (i.e., increases thermal responsivity), this method also increases the total electrical resistance of the thermopile, which in turn results in a higher level of Johnson-Nyquist noise [2, 3, 63].

2.1.1.1 Thermoelectric properties of semiconductors

Modern thermopiles are typically made of semiconductors such as single-crystal silicon and poly-silicon due to their relatively high Seebeck coefficients [64, 65] and the ease with which they can be fabricated using standard micro- and nanofabrication processes [3, 66, 67]. In comparison, metallic materials exhibit Seebeck coefficients that are one to two orders of magnitude lower [60, 68], leading to inferior thermal sensing performance. In addition, the Seebeck coefficients of semiconductors exhibit less unwanted temperature dependency [60,61,64], meaning that semiconductor thermopiles can be calibrated to operate linearly over a broader temperature range. Another major advantage of semiconductor-based thermopiles is that the Seebeck coefficient of the semiconductor material can be easily engineered by altering its doping concentration [see Fig. (2.2)] (e.g., a high doping concentration level leads to a low electric resistivity and also a low Seebeck coefficient). Doping is the process of adding impurities to silicon during its growth. The most common types of doped silicon used for constructing thermopiles are n-type (i.e., doped with phosphorus or arsenic) and p-type (i.e., doped with boron or gallium).

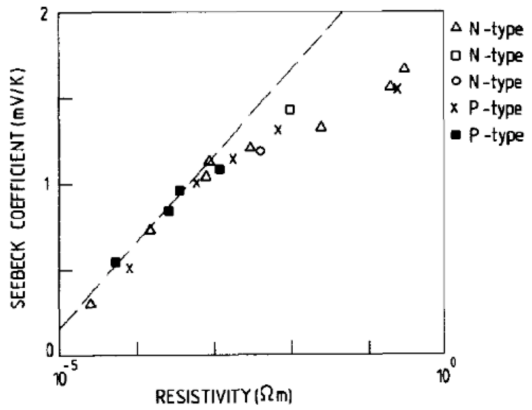

Figure 2.2: Seebeck coefficients as a function of resistivity for multiple types of doped mono-crystalline silicon at 300 K. Different symbols for the same type of doped silicon (e.g., N-type or P-type) represent different types of dopants. The detailed information of the dopant material is not given in the paper [61].

2.1.1.2 Design considerations

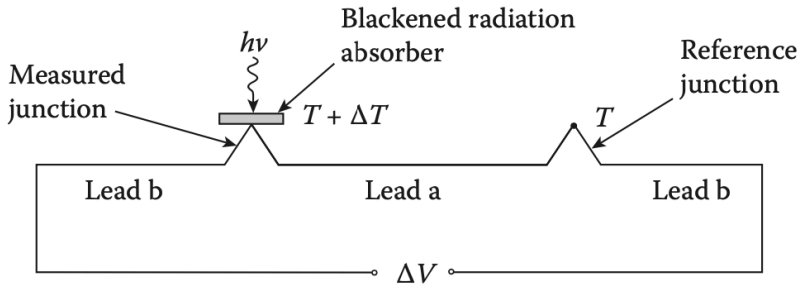

Figure 2.3: Schematic of two dissimilar leads thermopile [3].

Thermal stability is one of the major design considerations for a thermopile to operate in its desired state by maintaining a stable temperature gradient ΔT between the measured junction (i.e., the hot junction) and the reference junction (i.e., the cold junction) so that the thermopile can produce a stable voltage readout. To achieve this, the reference junction must be highly insulated from its environment to ensure its temperature remains unchanged during the measurement. As shown in Fig. (2.3), the conductor 'Lead A' connects the measured junction and the reference junction. Due to solid-state conduction, heat flux transfers from the hot junction to the cold junction, gradually leveling the temperature gradient over time. This transient heat transfer causes instability

and inaccuracy during measurement. To address this issue, modern thermopiles are made of poly-silicon, which has low thermal conductivity, minimizing changes in the temperature gradient during measurement. Meanwhile, the absorbing panel connected to the measured junction aims for high emissivity and low heat capacity to ensure the measured junction is thermally well-coupled to the sensing object via radiation and achieves a fast thermal response.

Another major design consideration involves balancing the trade-off between achieving high thermal responsivity and minimizing Johnson-Nyquist noise. On one hand, the junction materials should have low electrical resistance to reduce Johnson-Nyquist noise. On the other hand, low-resistance materials typically exhibit a low Seebeck coefficient [see Fig. (2.4)], as the Seebeck coefficient and resistivity are inversely proportional, which in turn leads to low thermal responsivity. To address this well-known trade-off in thermopiles, a commonly used figure of merit for thermopiles constructed with dual-material thermocouples (i.e., material a and b) is defined as Eq. (2.1) [2]:

$$Z = \frac{(\alpha_a - \alpha_b)^2}{\sqrt{\rho_a G_a} + \sqrt{\rho_b G_b}}, \tag{2.1}$$

where α_a and α_b are the Seebeck coefficients (μV/K), ρ_a and ρ_b are the electric resistivities ($\Omega \cdot$ m), and G_a and G_b are the thermal conductances (W/K). Note that total thermal conductance for a typical thermopile shall consider all schemes of heat transfer which include radiative, convective and solid-state conductive heat transfers.

As shown in Fig. (2.4) that semiconductors typically exhibit the highest Z value, making them inherently more suitable for use in thermopiles than metals and other materials.

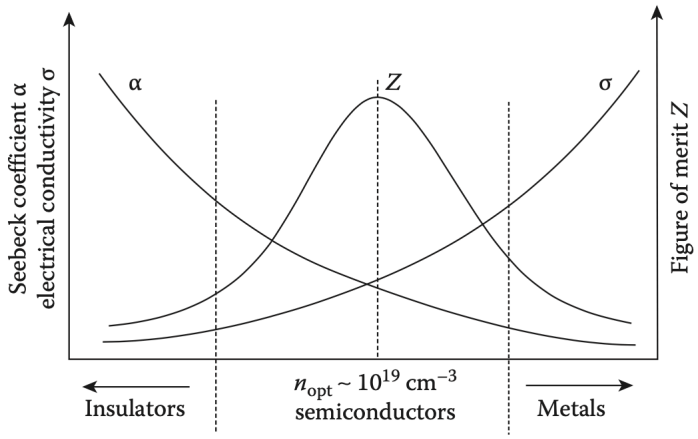

Figure 2.4: Figure of merit for thermoelectric materials. [69].

2.1.1.3 State-of-the-art

Due to the rapid development of semiconductor and nanotechnology, thermopiles made from novel two-dimensional materials such as graphene [70] and carbon nanotubes [71] have been proposed as a proof of concept, which could further drive the advancement of this previously stalled technology.

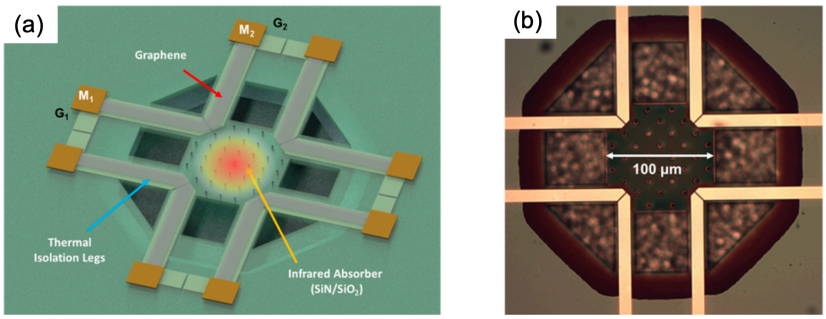

Figure 2.5: (a) Schematic of graphene thermopile. (b) Optical micrograph of the completed device [70].

Despite the low intrinsic Seebeck coefficient exhibited by pure graphene, processes such as doping and straining have been shown to enhance graphene' s Seebeck coefficient to a level surpassing that of single-crystal silicon and poly-silicon [70, 72–74]. A more obvious advantage of graphene-based thermopiles is leveraging the ultra-high thermal resistance (compared to conventional silicon-based materials due to ultra thin profile)

of single-layer graphene [75], which significantly enhances thermal isolation and, consequently, the thermal responsivity of the thermopile. Based on these inherent advantages, device shown in Fig. 2.5 [70] achieves peak detectivity $D^* \approx 8 \times 10^8$ cm $\cdot \sqrt{\text{Hz}}/\text{W}$ in the wavelength range of $5 - 15$ μm.

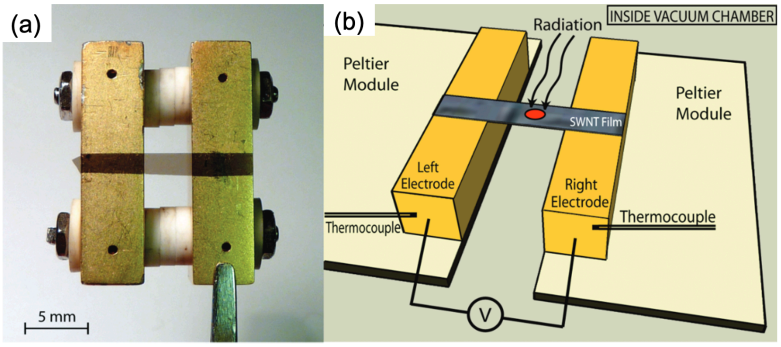

Figure 2.6: (a) Picture of the thin-film nanotube thermopile. (b) Schematics of the experimental setup. [71].

Carbon nanotubes also attract considerable interest for use in constructing thermopiles due to their inherent strong absorption in the mid- to far-infrared range. However, due to their high thermal conductivity and relatively low Seebeck coefficient (i.e., tens of μV/K), achieving high thermal responsivity with such materials has proven to be more difficult than with conventional silicon-based materials or graphene. Therefore, carbon nanotube-based thermopile shown in Fig. 2.6 are proposed more as a proof of concept with inferior performance (i.e., $D^* \approx 2 \times 10^6$ cm $\cdot \sqrt{\text{Hz}}/\text{W}$ [71]). A more recent thermal sensing characterization of the carbon nanotube thermopile [76] using a focused laser beam has not shown significant improvement in D^*.

2.1.2 Pyroelectric detectors

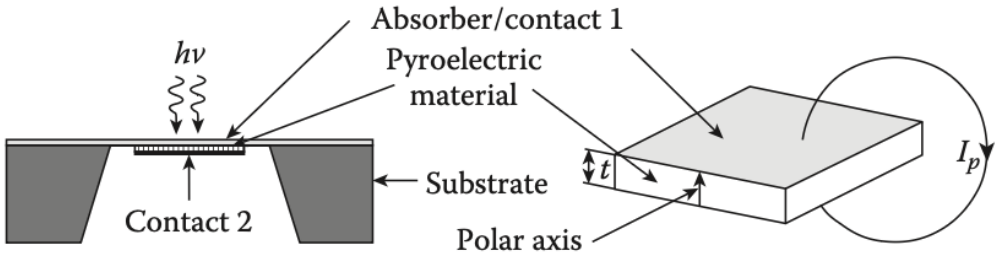

Figure 2.7: Schematic of pyroelectric detectors. [3].

Pyroelectric detectors utilize materials that exhibit spontaneous electrical polarization changes in response to temperature variation (i.e., the pyroelectric effect) upon incident thermal radiation [77, 78]. Such change in polarization in turn induces a displacement current I_p as shown in Fig. 2.7, that can be collected via a external readout circuit. Note that I_p can be calculate as:

$$I_p = A_{pyro} p \frac{dT}{dt}, \tag{2.2}$$

where A_{pyro} is the absorbing area of the pyroelectric material, p is the pyroelectric coefficient which represents the polarization change due to temperature variation and dT/dt is the rate of change of temperature with respect to time. From Eq. 2.2, we can immediately notice the fundamental distinction between a thermopile and a pyroelectric detector. Unlike a thermopile, which is able to produce an electrical signal in the presence of continuous thermal radiation, a pyroelectric detector only generates an electrical signal in response to changes in temperature over time dT/dt [79]. This means that one must modulate the source of incoming radiation to leverage the pyroelectric effect which is typically done by using a mechanical chopper.

2.1.2.1 Design consideration

Unlike thermopiles and bolometers, where the thermally induced voltage signal can be easily read out, pyroelectric detectors generate a faint displacement current upon spontaneous temperature changes, making efficient capture of the electrical signal significantly more difficult [80]. As a result, the construction of the readout circuit plays a crucial role in pyroelectric detector's thermal sensing performance.

A typical electrical readout configuration for pyroelectric detector which uses a junction field effect transistor (JFET) amplifier is presented in Fig. 2.8, where the pyroelectric material is modelled as an electrical capacitor C. A key consideration when constructing such a JFET amplifier for a pyroelectric detector is that the shunt resistor G^{-1} must be sufficiently large (i.e., typically $> 10^{11}$ ohms [81, 82]) to convert the minuscule current generated by the pyroelectric material to a sizable voltage output V_o.

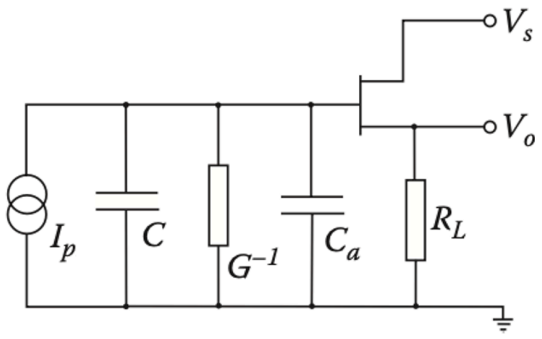

Figure 2.8: Schematic of pyroelectric detector's electrical readout circuit. [3].

It is worth noting that during thermal radiation sensing, both the electric time constant τ_e of the circuit shown in Fig. 2.8 and the thermal time constant τ_{th} of the pyroelectric material concurrently affect the voltage responsivity $\mathcal{R}_v$ of this system. This dual-time constant influence on responsivity is formalized as [3, 81, 82]:

$$\mathcal{R}_v(\omega) = \frac{R_e R_{th} \varepsilon p A_{pyro} \omega}{(1+\omega^2\tau_{th}^2)^{1/2}(1+\omega^2\tau_e^2)^{1/2}}, \tag{2.3}$$

where R_e is the equivalent electrical resistance of the circuit, R_{th} is the equivalent thermal

resistance of the system, ε is the total hemispherical emissivity of the absorber.

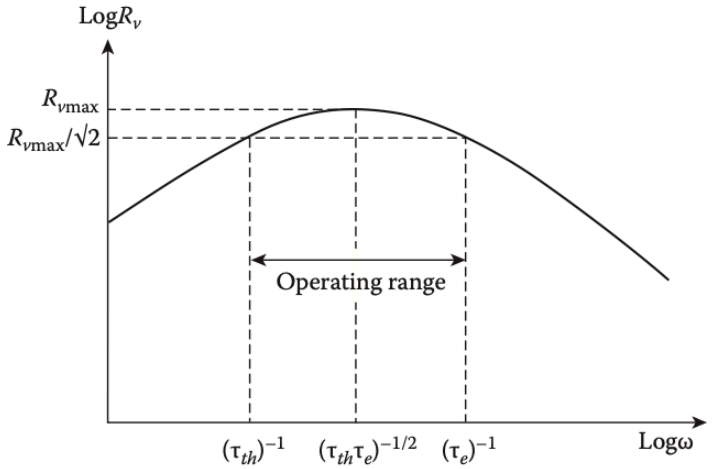

Figure 2.9: Optimum voltage responsivity with respect to sampling time [3].

A graphical representation of Eq. 2.3 is shown in Fig. 2.9 from which we note that the optimum sampling time of a pyroelectric detector occurs at $(\tau_e\tau_{th})^{-1/2}$. Furthermore, the maximum value of R_v can be calculate as:

$$\mathcal{R}_{vmax} = \frac{R_e R_{th}\varepsilon p A_{pyro}}{\tau_e + \tau_{th}}. \tag{2.4}$$

Typically, modern systems utilize thin-film pyroelectric materials in which their electrical time constants are much larger than their thermal time constant (i.e., $\tau_e \gg \tau_{th}$). As a result, for thin-film pyroelectric materials, their peak responsivity can be approximated as [81–84]:

$$\mathcal{R}_{vmax} \cong \frac{R_{th}\varepsilon p t_{pyro}}{\varepsilon_0\varepsilon_r}, \tag{2.5}$$

where ε_0 and ε_r are respectively the vacuum permittivity and the relative permittivity of the pyroelectric material, and t_{pyro} is the thickness of the material.

Due to the AC measurement scheme and the need for an amplifier in the readout circuit, pyroelectric detectors are subject to electrical noise in different forms [85], as is the case with other thermal-based detectors (i.e., bolometers and thermopiles) while Johnson-

Nyquist noise remains dominant. In specific, the Johnson-Nyquist noise is divided into two regimes: when sampling τ is much greater than the electric time constant τ_e of the system, noise is generated mainly due to the shunt resistance, whereas when $\tau \ll \tau_e$, AC noise originating from the capacitive nature of the pyroelectric material dominates. Pyroelectric detectors made of thin-film material [2,3,81], mainly experience noise of the later regime (i.e., $\tau \ll \tau_e$). In such case, the AC Johnson-Nyquist noise V_j is proportional to $\tan\delta/C$ where $\tan\delta$ is the loss tangent of the pyroelectric material and the pyroelectric material electric capacitance is $\varepsilon_0\varepsilon_r A_{pyro}/t_{pyro}$. Here, note that in an effort of minimizing the noise, material with large ε_r is more desirable, however doing so will sacrifice the responsivity as larger ε_r translates to a lower $\mathcal{R}_{vmax}$ as shown in Eq. 2.5.

2.1.2.2 State-of-the-art

The most popular choices of pyroelectric materials for thermal radiation sensing are single crystals such as triglycine sulfate (TGS) [86], lithium tantalate ($LiTaO_3$) [87], lead titanate ($PbTiO_3$) [88] and etc. Among these, detectors made of derivate L-alanine-doped deuterated TGS (DLaTGS) exhibit the highest pyroelectric coefficient [89], where the addition of deuterium significantly increases the linearity of the pyroelectric coefficient over a wider temperature range, and therefore the highest thermal radiation sensing performance in mid to far infrared (i.e., $D^* \approx 1 \times 10^9$ cm $\cdot \sqrt{\text{Hz}}/\text{W}$ [3, 90, 91]).

The inherent infrared absorption typically ranges from 8 μm $-$ 14 μm, therefore to broaden the spectral absorption to cover the entire mid-to-far infrared, gold-black coatings are typically applied to achieve this [92]. Recent academic works reported on pyroelectric detector, instead of focusing on improving the D^* over the existing market-available detectors [90, 91], they primarily focus on making pyroelectric detection spectrally more selective [93–96]. The highest D^* reported among these recent works is $\approx 1 \times 10^7$ cm $\cdot \sqrt{\text{Hz}}/\text{W}$ [96], which is two orders of magnitude lower than the state-of-the-art commercial systems.

2.1.3 Bolometers

Bolometer [97], as one of the oldest instrument for detecting thermal radiation was first invented in 1878 by American astronomer and physicist Samuel Langley. In his 1880 paper [98], Langley demonstrated the measurement of thermal radiation from the flame of a petroleum lamp using thin gold and iron strips. Upon absorbing the radiation, these metal strips exhibit changes in electrical resistance, which can then be read out using a standard Wheatstone bridge circuit. Moving forward, in 1961, American physicist Dr. Frank J. Low invented the gallium-doped germanium bolometer, which operates at cryogenic temperatures using liquid helium (i.e., 2 K). This cryogenic bolometer, still the best-performing commercially available detector for the mid-to-far infrared (i.e., $D^* \approx 1 \times 10^{11}$ cm $\mathrm{Hz}^{1/2}\mathrm{W}^{-1}$ [99, 100]), practically gave birth to the field of infrared astronomy by allowing scientists to observe faint radiation from outer space. In 1967, Dr. Low founded the company Infrared Laboratory (IRLabs [100]), which successfully commercialized the cryogenic bolometer and continues to serve the infrared community to this day. On May 2nd, 2024, I had the honor of visiting IRLabs in person to discuss the recent advancements in thermal radiation sensing.

2.1.3.1 Design considerations

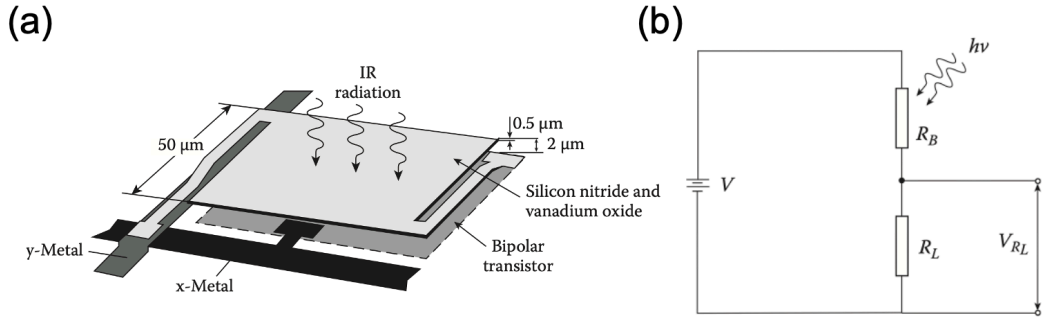

Figure 2.10: (a) Schematic of a thin-film bolometer [101]. (b) Equivalent electrical circuit of a typical bolometer [2, 3].

The most fundamental quantity that dictates the sensing performance of a bolometer is the fractional temperature coefficient of resistance α_r of the material in 1/K, which is defined as the relative resistance change per Kelvin temperature difference. Modern bolometers [see Fig. 2.10(a)] are typically made of thin-film vanadium oxide (VO_x) [102, 103] and amorphous silicon (aSi) [104, 105] rather than metals, due to their high temperature coefficient of resistance at room temperature. Furthermore, thin-film metal exhibits high thermal expansion coefficient, therefore introducing nonlinearity in α_r during temperature change which harms its stability during thermal sensing application [106]. So far, annealed VO_x is the most ideal sensing element for constructing a room-temperature bolometer, achieving a α_r value between 2% and 3% [3, 102], while maintaining excellent stability over a wide temperature range, as shown in Fig. 2.11. Note that the value of α_r for VO_x is typically one order of magnitude above thin-film metal of any kind [106].

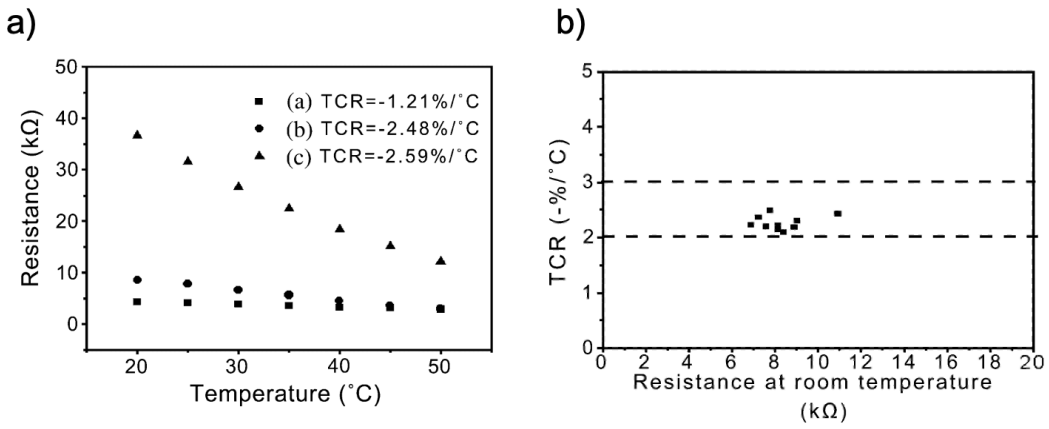

Figure 2.11: (a) Increasing temperature coefficient of VO_x through different level of annealing. (b) Measured temperature coefficients for various annealed VO_x sample. [102]

The simplest electrical readout circuit of a bolometer is illustrated as shown in Fig. 2.10(b), which primary consists of three major parts: a voltage source, a bolometer sensing element R_B (e.g., metal, silicon,VO_x, etc.) and a load resistance R_L. Note that typically R_L is much larger than R_B, which limits the magnitude of the bias current, pre-

venting the sensing material from getting damaged. The use of a large R_L also amplifies the voltage difference signal during thermal sensing. In this simplest configuration without considering joule heating due to bias current, the voltage responsivity of a bolometer can be calculated as:

$$\mathcal{R}_v \cong \frac{I\alpha_r R_e R_{th}\varepsilon}{\sqrt{1+\omega^2\tau_{th}^2}}, \tag{2.6}$$

which is in a similar form to the responsivity described in Eq. 2.3 for pyroelectric detectors, with the main difference being that it is only affected by the intrinsic thermal time constant τ_{th} of the bolometer sensing element, unlike pyroelectric detectors, which are affected by both τ_{th} and τ_e. According to Eq. 2.6, using a sensing element that has high electrical and thermal resistance is desirable for improving the responsivity. However, the electrical Johnson Nyquist noise $V_J = \sqrt{4k_B T R_e \Delta f}$, where k_B is the boltzmann constant and Δf is the measurement bandwidth, also scales with the total electrical resistance R_e of the bolometer. Therefore, optimizing $\mathcal{R}_v$ leads to an increase in V_J, which causes highly sensitive bolometers to be primary limited by electrical Johnson Nyquist noise.

2.1.3.2 State-of-the-art

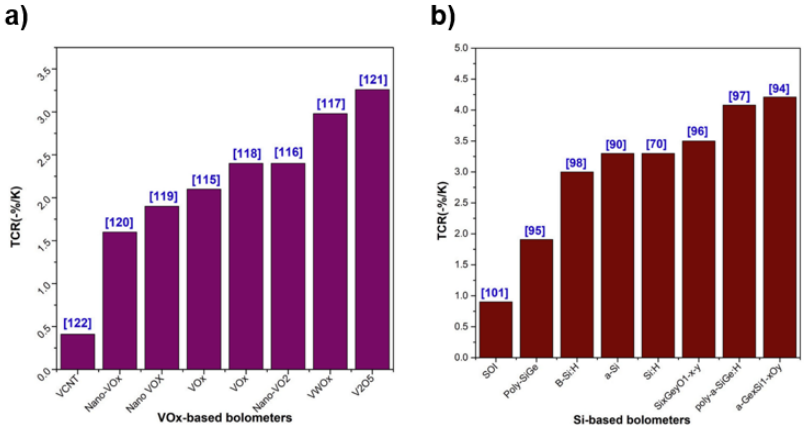

Figure 2.12: (a) Comparison of TCR values of various VO_x materials. (b) Comparison of TCR values of various Si-based materials [107].

Tabulated in Fig. 2.12 are temperature coefficients α_r of recently reported silicon-based and VO_x-based sensing material which ranges from 2% to 4%. This shows the difficulty of gaining thermal sensing performance by boosting α_r, as the values are largely similar. As suggested by Eq. 2.6, optimizing the infrared absorption ε and the thermal resistance R_{th} could result in more performance improvement. For instance, Fig. 2.13 [108] illustrates a high-detectivity vanadium oxide-based bolometer, achieving a D^* of $\approx 6{\times}10^8$ cm $\cdot \sqrt{\text{Hz}}/\text{W}$ by boosting the absorption of the sensing element. This VO_x-based bolometer utilizes a gold black absorbing layer, along with a gold back reflector which improves the absorption in mid infrared wavelengths (i.e., $8{-}14$ μm) by roughly a factor of two compared to a regular vanadium bolometer. Renoux *et al.* [109] demonstrated using a ultra-thin platinum wire (i.e., 4 μm by 300 nm) to maximize R_{th} therefore achieving high performance (i.e., $D^* \approx 1 \times 10^9$ cm $\cdot \sqrt{\text{Hz}}/\text{W}$). However, such thin platinum wire bolometer is practically not usable due to its sub-wavelength size. Commercially available bolometers typically achieve $D^* \approx 2 \times 10^8$ cm $\cdot \sqrt{\text{Hz}}/\text{W}$ at room temperature [110].

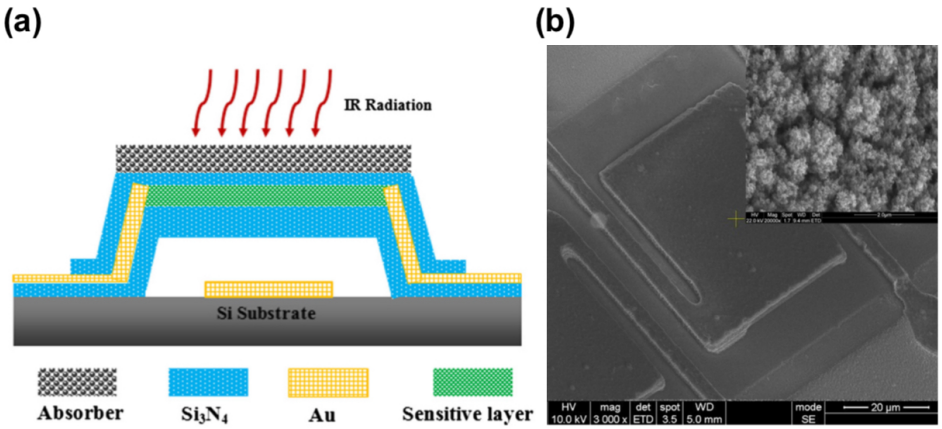

Figure 2.13: (a) Schematic for a VO_x-based bolometer with gold black absorber and a gold reflector. (b) SEM image of the bolometer top view [108].

2.2 Nanomechanical resonator (NMR)-based detectors

As we discussed in Section. 2.1, the electrical thermal-based detectors (i.e., thermopile, pyroelectric detector and bolometer) that rely on the electrical sensing schemes are typically limited by electrical Johnson-Nyquist noise at room temperature, which constrains the state-of-the-art detectivity D^* to between 1×10^8 cm $\cdot \sqrt{\text{Hz}}/\text{W}$ and 1×10^9 cm $\cdot \sqrt{\text{Hz}}/\text{W}$. To further improve performance beyond traditional thermal-based detectors, a sensing approach that deviates from conventional electrical sensing is needed. A torsional nanomechanical resonator (NMR)-based detector was reported in 2013 [26], marking one of the earliest efforts in the development of NMR-based thermal detectors. Unlike traditional thermal-based detectors that use electrical sensing, this type of detector utilizes a mechanical resonator's temperature-sensitive mechanical resonance frequency to measure incoming thermal radiation (see Section. 3.4 for detailed theoretical background). This mechanical sensing approach could potentially overcome the limitations imposed by electrical thermal sensing, therefore attracting interest of the NMR community. In this section, we aim to provide a comprehensive overview of important NMR-based thermal detector research conducted over the past decade.

2.2.1 Resonators supported by thin rod

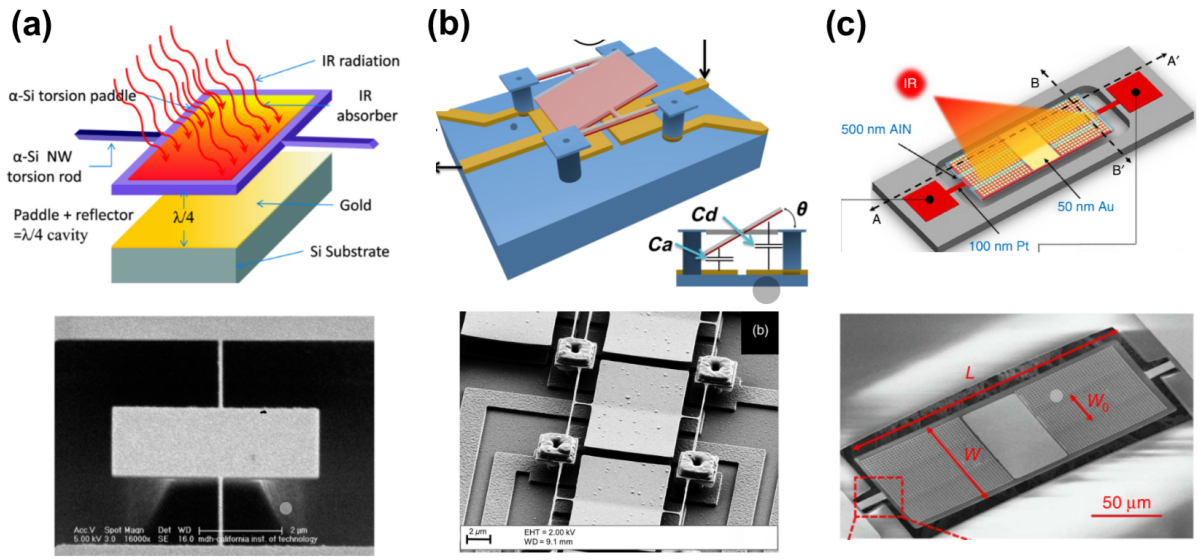

Figure 2.14: (a) Silicon nitride (SiN) sensing panel coated with titanium nitride (TiN) film and supported by thin rod made of amorphous silicon. A gold reflector located at quarter wavelength [26]. (b) Same material choices of sensing panel, absorbing layer and back reflector as in (a), with differences being the "H shape" thin-rod supporting structure and a larger sensing panel [24]. (c) Aluminum nitride (AlN) sensing panel coated with plasmonic metasurfaces made of gold and supported by platinum (Pt) tether [28].

Leveraging the conventional knowledge of thermal-based sensing, nanomechanical resonators (NMRs) shown in Fig. 2.14 all utilize thin rod or tether like supporting structure to suspend the sensing panel in order to achieve optimum thermal isolation, therefore boosting the thermal responsivity towards incident infrared radiation. Furthermore, designs shown in Fig. 2.14(a) [26] and (b) [24] both functionalized a TiN absorbing layer and an impedance-matching back reflector located at a quarter wavelength, resulting in an absorption efficiency close to 100% in the mid-to-far infrared range (i.e., 8 to 14 μm). Whereas Fig. 2.14(c) [28] implemented a metasurface absorbing layer, selectively targeting wavelengths centered around 8.8 μm.

During operation, the sensing panels exhibit two modes of vibration, namely torsional and flexural, depending on the actuation frequency. These two modes of vibration in-

terestingly show different temperature coefficient of fractional frequency shift α in 1/K, reported in [26]. Despite the implementation of different readout methods (i.e., capacitive [24], piezoelectric [28] and laser interferometric [26] readouts), NMR-based devices in Fig. 2.14 exhibit similar level of thermal sensing performance in terms of D^*, in which Laurent *et al.* [24] achieves the highest $D^* \approx 4.4 \times 10^7$ cm $\cdot \sqrt{\text{Hz}}/\text{W}$. The characteristic sizes $\sqrt{A_d}$ of the sensing elements for these devices range from 3 μm [26] to 12 μm [24] to 120 μm [28]. These devices supported by thin rod/tether [24,26,28] represent the earliest design style that attracted significant attention for NMR-based thermal detectors.

2.2.2 Beam resonators

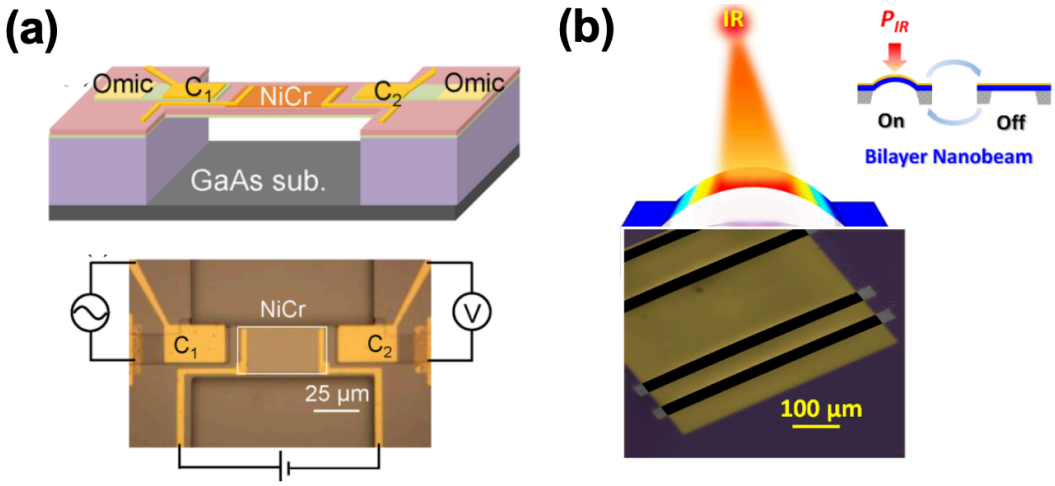

Figure 2.15: (a) Double-clamped beam made of gallium arsenide (GaAs) coated with 15-nm-thick nichrome (NiCr) terahertz (THz) absorbing layer [30,31]. (b) Silicon nitride beam coated with gold layer. Plasmonic metasurfaces made of titanium (Ti) are deposited on top of the gold layer [111].

The double-clamped beam resonator proposed by Zhang *et al.* [30, 31] demonstrates a different resonator design approach, compare to those in Section. 2.2.1, which focuses on improving the temperature coefficient of fractional frequency shift α of the resonator, rather than thermal isolation to achieve high thermal responsivity. Specially, [30, 31] utilize a 100-nm-thick GaAs beam with 10-nm-thick NiCr on top to achieve absorp-

tion efficiency of 20% for the terahertz radiation region (i.e., > 100 μm). As shown in Fig. 2.15, the sensing element is connected directly to the substrate without any thermal constraint, such as the thin-tether configuration in Section. 2.2.1, resulting in less-than-ideal thermal isolation. However, this beam resonator configuration provides a much higher temperature coefficient α, which compensates for the effects of non-ideal thermal isolation. In addition, the beam resonator can be fabricated more easily compared to those supported by thin tethers due to its simpler geometry. By using an integrated capacitive readout method, the device in Fig. 2.15(a) achieves a $D^* \approx 3.3\times10^7$ cm $\cdot \sqrt{\text{Hz}}$/W which is approximately a factor of three improvement over the best thin-rod-supported resonator [24].

Similar beam configuration shown in Fig. 2.15(b) [111] is also included in this section for comparison, despite its different mechanical sensing approach. This bilayer beam is constructed using a 22-nm-thick gold layer on top of 100-nm-thick silicon nitride film. Upon absorbing thermal radiation, this bilayer structure undergoes thermal bulking due to the thermal expansion coefficients mismatch between gold and silicon nitride, which the thermally-induced displacement is measured using a fiber optic interferometer. This bilayer beam also has a relatively large characteristic size $\sqrt{A_d}$ of ≈ 224 μm. However, this work is severely limited by the non-ideality from the readout interferometer which results in $D^* \approx 4.5 \times 10^6$ cm $\cdot \sqrt{\text{Hz}}$/W. More recently reported temperature-sensitive beam resonators focus either on tunability [112] or on the material's temperature coefficient [113], with conclusive thermal sensing performance data lacking; therefore, we omit these in this section.

2.2.3 Trampoline resonators

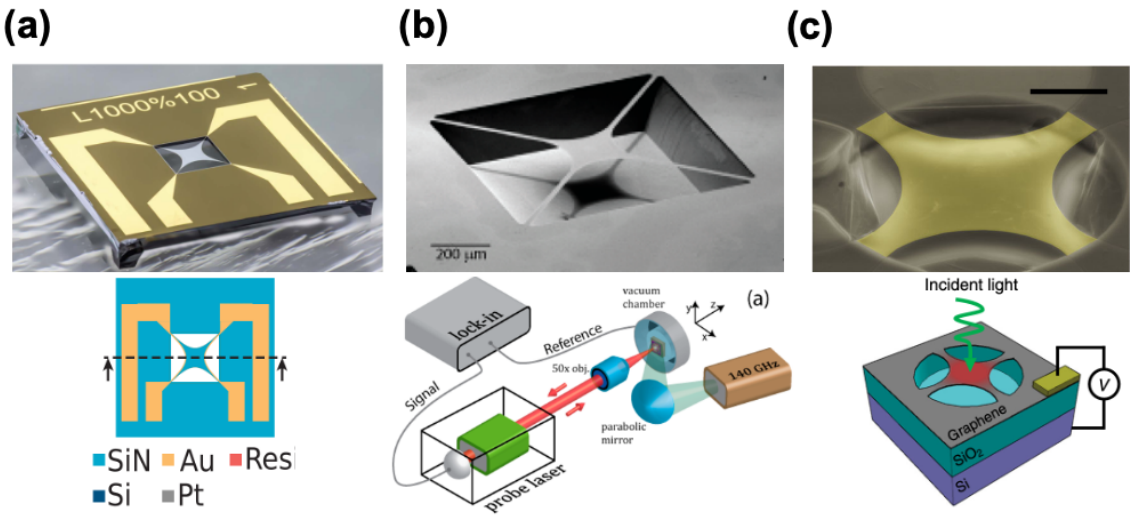

Figure 2.16: (a)Low-stress silicon nitride (SiN) trampoline resonator [27]. (b)High-stress SiN trampoline resonator coated with Cr/Au layer for sub-THz absorption [32]. (c)Graphene trampoline resonator [29]

Trampoline resonators of various kinds shown in Fig. 2.16 are the most recent addition to the family of NMR-based thermal detectors, which also exhibit the highest thermal sensing performance. This type of resonator achieves both excellent thermal isolation due to the thin tether and a large temperature coefficient of fractional frequency α when using a thin-film material with low intrinsic tensile stress [27]. This, in turn translates to impressive thermal responsivity. For instance, the device shown in Fig. 2.16(a), utilizes a low-stress (150 MPa) SiN membrane that was fabricated by low-pressure chemical vapor deposition, for the trampoline. This kind of SiN film exhibits high temperature coefficient α due to its low stress. Combined with the excellent thermal isolation provided by the thin tether, this device achieves the highest thermal responsivity (i.e., 11000 W^{-1}) ever reported for any NMR-based thermal detector. In contrast, the device shown in Fig. 2.16(b) is made of a high-stress (i.e., $\approx$ 900 MPa) SiN thin film that is also roughly five times thicker than that in Fig. 2.16(a). This results in significantly smaller thermal responsivity (i.e., 2.05 W^{-1}). Intriguingly, Piller *et al.* [27] and Vicarelli *et al.* [32] achieve

a similar level of specific detectivity $D^* \approx 3\times10^8$ cm $\cdot \sqrt{\text{Hz}}/\text{W}$ despite Vicarelli *et al.* [32] having a significantly lower thermal responsivity. This may be due to the high-stress, bulkier SiN used in [32], which results in significantly better frequency stability than that in [27], compensating for the lower responsivity. Lastly, the device shown in Fig. 2.16(c) exhibits a lower $D^* \approx 6 \times 10^6$ cm $\cdot \sqrt{\text{Hz}}/\text{W}$ due to very low absorption coefficient (i.e., $\approx 2\%$) of graphene and its poor frequency stability (i.e., low Q-factor).

2.3 Performance comparison

Nanomechanical resonators NMRs vs. traditional thermal-based detectors				
Detector type	D^* (cm $\cdot$ Hz$^{1/2}$W^{-1})	$\sqrt{A_d}$ (μm)	Tested wavelength (μm)	NEP (pW/$\sqrt{\text{Hz}}$)
Nanomechanical				
Zhang *et al.* 2.2.1(a) [26]	1.2×10^7	3	$8-14$	24
Laurent *et al.* 2.2.1(b) [24]	4.4×10^7	12	$8-12$	27
Hui *et al.* 2.2.1(c) [28]	5.7×10^6	120	~ 8.8	2100
Zhang *et al.* 2.2.2(a) [31]	3.3×10^7	30	~ 100	90
Yi *et al.* 2.2.2(b) [111]	4.5×10^6	224	~ 6	5000
Piller *et al.* 2.2.3(a) [27]	3.0×10^8	45	$1-25$	14
Vicarelli *et al.* 2.2.3(b) [32]	3.0×10^8	300	~ 214	100
Blaikie *et al.* 2.2.3(c) [29]	6.0×10^6	6	NA	100
Martini *et al* [114]	3.8×10^9	1000	$1-25$	27
Traditional				
Thermopile [70]	8.0×10^8	100	$5-15$	13
VO_x bolometer [108]	6.2×10^8	78	$8-14$	12
Pyroelectric IR [3, 90]	1.0×10^9	1000	$8-14$	100
Pyroelectric THz [91]	1.1×10^8	5000	$0.25-440$	4500
This work, Chapter. 5	3.4×10^9	1000	~ 150	27
Fundamental Limit [3]	1.8×10^{10}			

Table 2.1: Comparison of thermal sensing performance between nanomechanical resonators (NMRs) and traditional thermal-based detectors (i.e., thermopiles, bolometers, and pyroelectric detectors).

In Table. 2.1, we aim to thoroughly benchmark the thermal sensing performance of various detectors (i.e., NMR-based detectors, thermopile, bolometer and pyroelectric

detector) in terms of specific detectivity D^*, detectors characteristic size $\sqrt{A_d}$, target infrared wavelength range and noise equivalent power NEP. In this comparison, we regard D^* as the ultimate performance indicator as it is commonly used in many commercial detector specification sheets and is calculated as $\sqrt{A_d}$/NEP. This metric is normalized by detector size which eliminate the size-dependent effect on NEP, providing a fairer basis for performance comparison. We note that, through years of continuous development, the performance of NMR-based detectors is gradually improving to a level that is on par with state-of-the-art traditional bolometers and thermopiles. However, they still fall short of the best commercial pyroelectric detector.

Since NMR-based thermal detectors rely on temperature-dependent mechanical resonance frequency shifts rather than the electrical thermal sensing mechanism, their noise profile is inherently different from that of electrically based thermal detectors. However, to date, the reported NMR-based thermal sensing studies [24–32, 114] often lack a thorough investigation into resonators noise processes [35, 36, 38–40, 42, 43, 115] in the context of thermal sensing. Among these, only Laurent *et al.* [24], Zhang *et al.* [26], Blaikie *et al.* [29], Piller *et al.* [27] and Martini *et al.* [114] present frequency noise characterizations. Here, the most recent work by Martini *et al.* [114] demonstrated signs of reaching the fundamental temperature fluctuation noise limit at a specific sampling frequency. Nevertheless, none of the existing studies fully demonstrate that the NMR noise profile is dominated by fundamental temperature fluctuation across various PLL settings and over a broad range of sampling frequencies (i.e., measurement bandwidth).

3. Theoretical Background

3.1 Lumped mechanical model

3.1.1 Free response

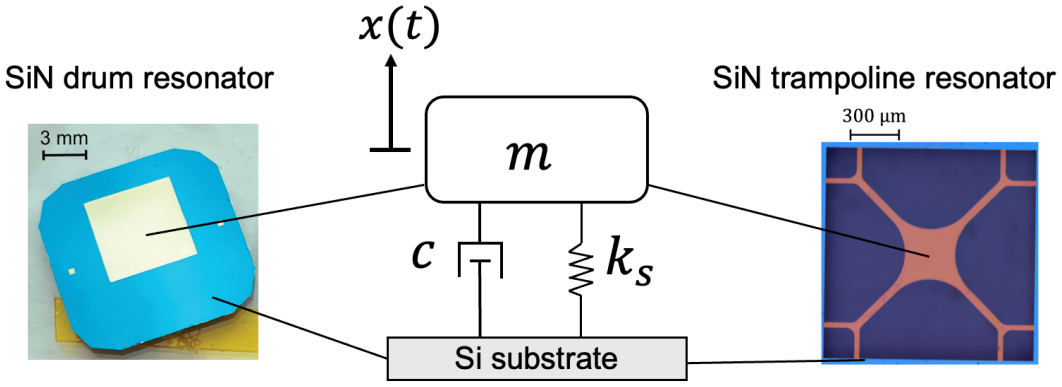

Figure 3.1: SiN nanomechanical resonators modeled as a 1D mass-spring-damper system.

At the core of this thesis are nanomechanical resonators (NMRs), which are tiny devices made of thin-film materials, typically with a thickness on the order of tens of nanometers. In the simplest form, when considering only one degree of freedom, these systems can be modeled as a mass-spring-damper system. Specifically, as shown in Fig. 3.1, the thin-film NMRs represent the mass, while the bulkier substrate, such as silicon, can be regarded as a fixed anchor. By assuming zero displacement $x(t)$ at static equilibrium, the 1D equation of motion of the NMR is:

$$m\ddot{x} + c\dot{x} + k_s x = 0, \tag{3.1}$$

where $\dot{x}$ denotes $dx(t)/dt$, c is the damping coefficient, and k_s is the spring coefficient. Note that when using a lumped model to represent a continuum-structured resonator (e.g., beam, string, membrane, etc.), effective mass and stiffness should be used, which we will discuss in the following section.

Conventionally, Eq. 3.1 is often written in a mass-normalized form [116] so that key vibration parameters (i.e., resonance frequency ω_n and damping ratio ζ) can be readily identified:

$$\ddot{x} + 2\zeta\omega_n\dot{x} + \omega_n^2 x = 0, \tag{3.2}$$

where $\omega_n = \sqrt{\frac{k_s}{m}}$ and $\zeta = \frac{c}{2\sqrt{k_s m}}$. In the absence of external force input (i.e., right-hand side of Eq. 3.2 is zero) and assuming either a critically damped ($\zeta = 1$) or underdamped system ($\zeta < 1$), solving Eq. 3.2 yields the natural response of the system,

$$x_{free}(t) = A_1 e^{-\zeta\omega_n t} \cdot \sin(\omega_n\sqrt{1-\zeta^2}\ t + \phi_1), \tag{3.3}$$

where A_1 and ϕ_1 represent the amplitude and phase which can be determined from the initial conditions (i.e., initial displacement $x(0)$ and velocity $\dot{x}(0)$). It is worth noting that due to the presence of damping, the sinusoidal part contains a frequency component different from ω_n, taking the form $\omega_n\sqrt{1-\zeta^2}$. This is commonly referred to as the damped resonance frequency, ω_r:

$$\omega_r = \omega_n\sqrt{1-\zeta^2}. \tag{3.4}$$

When a system is very lightly damped (e.g., NMRs under high vacuum), $\zeta \ll 1$, which yields $\omega_n \simeq \omega_r$.

3.1.2 Forced response under harmonic excitation

During operation, NMRs are typically driven by a single harmonic excitation that is very close to their damped resonance frequency. Here, we express the harmonic excitation as $F_0 \cos(\omega t)$ with ω being the carrier frequency; therefore, the equation of motion becomes:

$$\ddot{x} + 2\zeta\omega_n\dot{x} + \omega_n^2 x = f_0 \cos\omega t, \tag{3.5}$$

where f_0 is the mass-normalized input force F_0/m. Eq. 3.5 is a inhomogeneous linear second-order ordinary differential equation, therefore the total solution takes the form of:

$$\begin{aligned} x_{total}(t) &= x_{free}(t) + x_{forced}(t) \\ &= A_1 e^{-\zeta\omega_n t} \cdot \sin(\omega_r t + \phi_1) + X\cos(\omega t - \theta), \end{aligned} \tag{3.6}$$

where x_{free} is the homogeneous solution we solved in the previous section, representing the transient response of the system, while x_{forced} is the particular solution representing the steady-state response of the system. Since NMRs typically operate in steady state, we ignore the transient part and focus on examining the particular solution: $x_{forced} = X\cos(\omega t - \theta)$. Here, the value of X and θ can be solved by plugging x_{forced} as x into Eq. 3.5. Here we emphasize on obtaining X:

$$X = \frac{f_0}{\omega_n^2\sqrt{(1-(\frac{\omega}{\omega_n})^2)^2 + (2\zeta\frac{\omega}{\omega_n})^2}}. \tag{3.7}$$

Building on top of this, we divide Eq. 3.7 by the magnitude of the input force $F_0 = f_0 \cdot m$ to obtain the mechanical susceptibility $\chi(\omega)$ of the system:

$$\chi(\omega) = \frac{1}{m\omega_n^2\sqrt{(1-(\frac{\omega}{\omega_n})^2)^2 + (2\zeta\frac{\omega}{\omega_n})^2}}. \tag{3.8}$$

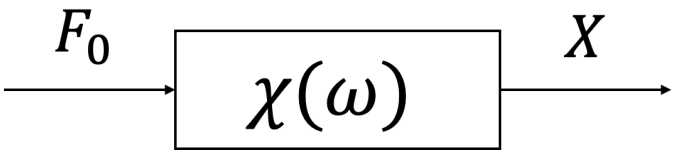

Figure 3.2: Mechanical susceptibility block diagram

The concept of mechanical susceptibility can be simply illustrated using a single block diagram, as shown in Fig. 3.2, in which an input force at a given frequency ω yields an output amplitude of the system. Interestingly, by setting $\omega = 0$, meaning a static force is applied, $\chi(0)$ reduces to $\frac{1}{m\omega_n^2}$. Note that $m\omega_n^2$ represents the system stiffness k_s, and thus $\chi(0) = 1/k_s$, consistent with Hooke's law.

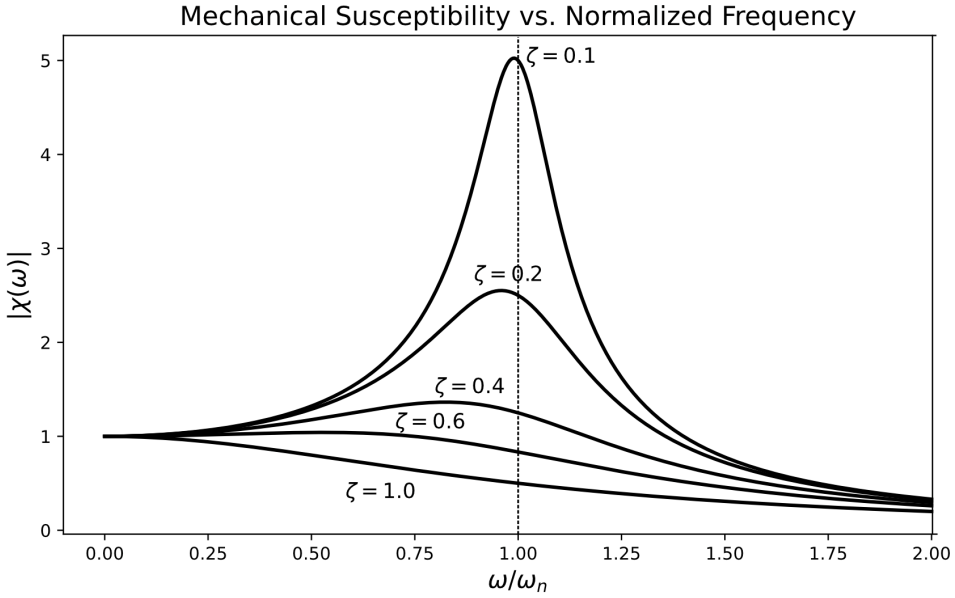

Figure 3.3: Mechanical susceptibility vs. normalized frequency plot with unit mass.

A more meaningful way to analyze Eq. 3.8 is by examining at its frequency response. In Fig. 3.3, we plot mechanical susceptibility for various damping ratio ζ. A peak amplitude occurs in these curves when $\zeta \leq \frac{1}{\sqrt{2}}$, at the frequency $\omega_{\text{peak}} = \omega_n\sqrt{1-2\zeta^2}$. Although ω_{peak} differs slightly from the damped resonance frequency $\omega_r = \omega_n\sqrt{1-\zeta^2}$, when ζ is very small, the two become approximately equal: $\omega_{peak} \approx \omega_r$. Moreover, due to the small damping, $\omega_r \approx \omega_n$, and thus $\omega_{peak} \approx \omega_r \approx \omega_n$. We can see that this is the

case for $\zeta = 0.1$ in Fig. 3.3, peak occurs close to $\omega/\omega_n \approx 1$.

A particularly important concept widely used in the nanomechanical resonator community is the Q-factor, which is inversely related to the damping ratio ζ, and is approximated as $Q \approx \frac{1}{2\zeta}$ for very small damping. It quantifies how sharp (or narrow) the mechanical resonance is. By replacing ζ with Q, we express Eq. 3.8 in a slightly different form:

$$\chi(\omega) = \frac{1}{m\omega_n^2\sqrt{(1-(\frac{\omega}{\omega_n})^2)^2 + (\frac{\omega}{Q\omega_n})^2}}. \tag{3.9}$$

Mechanical susceptibility $\chi(\omega)$ is regarded as the steady-state frequency response. However, it is also important to analyze the transient response under harmonic drive. When actuating the NMR near its natural frequency, the vibration amplitude does not immediately reach its steady-state value but instead rises gradually over time. This rise is described by Eq. 3.6 as $e^{-\zeta\omega_n t}$. By introducing the quality factor Q, this exponential response can be rewritten as $e^{-\frac{\omega_n}{2Q}t}$, from which we extract the system's mechanical time constant $\tau_{\text{mech}} = \frac{2Q}{\omega_n}$.

3.1.3 Thermomechanical displacement noise

A key difference between nanomechanical resonators NMRs and traditional macroscopic mechanical resonators lies in their susceptibility to microscopic perturbations, due to their exceptionally small mass—on the order of nanograms. According to the *equipartition theorem* [117], when placed in an environment with temperature T above absolute zero, each degree of freedom (i.e., mechanical mode) of NMRs are subjected to thermal energy $k_B T/2$, where k_B is the Boltzmann constant. As a result, even at thermal equilibrium and in the absence of external excitation, NMRs still experience constant random vibrations at an extremely small scale (i.e., sub-nanometer). Using a lumped vibration model (i.e., considering only a single vibrational mode), we can establish the following

relation:

$$\frac{1}{2}k_BT = \frac{1}{2}m\omega_n^2\langle x^2\rangle. \tag{3.10}$$

Here, $\langle x^2\rangle$ is a statistically stationary, time-independent quantity that represents the mean square vibration amplitude due to environmental thermal energy.

A more useful way to describe such displacement noise is through the power spectral density $S_x(\omega)$ in units of m^2/Hz, which allows us to examine the spectral content (i.e., frequency components) of the noise. Assuming a one-sided $S_x(\omega)$, we can relate the power spectral density to the mean square displacement $\langle x^2\rangle$ using the following integral [6, 118, 119]:

$$\langle x^2\rangle = \int_0^\infty \frac{d\omega}{2\pi} S_x(\omega). \tag{3.11}$$

Here, we further express $\langle x^2\rangle$ as $k_BT/(m\omega_n^2)$, deriving from Eq. 3.10,

$$\frac{k_BT}{m\omega_n^2} = \int_0^\infty \frac{d\omega}{2\pi} S_x(\omega). \tag{3.12}$$

From the previous section, $S_x(\omega)$ must share the same spectral characteristic as the mechanical susceptibility $\chi(\omega)$, shown in Fig. 3.3. Therefore, following the block diagram in Fig. 3.2, we deduce that there must be a one-sided force spectral density $S_f(\omega)$, in units of N^2/Hz, that gives rise to $S_x(\omega)$. The relation between the force and displacement spectral density is:

$$S_x(\omega) = \chi(\omega)^2 \cdot S_f. \tag{3.13}$$

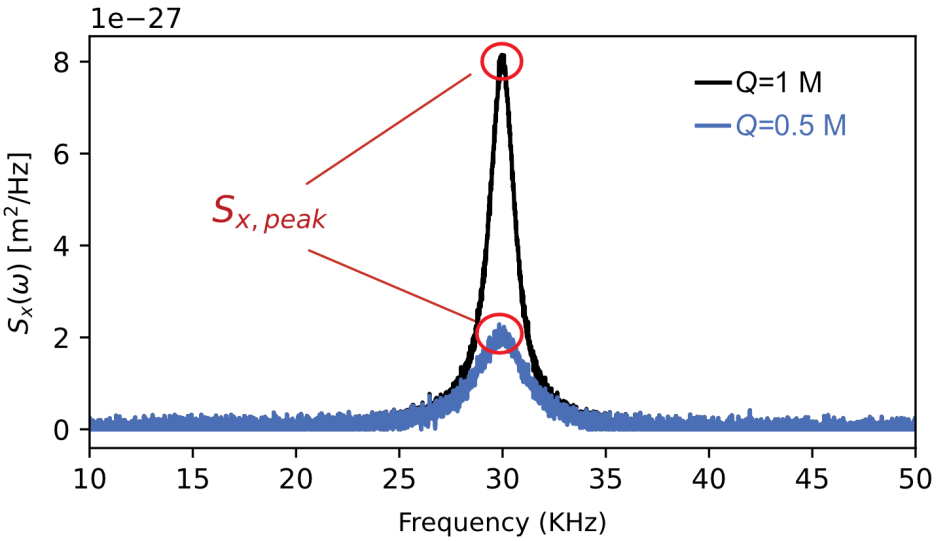

Figure 3.4: Thermomechanical peaks simulated for a fixed arbitrary mass (m) and resonance frequency (ω_n) of a nanomechanical resonator, with different Q-factors.

Note that S_f is independent of frequency, assuming that thermomechanical force noise is white noise around the eigen frequencies of the resonator. By plugging Eq. 3.13 into Eq. 3.12, we solve for the only unknown, S_f:

$$S_f = \frac{4k_B T m \omega_n}{Q}. \tag{3.14}$$

Substituting S_f back into Eq. 3.13, we obtain Fig. 3.4, which shows that a higher Q-factor leads to a narrower thermally driven resonance. For physical sensing applications that detect changes via resonance frequency shifts (e.g., mass, thermal, or acceleration sensing), instead of examining the entire noise spectrum, the point of interest is typically at $\omega = \omega_n$, which is highlighted in red and labeled as $S_{x,peak}$ in Fig. 3.4. By evaluating Eq. 3.13 at $\omega = \omega_n$, we obtain:

$$S_{x,peak} = \chi(\omega_n)^2 \cdot S_f = \frac{4k_B T Q}{m\omega_n^3}. \tag{3.15}$$

Here, $S_{x,peak}$ represents the displacement noise (in m^2/Hz) at the resonator's resonance frequency, induced by thermomechanical fluctuations. Eq. 3.15 indicates that a higher

Q-factor mechanical mode exhibits greater thermomechanically induced displacement noise peak, which may seem undesirable in the context of noise minimization. However, examining the noise in terms of displacement is not the appropriate metric, since our interest lies in physical sensing in the frequency domain (i.e., detecting physical changes via frequency shifts).

3.1.4 Thermomechanical frequency noise

Robin's formula [115] accurately describes how displacement noise (S_x in units of m^2/Hz) is transferred to phase noise (S_ϕ in units of rad^2/Hz). Here, we follow the formulation presented in [6], shown as follows:

$$S_\phi = 2 \cdot \frac{S_{x,peak}}{A_{rss}^2} = \frac{8 k_B T Q}{m \omega_n^3 A_{rss}^2}, \tag{3.16}$$

where A_{rss} is the driven vibration amplitude at the mechanical mode frequency ω_n. Robin's formula indicates that displacement noise can be significantly suppressed in the phase domain by driving a selected mechanical mode at a higher amplitude (A_{rss}). This concept can be graphically illustrated in phase space for clarity, as shown in Fig. 3.5. Note that this figure is largely adapted from both [6] and [43], with minor modifications.

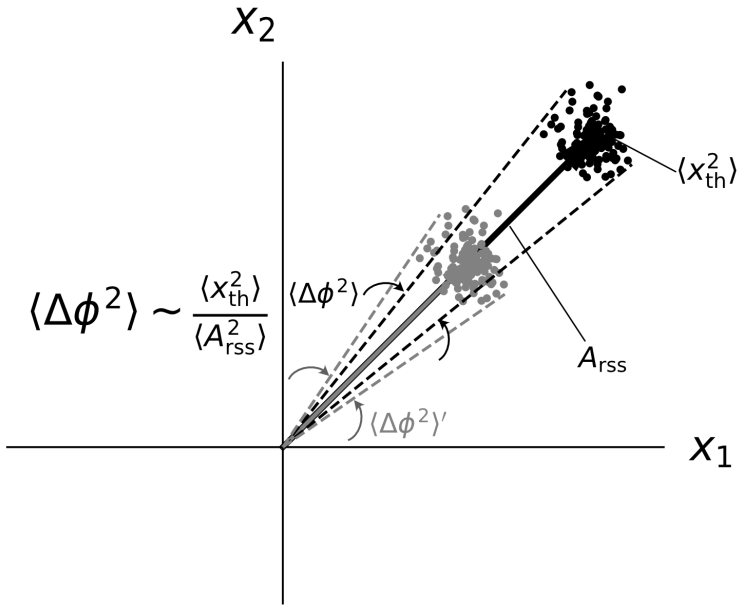

Figure 3.5: Displacement to phase noise in phase space. Comparison between a lower (grey cloud) and higher drive amplitude (black cloud).

In Fig. 3.5, the X_1 and X_2 axes represent the in-phase and out-of-phase quadratures, respectively. The spherical clouds represent the average thermomechanical displacements $\langle x^2_{th} \rangle$; the distance from the clouds to the origin represents the driven amplitude A_{rss}; and the projection angle of the clouds from the origin, corresponds to the average phase deviation $\langle \Delta\phi^2 \rangle$ induced by $\langle x^2_{th} \rangle$. From this figure, we can see that while the magnitude of the thermomechanical displacements $\langle x^2_{th} \rangle$ remains the same (as indicated by the diameter of the cloud), a higher A_{rss} (black cloud) results in a narrower phase angle compared to the lower A_{rss} case (grey cloud), thereby reducing the phase noise.

The phase noise spectral density S_ϕ, calculated in Eq. 3.16, can also be viewed as a frequency noise spectral density with units of Hz^2/Hz, which we denote as $S_{\Delta\omega}$. Following the derivation in [39], this relationship is given by:

$$S_{\Delta\omega} = \frac{1}{\tau^2_{\text{mech}}} \cdot S_\phi, \tag{3.17}$$

where τ_{mech} is the mechanical time constant of the resonator, expressed as $2Q/\omega_n$, such

that Eq. 3.17 expands to:

$$S_{\Delta\omega} = \frac{2k_BT}{m\omega_n Q A_{rss}^2}. \tag{3.18}$$

Lastly, frequency-domain noise is also often expressed in terms of fractional frequency ($y = \delta\omega/\omega_n$) for a normalized representation. Therefore, we can further convert $S_{\Delta\omega}$, given in units of Hz^2/Hz, into the fractional frequency spectral density S_y, with units of 1/Hz, as:

$$S_{y,tmech} = \frac{1}{\omega_n^2} \cdot S_{\Delta\omega} = \frac{2k_BT}{m\omega_n^3 Q A_{rss}^2}. \tag{3.19}$$

From Eq. 3.19, we highlight the importance of using a high-Q (i.e., low damping ratio ζ) resonator driven at a large vibration amplitude, as both high Q and large A_{rss} help minimize thermomechanical-noise-induced frequency fluctuations, thereby improving frequency stability.

So far, the derived $S_{y,tmech}$ in Eq. 3.19 appears as white frequency noise. However, according to the theoretical modeling in [120] and the experimental demonstration in [121], it has been shown that $S_{y,tmech}$ affects nanomechanical resonators at a rate governed by their mechanical time constant τ_{mech}. Therefore, in its complete form, $S_{y,tmech}$ is subjected to a one-pole, low-pass mechanical filter $H_{mech}(\omega)$, defined as $1/(1 + j\omega\tau_{mech})$. In this case, the complete form of thermomechanical frequency noise for NMRs is:

$$S_{y,tmech}(\omega) = \frac{2k_BT}{m\omega_n^3 Q A_{rss}^2} |H_{mech}(\omega)|^2. \tag{3.20}$$

3.2 2D continuum mechanical model

So far, we have used a 1D lumped mechanical model to perform our mechanical analysis, which has been sufficient for deriving key frequency noise expressions arising from thermomechanical fluctuations. However, such lumped model has reached its limitation. To enable further investigation, we now establish a 2D continuum mechanical model.

In this work, we primarily use thin-film, square SiN membrane resonators (or variants thereof) under tensile stress. Therefore, we adopt a 2D wave equation in which the membrane's rigidity is dominated by tensile stress σ:

$$\sigma \nabla^2 U(x,y,t) - \rho \frac{\partial^2 U(x,y,t)}{\partial t^2} = 0, \tag{3.21}$$

where $U(x,y,t)$ represents the location and time-dependent, out-of-plane displacement and ρ is density of the membrane material. The 2D wave equation for a square membrane under tension is a classic eigenvalue problem, in which the mode shapes are the eigenfunctions of the spatial Laplacian operator. For a square membrane with clamped edges, the eigenfunctions (mode shapes) are separable and given as:

$$\phi_{mn}(x,y) = \sin\left(\frac{m\pi x}{L}\right) \sin\left(\frac{n\pi y}{L}\right), \tag{3.22}$$

where m, n represent the mode indices and L is the side length of the membrane. The corresponding eigenfrequencies are determined by the eigenvalues through

$$\omega_{mn} = \frac{\pi}{L} \cdot \sqrt{\frac{\sigma}{\rho} \cdot (m^2 + n^2)}. \tag{3.23}$$

Here, we plot the first 4 mode shapes of a square membrane in Fig. 3.6 as a graphical reference for the spatial solution.

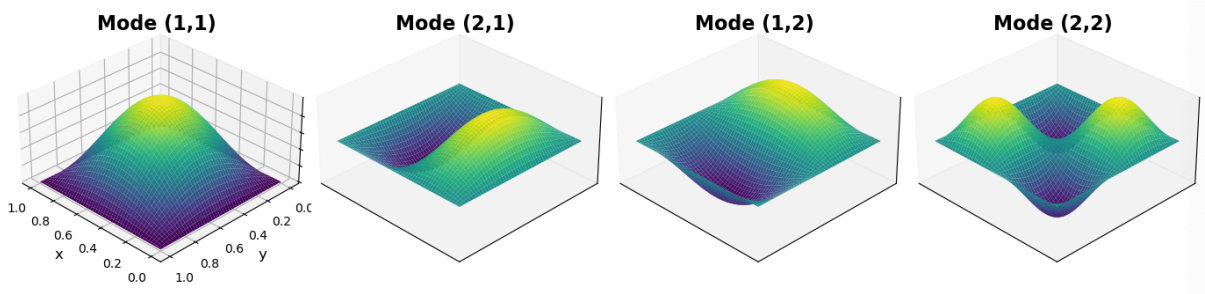

Figure 3.6: Mode shape of a vibrating square membrane, generated using *Matplotlib*.

3.2.1 Effective mass

The continuum model indicates that there are, in principle, infinite number of mode shapes and corresponding resonance frequencies for a clamped membrane. As a result, each mode should be subject to their own corresponding stiffness and mass [6]:

$$\omega_{mn} = \sqrt{\frac{k_{eff}}{m_{eff}}}. \tag{3.24}$$

Here, k_{eff} and m_{eff} are effective stiffness and mass for a given mode (m, n). Typically, after determining m_{eff}, one can subsequently calculate k_{eff} using $k_{eff} = \omega_{mn}^2 m_{eff}$. To determine the value of m_{eff}, one can evaluate the following integral which consist of the spatial eigenfunction ϕ_{mn} [6]:

$$m_{eff} = \rho h \int_0^L \int_0^L \phi_{mn}^2(x, y)\ dxdy, \tag{3.25}$$

where h is the thickness of the membrane. Eq. 3.25 is derived by equating the kinetic energy of a continuum resonator to that of a lumped model. A detailed derivation can be found in [6]. For a square membrane, $m_{eff} = m/4$. It is worth noting that for more complex geometries, finding an analytical expression can be challenging, and m_{eff} should be determined using finite element analysis software such as *COMSOL Multiphysics* or *ANSYS Mechanical*. With the notion of effective parameters, we modify Eq. 3.19 to incorporate them:

$$S_{y,tmech}(\omega) = \frac{2k_B T}{m_{eff}\omega_r^3 Q A_{rss}^2} |H_{mech}(\omega)|^2, \tag{3.26}$$

where ω_r denotes the resonance frequency at which the resonator operates. We will solely use ω_r for the rest of this thesis to avoid confusion.

3.3 Dissipation mechanisms

According to our analysis in Sec. 3.1, a high Q-factor is crucial for both narrowing the resonance bandwidth and improving frequency stability (see Eqs. 3.18–3.19) of a NMR. Therefore, enhancing the Q-factor of NMRs has been extensively investigated over the years [122–125]. In this section, we limit our discussion to dissipation mechanisms that affect thin-film membrane resonators operating in a high vacuum environment, which represents the conditions relevant to this work. We briefly discuss several of the most well-known dissipation mechanisms in NMRs and how they can be minimized. The major dissipation mechanisms can be categorized into three main types—namely, medium loss, clamping loss, and material loss. Quantitatively, these mechanisms contribute to the Q-factor of NMRs in the following manner:

$$\frac{1}{Q} = \frac{1}{Q_{\text{medium}}} + \frac{1}{Q_{\text{clamping}}} + \frac{1}{Q_{\text{material}}}. \tag{3.27}$$

1. $\boldsymbol{Q}_{\text{medium}}$.

   When situated in air, a membrane NMR with thickness on the order of hundreds of nanometers experiences significant air damping relative to its minute mass, making the system heavily overdamped and resulting in a low Q-factor due to the surrounding medium (i.e., Q_{medium}). However, when placed in a high vacuum chamber (typically $< 1 \times 10^{-6}$ hPa in our case), dissipation through air damping is drastically minimized. This is because lower pressure increases the mean free path of gas molecules, thereby reducing the likelihood of collisions with the NMR. This loss mechanism is the primary reason why high-performance NMR sensors are typically operated in high-vacuum environments.

2. $\boldsymbol{Q}_{\text{clamping}}$.

   A vibrating membrane NMR can be viewed as a standing wave that carries energy

in the form of phonons. This energy is subsequently radiated to the supporting substrate through the clamping points. Therefore, if an NMR can better confine its vibrational energy within the boundary between the membrane and its substrate, Q_{clamping} can be enhanced. To achieve better confinement of energy without changing the substrate or resonator material, it is evidenced that one can either excite a symmetric mode (i.e., equal mode indices $m = n$, such as mode (1,1) or (2,2) in Fig. 3.6) or utilize a resonator with a high characteristic length-to-thickness ratio [126].

3. $\boldsymbol{Q}_{\text{material}}$.

   There are also intrinsic losses within the NMR material itself, caused by internal friction mechanisms during vibration. Such Q_{material} can be calculated as [127]:

$$Q_{\text{material}} = \frac{E'}{E''}, \tag{3.28}$$

   where E' represents the real part and E'' the imaginary part of the complex Young's modulus. Here, E' is the standard Young's modulus, analogous to a "spring" term that represents energy storing during vibration, whereas E'' characterizes dissipation.

3.3.1 Damping Dilution

For thin-film SiN membranes with a thickness of approximately 100 nm, as primarily used in this work, Q_{material} typically falls in the mid-thousands range [128]. Eq. 3.28 implies that Q_{material} strictly depends on the intrinsic material properties of the NMR. However, numerous studies [122, 123, 129] have reported that SiN membrane and string resonators exhibit significantly higher Q values (i.e., exceeding one million) compared to their expected Q_{material}, due to a phenomenon known as damping dilution [130]. Here, for simplicity, we omit the effect of nonlinear damping dilution and focus on examining

only linear damping dilution which assumes no material elongation.

In a vibrating membrane or string (1D), mechanical energy is stored in two forms: tensile energy and bending energy. Therefore, by definition, Q can be expressed as [131]:

$$Q = 2\pi \frac{W_{\text{tensile}} + W_{\text{bending}}}{\delta W_{\text{bending}}}, \tag{3.29}$$

where the terms in the numerator represent the total stored energy, and the denominator represents the energy lost per cycle due to bending. It is worth noting that only bending contributes to energy loss, while tension does not, as it causes minimal internal friction. Furthermore, by definition,

$$Q_{\text{material}} = 2\pi \frac{W_{\text{bending}}}{\delta W_{\text{bending}}}, \tag{3.30}$$

Eq. 3.29 can subsequently be rewritten as:

$$Q = 2\pi \frac{W_{\text{tensile}}}{\delta W_{\text{bending}}} + Q_{\text{material}}. \tag{3.31}$$

In this case, we can clearly see that the overall Q consists of two additive terms, one of which is Q_{material}. Here, we can introduce a damping dilution factor α_{dd} such that

$$Q = 2\pi \frac{W_{\text{tensile}}}{\delta W_{\text{bending}}} + Q_{\text{material}} = \alpha_{\text{dd}} \cdot Q_{\text{material}}, \tag{3.32}$$

in which we can solve for α_{dd}:

$$\alpha_{\text{dd}} \approx \frac{W_{\text{tensile}}}{W_{\text{bending}}}. \tag{3.33}$$

To calculate W_{tensile} and W_{bending} for a square membrane resonator, one can use the following integrals [6]:

$$W_{\text{tensile}} = \frac{1}{2}\sigma h \int_0^L \int_0^L \left\{ \left(\frac{\partial \phi'_{mn}}{\partial x} \right)^2 + \left(\frac{\partial \phi'_{mn}}{\partial y} \right)^2 \right\} dx\, dy, \tag{3.34}$$

$$W_{\text{bending}} = \frac{D_P}{2} \int_0^L \int_0^L \left(\left(\frac{\partial^2 \phi'_{mn}}{\partial x^2} \right)^2 + \left(\frac{\partial^2 \phi'_{mn}}{\partial y^2} \right)^2 + 2(1-\nu) \left[\left(\frac{\partial^2 \phi'_{mn}}{\partial x \partial y} \right)^2 - \frac{\partial^2 \phi'_{mn}}{\partial x^2} \frac{\partial^2 \phi'_{mn}}{\partial y^2} \right] \right) dx\, dy \tag{3.35}$$

where $D_P = \dfrac{Eh^3}{12(1-\nu^2)}$ is the flexural rigidity of the membrane, ν is the Poisson ratio. Here, to fully capture the physics of a bending membrane, we must use a modified mode shape function ϕ'_{mn} that accounts for bending effects at the edges through the addition of an exponential term. To compare the difference between the modified mode shape ϕ'_{mn} and the original ϕ_{mn}, we plot the fundamental mode shape of a 1D string for both cases, as shown in Fig. 3.7. From this, we can see that the addition of an exponential term gives the mode shape a smoother transition at the boundaries, better representing the real energy loss at the edges.

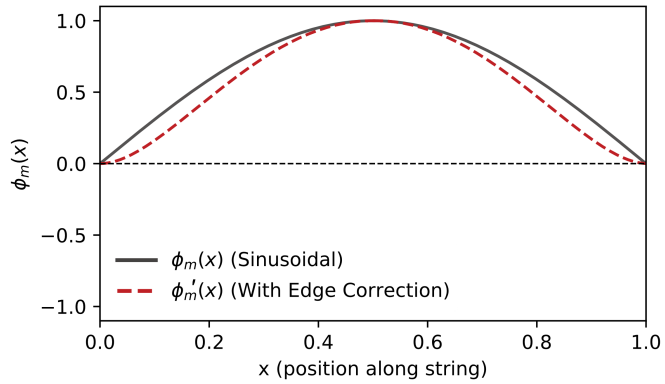

Figure 3.7: 1D fundamental mode shape with edge correction.

By substituting Eq. 3.35 and 3.34 into 3.33, the damping dilution factor for a membrane resonator can be approximated as:

$$\alpha_{\text{dd}} \approx \frac{1}{\underbrace{\frac{\pi^2(m^2+n^2)}{12} \frac{E}{\sigma} \left(\frac{h}{L} \right)^2}_{\text{sine shape}} + \underbrace{\frac{1}{\sqrt{3}} \sqrt{\frac{E}{\sigma}} \left(\frac{h}{L} \right)}_{\text{edge correction}}}. \tag{3.36}$$

Here, α_{dd} is divided into two parts: one from the sinusoidal mode shape, which is mode-dependent due to the mode indices (m, n), and the other from the exponential edge correction. In this work, we primarily utilize SiN membrane resonators with side lengths in the millimeter range and thicknesses of only hundreds of nanometers. This results in an ultra-small h/L ratio, causing the edge correction term to dominate the damping dilution:

$$\alpha_{\mathrm{dd}} \sim \frac{1}{\frac{1}{\sqrt{3}}\sqrt{\frac{E}{\sigma}}\left(\frac{h}{L}\right)}. \tag{3.37}$$

For demonstration purposes, consider a SiN membrane resonator with $L = 3$ mm and $h = 100$ nm (see the image on the left in Fig. 3.1), and typical material properties of $E = 300$ GPa and $\sigma = 100$ MPa. This results in an α_{dd} of approximately 1054, meaning that the Q_{material} is amplified by over a thousand times, yielding a Q-factor greater than one million.

3.4 Thermally induced resonance frequency shift

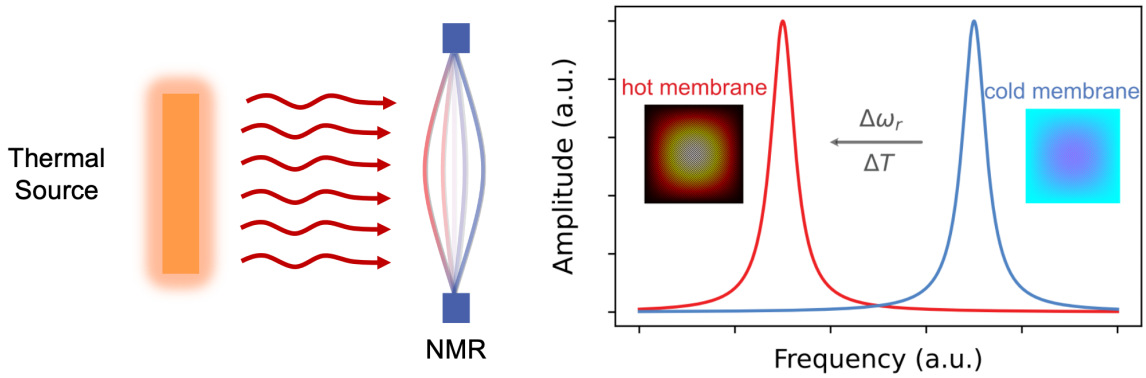

Figure 3.8: Nanomechanical membrane resonator undergoes frequency shift $\Delta\omega_r$ upon absorbing thermal radiation.

The fundamental working principle of thermal radiation sensing using temperature-sensitive NMRs can be conceptually described using a 1D lumped model (see Eqs. 3.1–

3.2). When thermal radiation impinges on and is absorbed by the NMR, the stiffness k_s decreases (i.e., thermally induced softening), leading to a corresponding reduction in the resonance frequency, since $\omega_r \approx \omega_n = \sqrt{k_s/m}$ (see Fig. 3.8). By relating the frequency variation to the temperature change during thermal absorption ($\Delta\omega_r/\Delta T$), thermal radiation sensing can be readily performed.

To analyze the nature of such thermally induced softening and how it affects the resonance frequency of a membrane resonator, we must revisit the 2D continuum model. As discussed previously and indicated in Eq. 3.21, the flexural rigidity of our SiN membrane resonators (analogous to stiffness k_s) is primarily dictated by the built-in tensile stress σ. Upon thermal radiation absorption, the membrane resonator undergoes thermal expansion, which consequently alters the built-in stress σ. To account for this, we modify Eq. 3.21 with the addition of $\sigma_r(x, y)$:

$$(\sigma + \sigma_r(x, y))\nabla^2 U(x, y, t) - \rho\frac{\partial^2 U(x, y, t)}{\partial t^2} = 0, \tag{3.38}$$

where $\sigma_r(x, y)$ represents change in in-plane stress due to thermal absorption. The closed-form expression for $\sigma_r(x, y)$ can be found in [132]. With the addition of $\sigma_r(x, y)$, the 2D wave equation becomes more challenging to solve analytically. Therefore, this is typically solved in polar coordinates rather than Cartesian, which reduces a 2D wave equation into a 1D wave equation. To demonstrate the similarity of mode shapes between a circular and a square membrane, we produce Fig. 3.9 as a reference using *Matplotlib*.

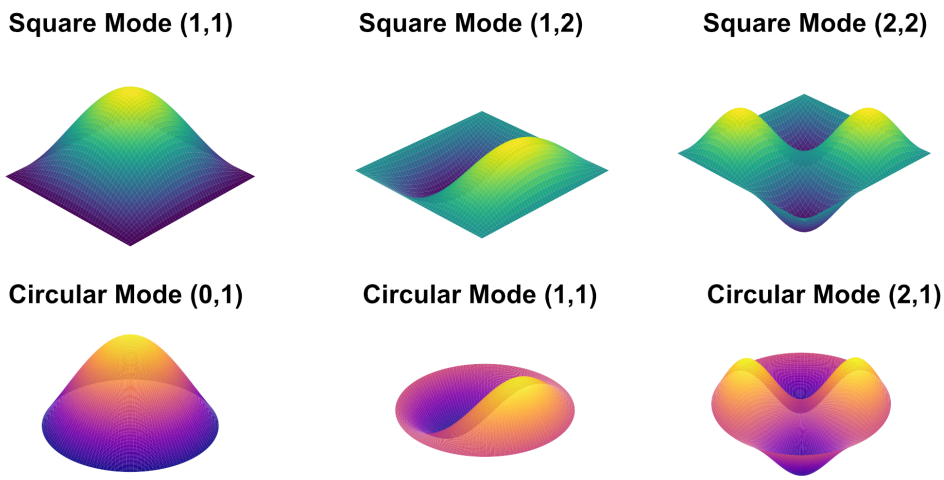

Figure 3.9: Mode shapes of a vibrating square vs. circular membrane, generated using *Matplotlib*.

By switching the coordinate system (i.e., $U(x, y, t)$ to $U(r, t)$), Eq. 3.38 becomes:

$$\frac{1}{r}\frac{\partial}{\partial r}[(\sigma + \sigma_r(r)) \cdot r\frac{\partial U(r,t)}{\partial r}] - \rho\frac{\partial^2 U(r,t)}{\partial t^2} = 0, \tag{3.39}$$

which r is the radial coordinate. Here, the thermally-induced stress variation σ_r can be calculated as [29, 132–134]:

$$\sigma_r = -\alpha_t E[\frac{1}{r^2}\int_0^r r\Delta T(r)dr + \frac{1+\nu}{1-\nu}\frac{\Delta\overline{T}}{2}], \tag{3.40}$$

where α_t is the thermal expansion coefficient, E is the Young's modulus and ν is the Poisson ratio of the material. $\Delta T(r)$ represents the location-dependent temperature change of the material upon absorbing thermal radiation, and $\Delta\overline{T}$ is the overall average temperature change. If we assume the membrane resonator has an approximately uniform temperature profile upon thermal absorption (i.e., $\Delta T(r) \approx \Delta\overline{T}$), Eq. 3.40 simplifies to a radius-independent form:

$$\sigma_r \approx -\frac{\alpha_t E}{1-\nu}\Delta\overline{T}. \tag{3.41}$$

Note that when $\Delta\overline{T} = 0$, indicating no thermal absorption, we have $\sigma_r = 0$, and Eq. 3.41

essentially reduces to Eq. 3.21. In this case, we first solve for the default eigenfrequency $\omega_{r(\Delta\overline{T}=0)}$ when there is no heating. We then introduce a temperature change $\Delta\overline{T}$ and solve Eq. 3.39 to obtain $\omega_{r(\Delta\overline{T})}$, representing the eigenfrequency after the temperature change. By evaluating $(\omega_{r(\Delta\overline{T})} - \omega_{r(\Delta\overline{T}=0)})/\Delta\overline{T}$, we can determine the frequency shift per unit of average temperature increase—that is, the temperature coefficient of frequency shift in units of Hz/K. For the fundamental mode of a circular drum resonator (see circular mode 0,1 in Fig. 3.9), this value is:

$$\frac{\omega_{r(\Delta\overline{T})} - \omega_{r(\Delta\overline{T}=0)}}{\Delta\overline{T}} \approx -\frac{E\alpha_t}{2\sigma(1-\nu)}\omega_{r(\Delta\overline{T}=0)}. \tag{3.42}$$

If we normalize Eq. 3.42 by the default ω_r, we can obtain the temperature coefficient of fractional frequency shift in units of 1/K:

$$\alpha \approx \frac{E\alpha_t}{2\sigma(1-\nu)}. \tag{3.43}$$

It is worth noting that Eq. 3.43 is a better approximation for lower order mode shapes, whereas its prediction error can reach 20% with higher order modes [50].

For the specific application of thermal radiation sensing, a higher α typically leads to a higher thermal responsivity R in units of 1/W, which represents the amount of fractional frequency shift induced per watt of power incident on the surface of the resonator. This is defined as:

$$R = \frac{\gamma\alpha}{G}|H_{th}(\omega)|, \tag{3.44}$$

where G is the overall thermal conductance of the resonator during illumination, γ is the absorption coefficient at the incident radiation wavelength, and $H_{th}(\omega)$ represents the low-pass thermal filter of the membrane resonator, which will be discussed in the next section.

3.5 Lumped thermal model

In its simplest form, the thermal process within a resonator can be described by a 1D lumped model [3], which is analogous to an RC circuit:

$$C_{th}\Delta\dot{T}(t) + G\Delta T(t) = P_{in}, \tag{3.45}$$

where C_{th} and G are the thermal capacitance and thermal conductance of the resonator, respectively, and $\Delta T(t)$ represents the lumped temperature rise due to the power input P_{in}. To solve for $\Delta T(t)$, we perform a Fourier transform on Eq. 3.45, yielding the solution for $\Delta T(\omega)$:

$$\Delta T(\omega) = \frac{1}{1 + j\omega\frac{C_{th}}{G}}\frac{1}{G} \cdot P_{in}(\omega) = \frac{H_{th(\omega)}}{G} \cdot P_{in}(\omega), \tag{3.46}$$

where the term $1/(1 + j\omega\frac{C_{th}}{G})$ is known as the one-pole, low-pass thermal filter $H_{th}(\omega)$, and the ratio C_{th}/G represents the thermal time constant τ_{th}. Another way to look at Eq. 3.46 is to use simple block diagram shown in Fig. 3.10 which has input power as the single input and temperature variation as a single output. The transfer function between the input and output is essentially $H_{th(\omega)}/G$.

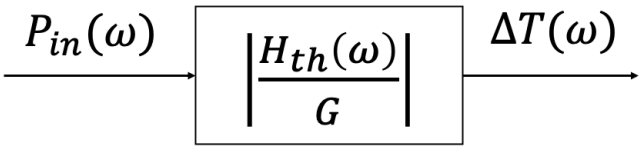

Figure 3.10: Thermal block diagram representing Eq. 3.46.

From this, we can clearly see that a miniaturized object like a nanomechanical resonator naturally possesses a small thermal conductance G; therefore, for each Watt of absorbed power, the resulting temperature rise can be more substantial compared to an object at larger scale.

When the resonator is placed in an environment at temperature T above absolute

zero, it is subject to thermal power fluctuations given by $4k_BT^2G$ [36], according to the *fluctuation-dissipation theorem*, which continuously perturbs the resonator's temperature. This term, $4k_BT^2G$, is denoted here as the one-sided power spectral density $S_{TP}(\omega)$, with units of W^2/Hz. To see how this power fluctuation manifests itself as a temperature fluctuation $S_{Temp}(\omega)$ in units of K^2/Hz, we can follow similar logic shown in Fig. 3.10. The transformation from $S_{TP}(\omega)$ to $S_{Temp}(\omega)$ is

$$\begin{aligned} S_{Temp}(\omega) &= S_{TP}(\omega) \cdot \left| \frac{H_{th}(\omega)}{G} \right|^2 \\ &= \left(4k_BT^2G\right) \cdot \left| \frac{H_{th}(\omega)}{G} \right|^2 \\ &= \frac{4k_BT^2}{G} \left|H_{th}(\omega)\right|^2 \end{aligned} \tag{3.47}$$

The graphical representation of Eq. 3.47 is shown in the following block diagram (Fig. 3.11).

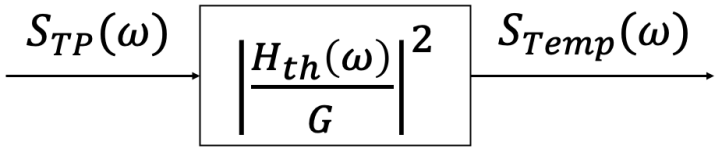

Figure 3.11: Temperature fluctuation block diagram representing Eq. 3.48.

It is important to emphasize that temperature fluctuation noise $S_{Temp}(\omega)$ represents the fundamental noise limit for all thermal-based sensors (i.e., thermopiles, bolometers, pyroelectric detectors, and NMR-based thermal sensors, as in this work). This is because all thermal-based sensors rely on reading the temperature rise of the sensing element upon thermal absorption; any thermal signal that results in a temperature change below $S_{Temp}(\omega)$ will be overshadowed by this noise and therefore cannot be measured.

In the context of thermal sensing using a nanomechanical resonator, we can convert $S_{Temp}(\omega)$ to the frequency domain using the temperature coefficient of fractional

frequency shift, α:

$$S_{y,th}(\omega) = S_{Temp}(\omega) \cdot \alpha^2 = \frac{4k_B T^2 \alpha^2}{G} |H_{th}(\omega)|^2. \tag{3.48}$$

Here, $S_{y,th}$ represents the fractional frequency fluctuation induced by temperature fluctuation, with units of 1/Hz.

So far, the 1D lumped thermal model has helped us derive the fundamental temperature fluctuation noise $S_{y,th}$. To calculate the thermal characteristic quantities (i.e., G, τ_{th}) in a membrane resonator, we must use the 2D heat equation, which will be introduced in the next section.

3.6 2D continuum thermal model

The content in this subsection is directly from my first published paper in 2020, *Phys. Rev. Appl. 14 (2), 024072 (2020)* [50]. This work was done during my MASc.

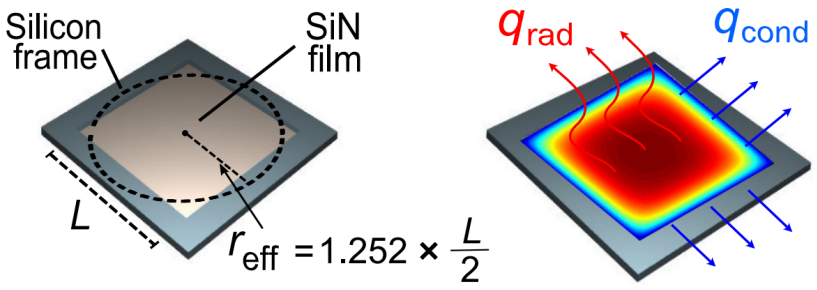

Figure 3.12: Schematic of a SiN membrane resonator exchanging heat with the environment via solid-state conduction and radiation [50].

Understanding the thermal coupling between the membrane NMR and its environment is essential for the application of thermal radiation sensing. During operation, NMRs are typically placed in a high-vacuum environment where the environmental pressure can be as low as $\sim 10^7$ Torr, making convective heat transfer negligible. Therefore, by solely considering conductive q_{cond} and radiative heat flux q_{rad}, the steady-state heat equation for a membrane NMR upon thermal absorption q_{absorb} can be expressed as [135]:

$$-k\nabla^2 T + \dot{q}_{rad} = \dot{q}_{absorb}. \tag{3.49}$$

Here, we normalize heat flux (in W) by membrane volume V for simplicity, where $\dot{q} = q/V$ (in W/m^3). T is the location-dependent temperature profile of the membrane and k is the membrane thermal conductivity. $\dot{q}_{rad}$ can be expressed as $[2\sigma_{SB}\varepsilon(T^4 - T_\infty^4)]/h$, where h is membrane thickness, σ_{SB} is the Stefan-Boltzmann constant, ε is the total hemispherical emissivity of membrane NMR, the factor of 2 accounts for radiative heat transfer occurring on both sides of the NMR and T_∞ represents the environment temperature (e.g., room temperature at ~ 300 K).

Due to the ultra-thin profile (i.e., 50 to 100 nm thick) of typical membrane NMRs [27, 50,136], it is reasonable to disregard thickness-dependent temperature profiles, making T depend solely on the in-plane location. Here, we assume the temperature profile depends only on the radius in cylindrical coordinates, which simplifies Eq. 3.49 into a 1D ordinary differential equation as follows:

$$-\frac{1}{r}\frac{d}{dr}[kr\frac{dT(r)}{dr}] + \dot{q}_{rad} = \dot{q}_{absorb}. \tag{3.50}$$

To obtain a closed-form analytical solution for Eq. 3.50, the term that represents the radiative heat transfer that contains higher order variable $T(r)^4$ must be linearized. Therefore, we assume small temperature change of NMRs occur during thermal sensing application (e.g., < 10 K) in which $\dot{q}_{rad}$ can be approximated as:

$$\dot{q}_{rad} \approx \frac{8\sigma_{SB}\varepsilon T_{\infty}^3}{h}[T(r) - T_{\infty}]. \tag{3.51}$$

Due to the significantly higher thermal conductivity of the silicon substrate compared to that of the typical ultra-thin membrane NMR it supports, it is reasonable to set the boundary condition for Eq. 3.50 to the environmental temperature T_{∞}. By plugging the linearized $\dot{q}_{rad}$ into Eq. 3.50 and applying the boundary condition, we obtain the steady-state temperature profile of a circular membrane NMR with a radius r_0 as follows:

$$T(r) = [1 - \frac{I_1(\beta r)}{I_0(\beta r_0)}]\frac{\dot{q}_{absorb}}{k\beta^2} + T_{\infty}, \tag{3.52}$$

where

$$\beta = \sqrt{\frac{8\sigma_{SB}\varepsilon T_{\infty}^3}{kh}}, \tag{3.53}$$

and I_N represents Nth-order modified Bessel function of the first kind [137]. Note that Eq. 3.52 can also be used for a square membrane NMR with side length L by setting an effective radius ($r_{eff} = 1.252L/2$ [50]).

Using Eq. 3.52, one can conveniently compute that, upon thermal absorption, the heat flux q_{cond} (in W) exits the membrane via solid-state conduction in accordance with Fourier's law of conduction [135]:

$$q_{cond} = -2\pi r_0 hk \frac{\partial T(r)}{\partial r}\bigg|_{r=r_0}, \tag{3.54}$$

where $\frac{\partial T(r)}{\partial r}\Big|_{r=r_0}$ represents the local temperature gradient at the edge of the membrane. In addition, radiation (q_{rad}) can also contribute to channeling heat out of the membrane upon thermal absorption. According to the conservation of energy, we have:

$$q_{absorb} = q_{cond} + q_{rad}. \tag{3.55}$$

To assess the fraction of heat transfer occurring via radiation, we define a key quantity x_{rad} as q_{rad}/q_{absorb}. When a membrane's $x_{rad} \approx 1$, its thermal coupling with the environment is dominated by thermal radiation, which is an important factor in achieving the fundamental detectivity limit [3, 5, 50]. By re-arranging Eq. 3.55, we compute x_{rad} as follows:

$$x_{rad} = \frac{q_{rad}}{q_{absorb}} = 1 - \frac{q_{cond}}{q_{absorb}} = 1 - \frac{2}{\beta r_0}\frac{I_1(\beta r_0)}{I_0(\beta r_0)}. \tag{3.56}$$

Using x_{rad}, one can conveniently calculate the total thermal conductance G for a membrane resonator as follows:

$$G = \frac{G_{rad}}{x_{rad}} = \frac{2 \cdot 4L^2 \sigma_{SB} \varepsilon T_\infty^3}{x_{rad}}, \tag{3.57}$$

where G_{rad} is the thermal conductance purely attributed to radiation occurring on both sides of the membrane. With the total thermal conductance G calculated, the thermal time constant can be readily obtained as $\tau_{th} = C_{th}/G$.

3.7 Summary of important noise sources in temperature-sensitive nanomechanical resonators

Up to this point, using the 1D lumped mechanical (Sec. 3.1.3) and thermal models (Sec. 3.5), we have successfully derived and explained the origins of both thermomechanical noise and temperature fluctuation noise in temperature-sensitive NMRs operating under high-vacuum and room-temperature conditions. However, other sources of frequency noise, such as those arising from readout instrument imperfections and Duffing nonlinearity, have not been discussed so far. In this section, we summarize the important noise contributions by dividing them into two categories: fundamental and non-fundamental, in the context of thermal sensing. We aim to describe these noise sources in their intrinsic forms, excluding the noise filtering effects imposed by closed-loop frequency tracking schemes.

3.7.1 Fundamental noise in thermal sensing

Like all thermal-based sensors which probe thermal radiation sensing via the sensing element temperature change, NMRs thermal sensing performance is fundamentally limited by temperature fluctuation noise. In the context of thermal sensing using NMRs, this noise is expressed as [6, 138]:

$$S_{y,th}(\omega) = \frac{4k_B T^2 \alpha^2}{G} |H_{th}(\omega)|^2, \tag{3.58}$$

where k_B is the Boltzmann constant, $H_{th}(\omega)$ is the intrinsic thermal filter of the NMR, calculated as $1/(1 + j\omega\tau_{th})$ where τ_{th} is the thermal time constant. Note that $S_{y,th}$ is in the unit of 1/Hz, representing the one-sided noise spectral density in fractional frequency shift. Minimizing all other non-fundamental noise sources to a negligible level compared to $S_{y,th}$ is crucial for reaching optimal thermal sensing performance (i.e., fundamental

detectivity limit at room temperature $D^* \approx 1.8 \times 10^{10}$ cm $\cdot \sqrt{\text{Hz}}/\text{W}$ [2]).

3.7.2 Non-fundamental noises in thermal sensing

Under ultra-high vacuum and room temperature environment conditions, frequency fluctuation originating from surface diffusion and absorption-desorption have been shown to be negligible [35, 36]. This, therefore, makes the thermomechanical noise and instrument readout noise the two major non-fundamental noises that harm NMRs thermal sensing performance.

3.7.3 Thermomechanical noise

Thermomechanical fluctuation (in Hz^{-1}), originating from the environmental thermal energy ($k_B T/2$) at a given eigenfrequency ω_r, can be expressed as [39, 120]:

$$S_{y,tmech}(\omega) = \frac{2k_B T}{m_{eff}\omega_r^3 Q A_{rss}^2} |H_{mech}(\omega)|^2, \tag{3.59}$$

where m_{eff} is the effective mass, Q is the mechanical quality factor and A_{rss} is the vibration amplitude of the NMR. $H_{mech}(\omega)$ is the intrinsic mechanical filter of the NMR, calculated as $1/(1 + j\omega\tau_{mech})$ where τ_{mech} is the mechanical time constant.

3.7.4 Instrument readout noise

Unlike temperature fluctuation and thermomechanical noise, which are intrinsic to the resonator' s own physics (e.g., mechanical and thermal models), noises associated with imperfections occurring during the transduction process are also detrimental to the frequency stability of NMRs. We therefore refer to this as instrument readout noise. Note that in this work, we adopt the formulation of instrument readout noise from [120] and [6], which lumps all instrument noise sources into a single term, regardless of their physical origin (e.g., electrical or optical), for convenience. Here, the instrument readout

noise is in in units of Hz^{-1} and expressed as:

$$S_{y,read}(\omega) = \frac{S_{x,read}}{2Q^2 A_{rss}^2} |H_{demod}(\omega)|^2, \tag{3.60}$$

where $S_{x,read}$ (in m^2/Hz) is the displacement noise floor of the readout instrument which must be measured during experiment. $H_{demod}(\omega)$ accounts for the readout instrument filter (e.g., lock-in amplifier demodulation filter), calculated as $1/(1 + j\omega\tau_{demod})$ where τ_{demod} is the readout instrument demodulation speed. It is worth noting that $S_{x,read}$ is fundamentally a displacement noise, similar to thermomechanical fluctuations. Therefore, Eq. 3.60 converts this displacement noise into the frequency domain using Robins' formula [139]. This type of displacement noise, which manifests itself as phase noise, is typically referred to as additive phase noise. To minimize the additive phase noise, one can optimize for both Q and A_{rss}.

3.7.5 Critical amplitude for the onset of Duffing nonlinearity

Although an increase in A_{rss} can help minimize non-fundamental additive phase noise during thermal sensing, A_{rss} cannot be increased indefinitely. Beyond a certain point A_{crit}, it starts to trigger Duffing nonlinearity [140, 141], which is also detrimental to the frequency stability of NMRs. According to well-established literature [6, 142], A_{crit} is generally inversely proportional to the quality factor Q, and directly proportional to the resonator's effective stiffness k_{eff} and characteristic length L. However, a recent study [143] offers a new perspective on this topic in the context of resonators operating under closed-loop frequency tracking. Specifically, it divides frequency fluctuations arising from Duffing nonlinearity into two regimes (i.e., fast and slow), each associated with a corresponding critical amplitude, A_{crit}. This newly proposed model incorporates the effect of sampling rate F_s. In the 'fast sensing' regime where sampling occurs much faster than the mechanical response time of the resonator (i.e., $F_s \gg 1/(2\pi\tau_{mech})$), the critical

amplitude above which frequency stability begins to deteriorate due to nonlinearity is given by:

$$A_{crit|fast} = \frac{2}{\sqrt[4]{3}}\sqrt{\frac{F_s}{\omega_r \beta}}, \tag{3.61}$$

where β is the Duffing coefficient which can be measured experimentally, in units of m^{-2}. In the 'slow sensing' regime, $A_{crit|slow}$ is calculated as $A_{crit} \cdot \sqrt[4]{3}/2$, where A_{crit} is taken from previously established work [6, 142], and is independent of the sampling rate F_s. It is worth noting that Duffing nonlinearity-induced amplitude noise cannot be simply converted to phase noise using Robins' formula, as was done for additive phase noise. This type of noise is not the focus of this work and requires further experimental and theoretical investigation.

3.7.6 Conversion between noise figure conventions

3.7.6.1 Fractional frequency spectral density $\longrightarrow$ Allan deviation

Fractional frequency noise of nanomechanical resonators is typically characterized using a metrology standard known as Allan deviation [144], and is defined as:

$$\sigma_A(\tau) = \sqrt{\frac{1}{2(N-1)}\sum_{i=1}^{N}\left(y_{i+1,\tau} - y_{i,\tau}\right)^2}, \tag{3.62}$$

where $y_{i,\tau}$ represents ith fractional frequency $y(t)$ averaged over time duration τ. Note that σ_A is dimensionless. The fundamental advantage of using σ_A to characterize frequency noise lies in its ability to distinguish between different noise types across sampling time scales τ, and to clearly identify which noise source dominates in each sampling time regime. During the experiment, the fractional frequency time series $y(t)$ can be recorded, and then converted numerically into σ_A using Eq. 3.62.

Note that the theoretical one-sided S_y (in Hz^{-1}) calculated using Eq. 3.58,3.59 and

3.60 can be converted into σ_A using the following integral:

$$\sigma_A(\tau) = \frac{2}{\sqrt{\pi}\tau}\left[\int_0^\infty \left(\frac{\sin\left(\frac{\omega\tau}{2}\right)}{\omega^2}\right)^4 S_y(\omega)\, d\omega\right]^{\frac{1}{2}}. \tag{3.63}$$

Care must be taken when dealing with a two-sided S_y: we must either modify the term $2/\sqrt{\pi}\tau$ to $4/\sqrt{\pi}\tau$, or re-evaluate the integral from $-\infty$ to ∞. In a practical experimental setting, the resonator's fractional frequency noise spectral density S_y can also be directly extracted from a recorded frequency time series using a Fast Fourier Transform (FFT) with appropriate signal de-trending.

3.7.6.2 Phase spectral density $\longrightarrow$ Fractional frequency spectral density

Frequency fluctuations are also often presented in the form of phase spectral density $S_\phi(\omega)$, in units of rad^2/Hz. One can convert $S_\phi(\omega)$ to $S_y(\omega)$ as follows:

$$S_y(\omega) = S_\phi(\omega) \cdot (\frac{1}{\tau_{mech}})^2 \cdot (\frac{1}{\omega_r})^2, \tag{3.64}$$

where τ_{mech} is the resonator mechanical time constant, expressed as $\tau_{mech} = 2Q/\omega_r$. Conveniently, Eq. 3.64 simplifies to

$$S_y(\omega) = S_\phi(\omega) \cdot \frac{1}{4Q^2}. \tag{3.65}$$

3.8 Noise filtering effect of closed-loop frequency tracking

In practice, despite typically being operated in controlled environments (e.g., pressure, humidity, temperature, etc.), nanomechanical resonators—due to their ultrasensitive nature (i.e., high Q and ultra small mass)—almost invariably suffer from frequency drift that exceeds their mechanical bandwidth by orders of magnitude. Therefore, operating

them in an open-loop (feedback-free) manner makes it difficult to detect perturbation of interest, such as thermal radiation in this work, as the signal can be overshadowed by drift. Therefore, we use a closed-loop frequency tracking scheme—phase-locked loop (PLL)—in this work, which allows the resonator to be continuously driven at its instantaneous resonance frequency, ω_r. Other closed-loop frequency-tracking schemes, such as the self-sustaining oscillator (SSO) with positive feedback, are also often used and are under active investigation. In fact, a recent work [48] has shown that SSO achieves a noise figure similar to that of PLL frequency-tracking schemes.

In Fig. 3.13, we present a block diagram illustrating the noise filtering effect imposed by the closed-loop frequency tracking scheme. Note that this block diagram is adapted from Demir *et al.* [120] and only considers the filtering effect on additive phase noise sources (i.e., thermomechanical noise $S_{y,tmech}$ and instrument readout noise $S_{y,read}$). Here, the noise inputs are unfiltered thermomechanical noise $\overline{S_{y,tmech}}$, and instrument readout noise $\overline{S_{y,read}}$. The overline donation denotes the white noise magnitude before filtering, i.e., $\overline{S_y} = S_y(0)$.

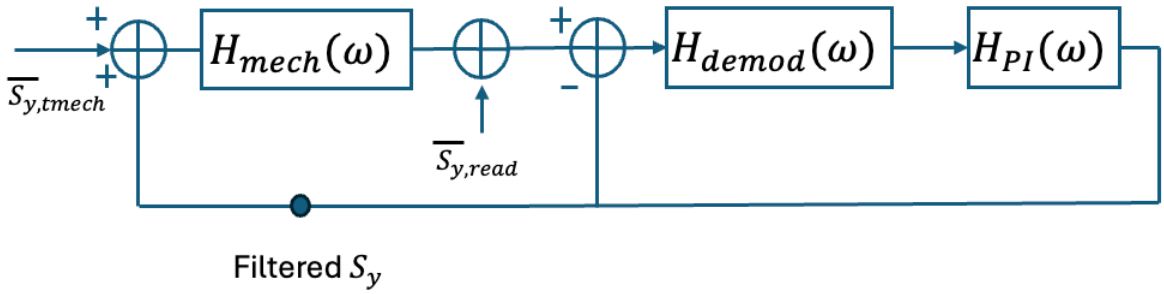

Figure 3.13: Block diagram of the closed-loop frequency tracking scheme, showing the filtering paths for thermomechanical and instrument readout noise.

The block diagram in Fig. 3.13 can be viewed in two parts: on the left is the resonator's mechanical frequency response (i.e., $H_{mech}(\omega)$), and on the right is a negative feedback loop encompassing the demodulation process (i.e., $H_{demod}(\omega)$) together with the PLL frequency tracking controller (i.e., $H_{PI}(\omega)$). Expressions for $H_{mech}(\omega)$ and $H_{demod}(\omega)$ were introduced in the previous section, while $H_{PI}(\omega)$ is simply the transfer function of

a proportional-integral (PI) controller:

$$H_{PI}(\omega) = K_p + \frac{K_i}{j\omega}, \tag{3.66}$$

where K_p and K_i are the proportional and integral gains of the controller, respectively. In the context of PLL frequency tracking, $K_p = 1/\tau_{pll}$ represents the PLL bandwidth, and $K_i = 1/(\tau_{pll} \cdot \tau_{mech})$ represents the combined effect of the resonator' s mechanical response and the PLL speed. By simplifying the block diagram node by node from $\overline{S_{y,tmech}}$ to the filtered S_y (see Fig. 3.13), one can obtain the transfer function that describes the PLL filtering effect on thermomechanical noise [39, 40, 120]:

$$H_{mech}^{PLL}(\omega) = \frac{(j\omega K_p + K_i)H_{demod}(\omega)}{(j\omega)^2 + \frac{j\omega}{\tau_{mech}} + (j\omega K_p + K_i)H_{demod}(\omega)}. \tag{3.67}$$

In turn, since $\overline{S_{y,tmech}}$ and $\overline{S_{y,read}}$ are only separated by $H_{mech}(\omega)$, the PLL filtering effect on instrument readout noise is simply:

$$H_{read}^{PLL}(\omega) = \frac{H_{mech}^{PLL}(\omega)}{H_{mech}(\omega)}. \tag{3.68}$$

The block diagram in Fig. 3.13 models thermomechanical noise and instrument readout noise as two separate disturbance inputs, which implies that these two noise sources are independent of each other. It should be emphasized that the PLL filtering effect on temperature fluctuation noise has not been clearly understood to date, which is therefore a main point of investigation in this work.

4. Temperature Fluctuation Noise

4.1 Article 1: Initial investigation of temperature fluctuation noise

4.1.1 Foreword

This section presents a published journal article ***Appl. Phys. Lett. 122, 193501 (2023) [136]*** titled as **Demonstration of Frequency Stability limited by Thermal Fluctuation Noise in Silicon Nitride Nanomechanical Resonators** in its original form. Note that *thermal fluctuation noise* in this article refers to the same concept as temperature fluctuation noise; it is simply a different name. This article aims to characterize temperature fluctuation noise in an nanomechanical resonator (NMR) under a closed-loop frequency tracking scheme (i.e., phase-locked loop, PLL). To the best of our knowledge, this is also the first work showing signs that an NMR can reach an overall noise profile dominated by temperature fluctuation noise.

This work marks the beginning of our investigation into temperature fluctuation noise under the PLL frequency tracking scheme. It should be emphasized that this paper contains later-identified mistakes in the theoretical formulation of temperature fluctuation noise (i.e., Eq. 4.2) and the corresponding filtering effect imposed by the PLL (i.e., Eq. 4.7). These errors in the theoretical model are subsequently corrected in **Chapter. 4.2** by **(Article 2)**, which presents our latest findings on this topic. The general concept and preliminary experimental results remain valid, and the article conclusions remain intact.

Author list: Chang Zhang, Raphael St-Gelais.

4.1.2 Author Contributions

Chang Zhang: Lead investigator of this article; responsible for all experimental work and drafting the manuscript.

Raphael St-Gelais: Principal investigator; led the conceptual development of the article, provided guidance during the experiments, and assisted in writing the manuscript.

4.1.3 Abstract

The frequency stability of nanomechanical resonators (NMR) dictates the performance level of many state-of-the-art sensors (e.g., mass, force, temperature, radiation) that relate an external physical perturbation to a resonance frequency shift. While this is obviously of fundamental importance, accurate models and understandings of sources of frequency instability are not always available. The contribution of thermomechanical noise to frequency stability has been well studied in recent years and is often the fundamental performance limitation. Frequency stability limited by thermal fluctuation noise has attracted less interest but is nevertheless of fundamental importance notably in temperature sensing applications. In particular, temperature-sensitive NMR have become promising candidates for replacing traditional bolometers in infrared radiation sensing. However, reaching the ultimate detectivity limit of thermal radiation sensors requires their noise to be dominated by fundamental thermal fluctuation, which has not been demonstrated to date. In this work, we first develop a theoretical model for computing the frequency stability of NMR by considering the effect of both additive phase noise (i.e., thermomechanical, and experimental detection noise) and thermal fluctuation noise in a close-loop frequency tracking scheme. We thereafter validate this model experimentally and observe thermal fluctuation noise in SiN drum resonators of various sizes at room temperature. Our work shows that by using resonators of specific characteristics—such as high temperature sensitivity, high mechanical quality factors, and high mass-to-thermal-

conductance ratio—one can minimize additive phase noise below thermal fluctuation noise. This paves the way for uncooled NMR-based radiation sensors that can reach the fundamental detectivity limit of thermal radiation sensing and outperform existing technologies.

4.1.4 Introduction

Nanomechanical resonators (NMR) frequency stability is the fundamental quantity dictating the performance of sensors measuring physical signals through resonance frequency shifts (e.g., mass [145–148], force [149, 150], and thermal [134, 151–155] sensors). Hence, identifying the source of noise that dominates frequency fluctuations in the absence of a signal is fundamental for understanding the performance limit of NMR. Early theoretical investigation of various sources of noise in NMR was proposed by Vig *et al.* [156] and Cleland *et al.* [36]. These theoretical works provided a comprehensive picture of multiple sources of noise in NMR, including surface diffusion, absorption-desorption, thermomechanical, detection, and thermal fluctuation noises. Thermomechanical noise was later identified as a dominant source of noise in many cases. This noise originates from the thermal energy ($k_BT/2$) of each resonator eigenmode, causing random mechanical fluctuations that are detrimental to frequency measurement. Substantial efforts were therefore devoted to resolving the frequency stability limit imposed by thermomechanical noise [157–160], and to predicting its effect after processing by various frequency tracking schemes. Demir [120] recently provided a theoretical model for predicting the frequency stability of resonators, which considers the combined effect of thermomechanical and detection noise in commonly employed phase-locked loop (PLL) frequency tracking. Such theoretical model was later validated experimentally by Sadeghi *et al.* [121], confirming that thermomechanical and detection noises can be the dominant noises in high-stress silicon nitride string resonators. While thermomechanical noise was proven to dominate frequency fluctuation in many high-Q factor NMR, achiev-

ing regimes in which thermal fluctuation noise would dominate remains of high interest especially in temperature sensing applications. Thermal fluctuation noise originates from random exchanges of heat between the NMR and its surrounding thermal bath. These exchanges cause the NMR temperature (and thus frequency) to fluctuate over bandwidths and amplitudes determined by the system thermal conductance and heat capacity. In temperature sensors, the smallest temperature that theoretically can be measured is ultimately dictated by thermal fluctuation noise. This limit is of particular interest in the field of radiation detection, as it dictates the fundamental detectivity limit that can ultimately be reached by thermal-based radiation detectors [2,161], or bolometers. Traditional bolometers that rely on temperature coefficient of resistance for thermal radiation detection face a trade-off [2] in simultaneously achieving low thermal conductance (i.e., high sensitivity to radiation) and high electric conductance (i.e., minimizing Johnson-Nyquist noise). Such goal is challenging, as both thermal and electrical conductances are typically proportional to each other (see Wiedemann-Franz Law). NMR-based thermal radiation detectors [134, 151–155] that rely on resonant sensing scheme break this trade-off, potentially allowing operation limited only by fundamental thermal fluctuation noise. However, existing NMR-based thermal radiation detectors were found to be limited instead by other non-fundamental noises such as thermomechanical, detection [134, 151, 153–155], or flicker noise [152].

In the current work, we experimentally demonstrate low-stress, high Q-factor SiN drum resonators in which frequency instability is minimized down to fundamental thermal fluctuation noise at room temperature. We also include thermal fluctuation noise with recently proposed models for frequency stability within a closed-loop frequency tracking scheme [120]. Our results and model, therefore, pave the way for radiation sensors that could reach the fundamental detectivity limit of physical radiation detectors.

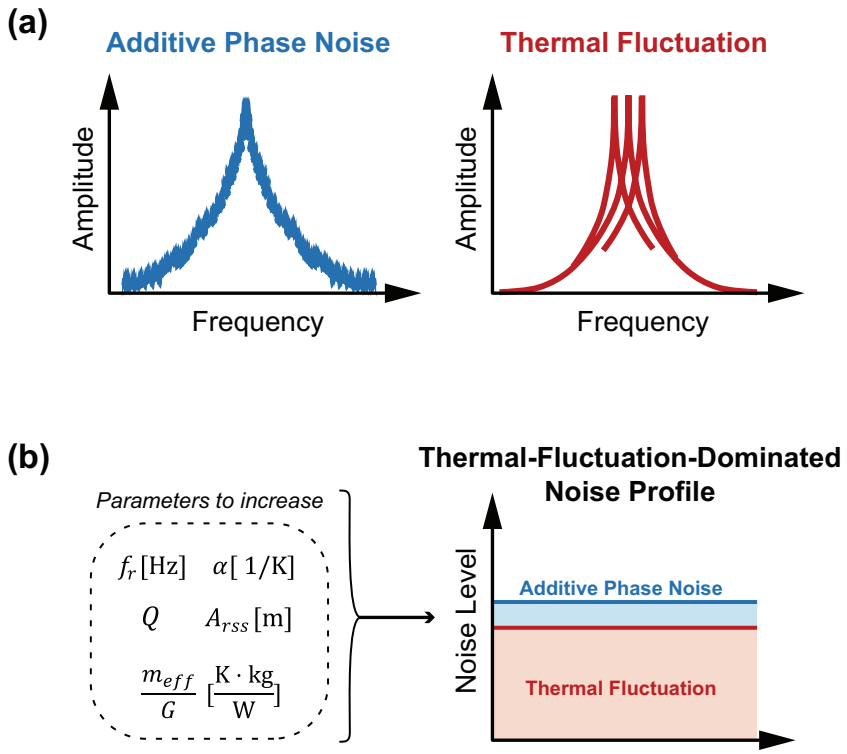

Figure 4.1: **Additive phase noise vs. thermal fluctuation** (a) Illustration of the characteristic difference between additive phase noise and thermal fluctuation. (b) Increase in temperature coefficient α, resonance frequency f_r, mechanical Q-factor, vibration amplitude A_{rss}, mass-to-thermal-conductance ratio m_{eff}/G of the nanomechanical resonator (NMR) minimizes additive phase noise relative to thermal fluctuation noise.

4.1.5 Theory

We separate the sources of frequency fluctuation in a drum resonator into two categories, namely, the additive phase noise $S_{y,add}(\omega)$ which includes thermomechanical $S_{y,mech}(\omega)$ and detection noise $S_{y,det}(\omega)$; and thermal fluctuation noise $S_{y,th}(\omega)$. Here y represents fractional frequency $\langle \delta f/f_r \rangle$ fluctuations. We also define the intrinsic noise spectral density $S_y^{int}(\omega)$ before it is modified by the experimental frequency measurement scheme (e.g., open-loop, phase-lock loop frequency tracking, or self-sustained oscillation). For a given eigen frequency f_r, the intrinsic frequency fluctuation caused by additive

phase noise $S^{int}_{y,add}(\omega)$ is therefore [120]:

$$\begin{aligned} S^{int}_{y,add}(\omega) &= S^{int}_{y,mech}(\omega) + S_{y,det}(\omega) \\ &= \frac{k_B T}{8\pi^3 m_{eff} f_r^3 Q A_{rss}^2} |H_{mech}(j\omega)|^2 \\ &+ \frac{k_B T}{8\pi^3 m_{eff} f_r^3 Q A_{rss}^2} \kappa_d^2 \\ &= \frac{k_B T}{8\pi^3 m_{eff} f_r^3 Q A_{rss}^2} (|H_{mech}(j\omega)|^2 + \kappa_d^2), \end{aligned} \tag{4.1}$$

where $H_{mech}(j\omega) = 1/(1 + j\omega\tau_{mech})$ is a one-pole low pass filter accounting for the mechanical time constant $\tau_{mech} = Q/(\pi f_r)$ of the resonator, k_B is the Boltzmann constant, T is the eigenmode temperature, m_{eff} is the mode effective mass, Q is the mechanical quality factor, A_{rss} is the vibration amplitude in steady-state and κ_d is a dimensionless parameter scaling the level of detection noise relative to thermomechanical noise, as described in [120]. More specifically, thermomechanical noise is resolved above detection noise when $\kappa_d < 1$.

In turn, the intrinsic frequency fluctuation caused by thermal fluctuation [156, 161] is:

$$S^{int}_{y,th}(\omega) = \frac{2 k_B T^2 \alpha^2}{\pi G} |H_{th}(j\omega)|^2, \tag{4.2}$$

where G is the total thermal conductance [134] in W/K between the resonator and its environment, $H_{th}(j\omega) = 1/(1 + j\omega\tau_{th})$ is a one-pole filter accounting for the thermal response time $\tau_{th} = C_{th}/G$ of the resonator, and C_{th} is the heat capacity of the resonator in J/K. An analytical model for G (and hence τ_{th}) in drum resonators is developed in [134] and is used throughout this work. α is the temperature coefficient of fractional frequency shifts, in K^{-1}. For a drum resonator, a reasonable approximation ($< 20\%$ error relative

to finite element modeling [134]) of this parameter is:

$$\alpha \approx \frac{E\alpha_T}{2\sigma(1-\nu)}, \tag{4.3}$$

in which E is Young's modulus, α_T is the drum material thermal expansion coefficient, σ is the built-in tensile stress, and ν is the Poisson ratio of the drum resonator material. Note that Eq. 4.3 is only valid for drum resonators where stiffness dominated by tensile stress (i.e., not by plate rigidity). In drum resonators [6], this occurs for $\sigma > 54Eh^2/[\pi^2L^2(1-\nu^2)]$ where L is the side length and h is the thickness of the drum resonator. For our typical 3.2×3.2 mm SiN drum resonator with $\sigma = 100$ MPa, tensile stress therefore dominates over plate rigidity, with $\sigma >> 1560$ Pa. In other cases where rigidity dominates stiffness (e.g., plates, cantilevers) [162], α should be inferred from the temperature sensitivity of the Young' s modulus and resonator dimensions, or from experimental measurement. In Eq. 4.2, T denotes the drum resonator material temperature, whereas T in Eq. 4.1 denotes the temperature of the eigenmode of frequency f_r. We use the symbol T interchangeably in this work since both are assumed to be ≈ 300 K.

A key difference between the additive phase noise and thermal fluctuation noise is schematized in Fig. 4.1(a), in which the additive phase noise manifests itself as amplitude fluctuation, which then contributes to the frequency noise via Robins' formula [139]. Conversely, thermal fluctuations make the resonance peaks of the NMR fluctuate directly in the frequency domain by affecting the stiffness of the drum material. We note that one can change the level of additive phase noise by utilizing different eigenmodes of the resonators (see Eq. 4.1) since f_r, Q are mode-dependent. Likewise, additive phase noise can be minimized by increasing the vibration amplitude A_{rss} (within the linear actuation regime). On the contrary, mode and amplitude changes do not affect the level of thermal fluctuation (see Eq. 4.2), which depends primarily on drum resonator geometric, material and heat transfer properties (e.g., α and G).

To compare the relative contributions of $S^{int}_{y,mech}(\omega)$ and $S^{int}_{y,th}(\omega)$ with respect to the overall frequency fluctuation, we define a dimensionless ratio γ:

$$\begin{aligned}\gamma &= \frac{S^{int}_{y,th}(0)}{S^{int}_{y,mech}(0)} \\ &= 16\pi^2 TQ\frac{m_{eff}}{G}\cdot\alpha^2 A^2_{rss} f_r^3\end{aligned} \tag{4.4}$$

This ratio ignores, for simplicity, the effect of both thermal $H_{th}(j\omega)$ and mechanical $H_{mech}(j\omega)$ response filters by setting $\omega = 0$. A value of $\gamma \approx 1$ indicates thermal fluctuation and additive phase noise are at a similar level. If γ is significantly larger than 1 and detection noise is minimized (i.e., $\kappa_d << 1$), a thermal-fluctuation-dominated noise profile can be achieved.

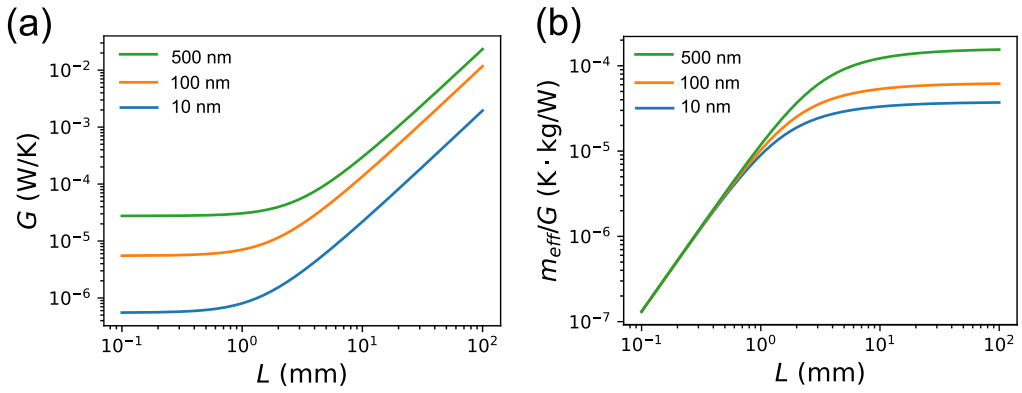

Figure 4.2: **Effect of dimensions on heat transfer quantities in silicon nitride drum resonators,** namely (a) G and (b) $\frac{m_{eff}}{G}$.

By examining γ, we find that thermal-fluctuation-dominated noise profile can be achieved by maximizing the values of Q, $\frac{m_{eff}}{G}$, α, A_{rss} and f_r. Among these listed parameters, the mass-to-thermal-conductance ratio $\frac{m_{eff}}{G}$ is likely the most unintuitive. Hence, in Fig. 4.2, we illustrate this ratio as a function of the dimensions of a square SiN drum resonators of side length L and thickness t. Values of G are presented in Fig. 4.2(a) and are calculated using the model developed in [134] which includes con-

ductive and radiative heat transfer. We note that for relatively small drum resonators ($L < 1$ mm) where heat transfer occurs mostly by conduction, both G and m_{eff} scale with the thickness, such that t cancels out in the $\frac{m_{eff}}{G}$ ratio [see Fig. 4.2(b)]. Conversely, as $L > 1$ mm, radiative heat transfer dominates, and L now cancels, making the curves plateau in Fig. 4.2(b).

In summary, considering this trend in $\frac{m_{eff}}{G}$ and the expression of γ, we find that minimizing additive phase noise below thermal fluctuation requires (i) a temperature sensitive resonator (i.e., high α) which can be maximized using a low-stress material as suggested in Eq. (4.3), (ii) a large drum resonator (i.e., large L) to maximize $\frac{m_{eff}}{G}$, (iii) a high order (i.e., high f_r) and high Q eigenmode, and (iv) excitation at high amplitude A_{rss} within the limits of linear actuation. We finally note that, despite the trend observed in Fig. 4.2(b), increasing t beyond ≈ 100 nm to maximize $\frac{m_{eff}}{G}$ is likely not a practical approach since high t can also be detrimental to Q-factor [122, 123].

To evaluate the spectral density of the frequency fluctuations $S_y(\omega)$ in a practical experimental setting, we must also consider the effect of the measurement scheme. A phase-locked loop (PLL) frequency tracking scheme, such as in the current work, includes a proportional-integral controller with proportional gain K_p and integral gain K_i, and an input demodulator filter of time constant τ_{demod}. As shown in [120], the PLL frequency tracking scheme imposes filters on the additive phase noises of the resonators (i.e., the thermomechanical and detection noises):

$$H_{mech}^{PLL}(j\omega) = \frac{(j\omega K_p + K_i)H_L(j\omega)}{-\omega^2 + \frac{j\omega}{\tau_{mech}} + (j\omega K_p + K_i)H_L(j\omega)}, \tag{4.5}$$

$$H_{det}^{PLL}(j\omega) = \frac{H_{mech}^{PLL}(j\omega)}{H_{mech}(j\omega)}, \tag{4.6}$$

where $H_L(j\omega) = 1/(1 + j\omega\tau_{demod})$ is the demodulator filter. Since $S_{y,mech}(\omega)$ and $S_{y,th}(\omega)$ are both white noises, the PLL frequency tracking scheme imposes the same filtering

effect on them, with the only difference being the time constant τ_{th}:

$$H_{th}^{PLL}(j\omega) = \frac{(j\omega K_p + K_i)H_L(j\omega)}{-\omega^2 + \frac{j\omega}{\tau_{th}} + (j\omega K_p + K_i)H_L(j\omega)}. \tag{4.7}$$

We then incorporate the PLL transfer functions (Eq. 4.5-4.7) with $S_{y,add}^{int}(0)$ and $S_{y,th}^{int}(0)$ to obtain the noise after processing by the PLL frequency tracking:

$$S_{y,add}^{PLL}(\omega) = S_{y,mech}^{int}(0)|H_{mech}^{PLL}(j\omega)|^2 + S_{y,det}(0)|H_{det}^{PLL}(j\omega)|^2, \tag{4.8}$$

$$S_{y,th}^{PLL}(\omega) = S_{y,th}^{int}(0)|H_{th}^{PLL}(j\omega)|^2. \tag{4.9}$$

Finally, the overall fractional frequency fluctuation $S_y(\omega)$ of a resonator under the PLL frequency tracking scheme is simply $S_y(\omega) = S_{y,add}^{PLL}(\omega) + S_{y,th}^{PLL}(\omega)$.

4.1.6 Methods & Results

SiN drum resonators used in this work are fabricated using the process provided in [161]. During characterization, the SiN drum resonators are mounted magnetically onto a steel plate via three pairs of spherical magnets as shown in Fig. 4.3(b) and exited mechanically via a ceramic piezo actuator mounted on the other side of the steel plate [see Fig. 4.3(c)]. The magnet mounting method provides minimum contact area between the mounts and the chip, thus minimizing mechanical dissipation. We place the SiN drum resonators inside of a custom-built, high-vacuum (8×10^{-7} Torr typical operating pressure) chamber to minimize air damping (i.e., maintaining high-Q factor) and convective heat transfer. We conduct frequency fluctuation measurements once the chamber conditions (i.e., pressure and temperature) are sufficiently stabilized. Specifically, we monitor the resonance frequency drift of SiN drum resonators after vacuum pump down from ambient. If the frequency drift remains below 0.5 Hz over a 24-hour period, we consider the chamber conditions to be stable. In our setup, the typical stabilization time

is approximately 48 hours, most likely due to its high thermal mass and the transient temperature decrease that occurs during pump down.

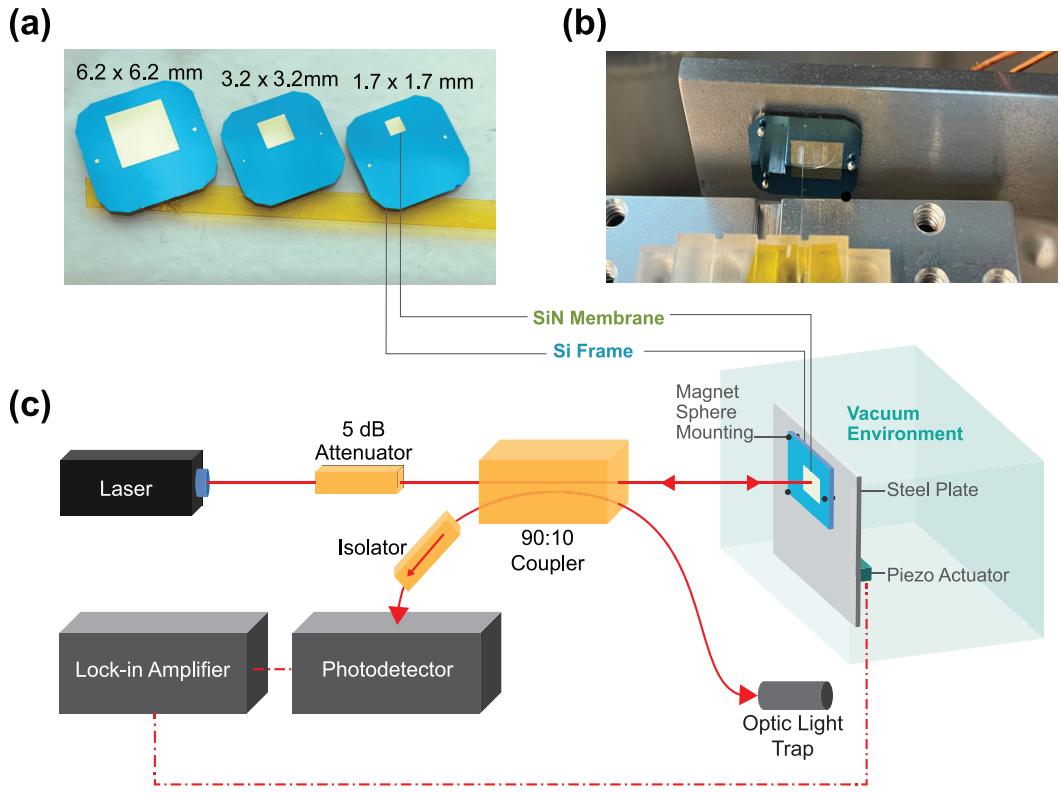

Figure 4.3: **Schematics of the experimental setup** (a) Pictures of SiN drum resonators of three different sizes characterized in this work. (b) Picture of SiN drum resonator mounted on a steel plate using magnetic spheres inside our vacuum chamber. (c) Overall schematics of the experimental setup which includes the laser interferometer located outside of the high-vacuum chamber and the actuation and mounting method of SiN drum resonator inside of the chamber.

We detect the vibration signal of the SiN drum resonator, using a laser interferometer that consists of a 1550 nm Orion^{TM} laser with built-in optical isolation, a 90:10 optical fiber coupler, 5 dB optical attenuator, optical isolator and a Thorlabs PDA20CS2 photodetector which is shown schematically in Fig. 4.3(c). The isolator at the location in Fig. 4.3(c) eliminates spurious optical cavities between the detector and the sample chip. The laser power output is set at 3.7 mW which is then attenuated to 11.7 μW prior to reaching the SiN drum resonator, via the 5 dB optical attenuator and the 90:10 optical coupler (i.e., 90% power attenuation). Laser power attenuation is critical to minimize

the effect of laser heating, as observed in a separate experiment in Appendix. A.1.

We quantify the frequency fluctuation of SiN drum resonators in this work using Allan deviation σ_A [144], a metrology standard widely used to characterize the frequency fluctuation in nanoresonators. Based on the theoretically expected spectral density of frequency fluctuation $S_y(\omega)$, we can numerically compute the theoretical σ_A via [120]:

$$\sigma_A(\tau) = \frac{2}{\sqrt{\pi}\tau}\left[\int_{-\infty}^{\infty} \frac{[\sin(\frac{\omega\tau}{2})]^4}{\omega^2} S_y(\omega)\, d\omega\right]^{\frac{1}{2}}, \tag{4.10}$$

where τ is the integration time. The asymptotic limit of σ_A (i.e., excluding all intrinsic and PLL filters) for white noises can be computed analytically as $\sqrt{S_y(0)/\tau}$, such that the asymptote specifically for thermal fluctuation noise is $\sqrt{S_{y,th}^{PLL}(0)/\tau}$.

In order to observe additive phase noise and thermal fluctuation noise over a broad range of τ, the demodulation time constant in our experiment is set to a high bandwidth ($\tau_{demod} = 3.18 \times 10^{-5}$ s) to minimize signal filtering at the lock-in input. Likewise, the PLL bandwidth is set to ≈ 5 times faster than the thermal fluctuation bandwidth ($\tau_{PLL} \approx \tau_{th}/5$) to prevent filtering of thermal fluctuation noise $S_{y,th}^{int}$ by the PLL. The corresponding K_p and K_i values for achieving this bandwidth are determined using the relations given in [120].

The geometric and material properties of the SiN drum resonators, and of the eigenmodes chosen for actuation, are decided to minimize additive phase noise related to thermal fluctuation noise according to Eq. 4.4. The drum resonators large area [i.e., $L = 1.7$ mm, 3.2 mm, 6.2 mm shown in Fig. 4.3(a)] maximizes the mass-to-thermal-conductance ratio $\frac{m_{eff}}{G}$ for the drum resonator thickness of 90 nm. The use of low-stress ($\sigma \approx 100$ MPa) SiN membrane maximizes the temperature sensitivity α via Eq. 4.3. The values of E, α_T and ν for SiN are respectively 300 GPa, 2.2×10^{-6} K^{-1} and 0.27, which result in $\alpha \approx 4.6 \times 10^{-3}$ K^{-1}. We also pick high-order eigenmodes (high f_r) having high Q-factors. Specifically, the values of f_r and Q-factors, from the smallest to largest SiN

drum resonator are respectively 137.6, 90.2, 208.6 kHz and 0.86, 1.18, 1.24 million.

Considering these drum resonator parameters, we compare, in Fig. 4.4(b), the expected Allan deviation σ_A plots for our model (labelled "ADD+TH") with that of recent model [120] that solely includes additive phase noise (labelled "ADD"). In this case, we consider a low-stress 3.2 × 3.2 mm SiN drum resonator at different levels of actuation A_{rss} and we set $\kappa_d = 0.012$ to account for typical detection noise in our experiment. We note that at small $\tau \lesssim 0.005$ s, the two models overlap with each other, which indicates that additive phase noise is dominant. More specifically, $S_{y,det}$ dominates, since $S^{int}_{y,th}$ and $S^{int}_{y,mech}$ are attenuated by their respective intrinsic filter H_{th} and H_{mech} (with $\tau_{th} = 0.095$ s and $\tau_{mech} = 4.15$ s). At intermediate integration time $0.005 \lesssim \tau \lesssim 0.07$ s, and when A_{rss} is sufficiently high, thermal fluctuation noise becomes non-negligible. In this case, theoretical σ_A plots that include thermal fluctuation converge towards an A_{rss}-independent thermal fluctuation asymptote ($\sqrt{S^{PLL}_{y,th}(0)/\tau}$) as τ increases. On the contrary, considering only additive phase noise in Fig. 4.4(b) do not exhibit amplitude-independent-converging effect.

This difference between the models is confirmed experimentally in Fig. 4.4(c), where we find that experimentally recorded σ_A match closely with our model. Conversely, the "ADD" model fails at intermediate τ values (i.e., in the "thermal fluctuation dominated region ") when A_{rss} is sufficiently high for thermal fluctuation noise to dominate. Eventually, drift occurs and systematically dominates at $\tau \gtrsim 0.07$ s. This systematic drift at larger time scale is commonly observed in NMR frequency measurements [121, 157]. Sources of the systematic drift are most often due to extrinsic environmental factors such as vacuum chambers pressure and temperature variation. In Fig. 4.4(c), we superimpose the systematic drift measured experimentally into both theoretical models (i.e., "TH" and "ADD"). This is for visualization purpose only (i.e., drift is not accounted for in the model) and the process is not repeated in subsequent figures. Note that values presented in Fig. 4.4(c) are a limited subset of the more complete data set presented in

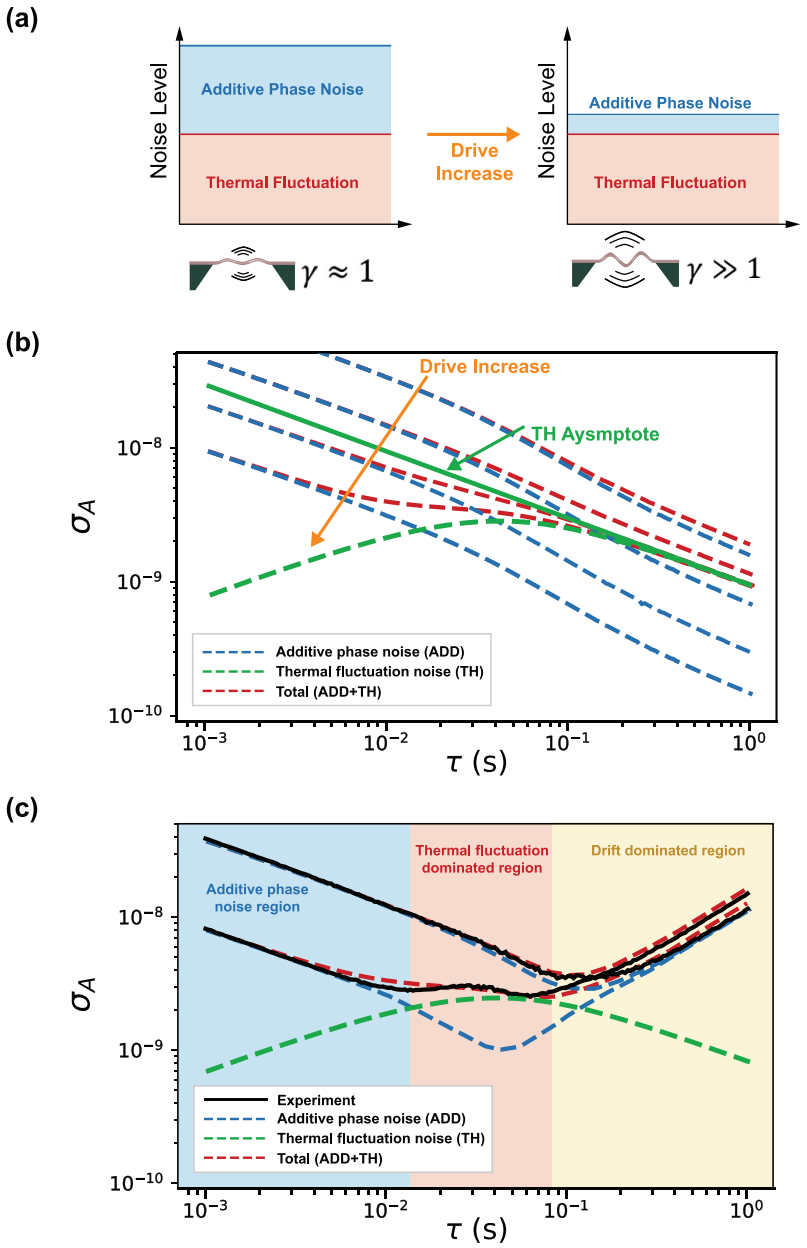

Figure 4.4: (a) Schematic of changing noise profile via drive increase. (b) Theoretical Allan deviations σ_A comparison between the model that solely considers additive phase noise (labelled "ADD"), the model that solely considers thermal fluctuation noise (labelled "TH") and the model that considers both additive phase noise and thermal fluctuation noise (labelled "ADD+TH"), for a 3.2×3.2 mm SiN drum resonator at four levels of A_{rss}. (c) Comparison of experimental Allan deviations σ_A (black solid lines) with respect to all theoretical σ_A at two levels of A_{rss}.

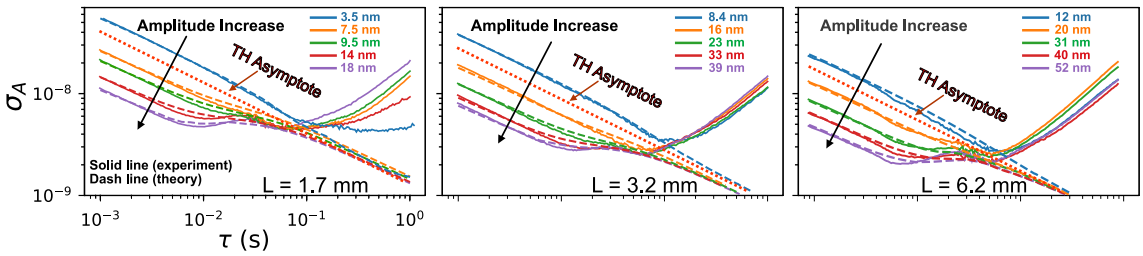

Figure 4.5: Experimental and theoretical Allan deviations σ_A for SiN drum resonators of three different sizes, at multiple vibration amplitudes A_{rss}.

Fig. 4.5. The experimental conditions and model fitting parameters are discussed below for Fig. 4.5 therefore also applies to Fig. 4.4(c).

To further validate our theoretical model, we repeat Allan deviation σ_A measurements for resonators of three different sizes (i.e., $L = 1.7$ mm, 3.2 mm, 6.2 mm) and for several drive amplitudes A_{rss} in Fig. 4.5. During experiments, we first excite the resonators at low A_{rss}, such that the experimental σ_A is overall slightly above the thermal fluctuation asymptote—i.e., additive phase noise is marginally larger than thermal fluctuation noise. We then increase A_{rss} progressively to reduce the additive phase noise. We find that all three drum resonators consistently converge towards the thermal asymptote at intermediate τ values, and when A_{rss} is sufficiently large. The convergence is then rapidly shadowed by drift at large τ.

Correspondence between the model and experiment in Fig. 4.5 was obtained by using only fit parameters that are expected from our experimental uncertainties. Two fit parameters are used for all resonators, while a third one is needed only for the largest resonator. The vibration amplitude of the resonators A_{rss} and the detection noise scaling factor κ_d are fitted for all three resonators to account for misalignment uncertainly between the location of our optical fiber and the mode vibration anti-node. This misalignment is found to underestimates A_{rss} by fitted factors of (0.87, 1.1, 2.4) for the three respective resonators sizes. Likewise, fitting κ_d yields increase factors of (50%, 30%, 10%) relative to the κ_d values expected from our measurement noise floor (≈ 0.23 pm/$\sqrt{\text{Hz}}$)

and from theoretically expected thermomechanical fluctuations. Finally, we find that for the largest resonator, the experimental thermal time constant τ_{th} must be reduced by a factor of 2 relative to the theoretically expected value. It is possible that the very high order mode used in this case lead to a higher G (lower τ_{th}) due to several mode anti-nodes being located close to the heat-dissipating silicon frame. Adding more fit parameters, such as making $H_{th}(j\omega)$ not strictly a first order low-pass filter, could potentially correct for slight mismatch between theory and model in the transition region between additive phase noise and thermal fluctuation noise (i.e., around $\tau \approx 10^{-2}$). This is not explored further, as we opt instead to minimize the number of fit parameters.

We note that our measurement in Fig. 4.5 confirms important relations between the level of thermal fluctuation relative to the membrane dimensions and mechanical properties. We first observe the level of thermal fluctuation noise (i.e., the TH asymptote vertical position) scales inversely with the drum resonator side length (i.e., with G), as predicted by Eq. 4.2 and Fig. 4.2. This as an important consequence in practice. While Eq. 4.2 and Fig. 4.2(b) suggest that large drum resonators are always better (to maximize $\frac{m_{eff}}{G}$), this is not entirely true in practice. As our membrane size increases, it becomes increasingly difficult to identify the thermal asymptote before drifts occur at higher τ. A trade-off therefore exists when designing sensors operating at the fundamental thermal fluctuation noise limit; large drum resonator should be used to maximize the $\frac{m_{eff}}{G}$ ratio up to the plateau observed in Fig. 4.2(b). However, thermal fluctuation noise limit will eventually be shadowed by drift if the resonator is too large ($L >> 3.2$ mm).

In conclusion, we present and experimentally validate a model for computing frequency stability of NMR considering the effect of both additive phase noise and thermal fluctuation noise in close-loop frequency tracking scheme. We demonstrated that by using SiN drum resonators of properly designed geometric and material properties, one can minimize additive phase noise below thermal fluctuation noise. We also identified which resonators inherent properties (e.g., thermal conduction, thermal coefficient of frequency)

most affect thermal noise, in contrast with additive phase noise that can be minimized via other parameters (e.g., drive amplitude). Our work therefore provides fundamental guidance for building thermal sensors such as nanomechanical bolometers. We provide a path for those to reach the never attained fundamental detectivity limit [2] of thermal radiation detection at room temperature, which requires sensors limited only by fundamental thermal fluctuation noise [161].

4.2 Article 2: Reaching temperature fluctuation dominated noise profile over an extended measurement bandwidth

4.2.1 Foreword

This section presents our most recent article, titled **Enhanced bandwidth in radiation sensors operating at the fundamental temperature fluctuation noise limit**. Note that the revised version of this article was ***accepted by Nano Letters*** on ***September 18, 2025***. It is currently awaiting online publication. The DOI of this article is ***https://doi.org/10.1021/acs.nanolett.5c03415***.

Building upon our initial investigation of temperature fluctuation noise-limited nanomechanical resonators NMRs presented in the previous chapter, this article refines the model in **Chapter. 4.1** that predicts temperature fluctuation under a closed-loop frequency tracking scheme. Through a set of comprehensive experiments, we not only verify the validity of the proposed frequency noise model but also unveil an undiscovered benefit of operating an NMR at the temperature fluctuation noise limit—enhanced measurement bandwidth. Specifically, we experimentally demonstrate that when the noise profile of a high-Q, hierarchical NMR is largely dominated by temperature fluctuation noise, its peak thermal sensing performance (i.e., NEP and D^*) remains largely unaffected up to 30 times the intrinsic thermal response time.

Author list: Chang Zhang, Zachary Louis-Seize, Maxime Brazeau, Timothy Hodges, Mathis Turgeon-Roy and Raphael St-Gelais.

4.2.2 Author Contributions

Chang Zhang: Lead investigator of this article; responsible for all experimental work and drafting the manuscript.

Zachary Louis-Seize: Assistant investigator; helped perform preliminary experiments.

Maxime Brazeau: Assistant investigator; helped build part of the experimental setup.

Timothy Hodges: Assistant investigator; contributed to writing part of the data acquisition code.

Mathis Turgeon-Roy: Assistant investigator; helped verify and sanity-check the mathematical equations in the article.

Raphael St-Gelais: Principal investigator; led the conceptual development of the article, provided guidance during the experiments, and assisted in writing the manuscript.

4.2.3 Abstract

Temperature-based radiation detectors are an essential tool for long optical wavelengths detection even if they often suffer from important bandwidth limitations. Their responsivity, and hence their noise equivalent power (NEP), typically degrade at frequencies exceeding the cutoff set by their characteristic thermal response time (τ_{th}), i.e., at $\omega > \tau_{\text{th}}^{-1}$. Here we show that this bandwidth limitation can be broken when a radiation sensor operates at its fundamental temperature fluctuation noise limit. The key enabler of this demonstration is a nanomechanical sensor in which frequency stability is limited by fundamental temperature fluctuations over an unprecedentedly large bandwidth of 54 Hz. In this range, the sensor performance remains within a factor 3 from its peak detectivity ($D_T^* = 7.4 \times 10^9$ cm $\cdot$ Hz$^{1/2}$W^{-1}) even though the thermal cutoff frequency is 30 times lower (i.e., $1/2\pi\tau_{\text{th}} = 1.8$ Hz). We also derive and validate experimentally,

closed-form expression predicting maximum bandwidth enhancement in the context of nanomechanical resonators interfaced with a closed-loop frequency tracking scheme.

4.2.4 Introduction

Temperature-sensitive nanomechanical resonators (NMRs) [24, 26–30, 32, 138] have attracted significant interest as an alternative to traditional thermal sensing approaches that rely on electrical sensing (e.g., resistive bolometers [108, 109], pyroelectric detectors [27–29], and thermopiles [70, 71]). In principle, mechanical-based temperature detection in NMRs can provide immunity to electrical noise (e.g., Johnson–Nyquist noise) that limits performance in traditional thermal-based detectors. This immunity creates a path to reaching the fundamental detectivity limit of thermal photon fluctuation at room temperature $D^*_{T,photon} \approx 10^{10}$ cm $\cdot$ Hz$^{1/2}$W^{-1} [163].

Reaching this fundamental detectivity limit with NMR-based radiation sensors requires eliminating all non-fundamental sources of frequency fluctuations. In recent years, these non-fundamental fluctuations have been shown to originate in large part from thermomechanical resonator fluctuations, and from noise in the readout used to capture resonator vibration. Comprehensive studies of these noise sources can be found in [38–40,48], which also outlines the central importance of including the frequency tracking schemes—such as phase-locked loop (PLL) or self-sustaining oscillators—when predicting frequency noise.

Despite these recent progress in noise modeling, demonstration of NMRs in which these noise sources are minimized below fundamental temperature fluctuation remain scarce. Previous work [136] explored the modeling of temperature fluctuation noise in a PLL frequency tracking scheme with preliminary experimental validation within a limited frequency range. Other recent comparative analysis of silicon nitride nanomechanical resonators have approached the temperature fluctuation noise limit [164] but without reaching it clearly over a broad frequency bandwidth.

Here, we demonstrate NMRs with a frequency stability dominated by temperature fluctuation noise over an unprecedentedly large bandwidth of 54 Hz. We also provide updated modeling for temperature fluctuation noise within closed-loop frequency tracking scheme, thus greatly improving predictability of noise figure in this regime.

Building on this result, we unveil an important benefit of reaching the fundamental temperature fluctuation noise limit over such a large bandwidth. In this regime, we show that detectivity and noise equivalent power remain undegraded at frequencies greatly exceeding the resonator thermal responsivity cutoff (i.e., at $\omega > 1/\tau_{th}$, where τ_{th} is the sensor characteristic thermal response time).

4.2.5 Theory

When using NMRs to perform thermal radiation sensing, noise equivalent power (NEP) in $\mathrm{W} \cdot \mathrm{Hz}^{-1/2}$ can be defined as:

$$\mathrm{NEP} = \frac{\sqrt{S_y}}{R}, \tag{4.11}$$

where S_y quantifies unwanted resonator frequency fluctuations, and R quantifies the sensor responsivity, i.e., its sensitivity to absorbed radiation. We use unitless fractional frequency ($y = \delta\omega/\omega_r$) throughout this work such that S_y is a noise spectral density (one-sided) expressed in units of Hz^{-1}. Similarly, R is in units of W^{-1} and is given by

$$R(\omega) = \frac{\gamma\alpha}{G}|H_{th}(\omega)|, \tag{4.12}$$

where G is the total thermal conductance between the NMR and its environment, in W/K, γ is the optical absorption coefficient at target detection wavelength, and α represents the temperature coefficient of fractional frequency shift, in K^{-1}. This coefficient α is mostly dictated by the NMR' s material properties and is discussed below (see Eq. 4.27) for the specific resonator used in this work. $H_{th}(\omega)$ accounts for NMR thermal

response time τ_{th} under uniform illumination, and is defined as:

$$H_{th}(\omega) = \frac{1}{1 + j\omega\tau_{th}}. \tag{4.13}$$

For the general case of an arbitrary white noise S_y, we see from Eq. 4.11 that NEP degrades rapidly at frequencies exceeding the resonator thermal response time (i.e., for $\omega > \tau_{th}^{-1}$) because of its inverse dependence on the thermal responsivity filter (Eq. 4.13). However, this is not always true if we examine more closely the different possible contributions to S_y.

Here, we consider the three most common noise sources for the overall noise profile of NMRs, namely thermomechanical noise $S_{y,tmech}$, instrument readout noise $S_{y,read}$, and fundamental temperature fluctuation noise $S_{y,T}$:

$$S_y = S_{y,tmech} + S_{y,read} + S_{y,T}. \tag{4.14}$$

Among these three noise sources, S_T is the universal limiting noise for thermal-based radiation sensors of all types [163] (e.g., bolometer, thermopile, pyroelectric detector), including NMRs. For NMRs, $S_{y,T}$ can be expressed as:

$$S_{y,T}(\omega) = \frac{4k_B T^2 \alpha^2}{G} \left| H_{th,eff}(\omega) \right|^2, \tag{4.15}$$

where k_B is the Boltzmann constant and T is the surrounding temperature. $H_{th,eff}(\omega)$ denotes the effective thermal response of the resonator, averaging all local thermal energy fluctuations over the sensor volume. As shown in [164], the value of $H_{th,eff}(\omega)$ is close to $H_{th}(\omega)$, especially when the resonator is coupled to its environment primarily by radiation. We therefore assume $H_{th,eff}(\omega) \approx H_{th}(\omega)$ in the following.

In an ideal case where all non-fundamental noise sources (i.e., $S_{y,tmech} + S_{y,read}$) are minimized compared to the fundamental temperature fluctuation noise $S_{y,T}$ (i.e., $S_y \approx$

$S_{y,T}$), NEP reduces to

$$\mathrm{NEP_T} = \frac{\sqrt{4k_B T^2 G}}{\gamma}. \tag{4.16}$$

Furthermore, Eq. 4.16 can be normalized by the sensor area to provide the maximum possible sensor detectivity ($D^* = A^{1/2}/\mathrm{NEP}$, where A is the sensor area):

$$D_T^* = \gamma \sqrt{\frac{A}{4k_B T^2 G}}. \tag{4.17}$$

Another limiting case occurs when the sensor is thermally coupled to its surroundings primarily by radiation on both its faces: $G \approx 2 \cdot 4\sigma_{SB}\varepsilon A T^3$, where σ_{SB} is the Stefan–Boltzmann constant, ε is the total hemispherical emissivity, and a perfect emitter/absorber is assumed ($\varepsilon = \gamma = 1$). In this case, D^* converges to the well-known fundamental limit of thermal photon fluctuation ($D^*_{T,photon} = 1.3 \times 10^{10}$ cm $\cdot$ Hz$^{1/2}$W^{-1} for a two-side coupled sensor).

Of central importance, we see in Eq. 4.16–4.17 that a thermal sensor limited purely by temperature fluctuation noise $S_{y,T}$ is unaffected by the thermal filter $H_{th}(\omega)$ and can therefore, in principle, have infinitely large sensing bandwidth. More specifically, a sensor can be expected to operate at its fundamental NEP and D^* performance limits (Eq. 4.16–4.17) at any frequency where its overall noise $S_y(\omega)$ is limited by fundamental temperature fluctuations $S_{y,T}(\omega)$. In this case, the sensor bandwidth is not defined anymore by the thermal corner frequency $\omega_{th} = \tau_{th}^{-1}$, but instead by the limit frequencies ($\omega_{c,read}$ and $\omega_{c,tmech}$) above which other non-fundamental noise sources (respectively $S_{y,read}$ and $S_{y,tmech}$) begin to dominate over $S_{y,T}$.

To quantify the range of frequencies over which fundamental-level performances are possible, we aim to provide expressions for critical intersection frequencies (ω_c) above which either $S_{y,tmech}$ or $S_{y,read}$ start dominating over $S_{y,T}$. To do so, we must however consider not only the intrinsic noise contributions to S_y, but their values after filtering by the frequency tracking apparatus; an optical fiber interferometer combined with a

phase-locked loop (PLL) in the present study (see Fig. 4.6a). In this setup, an optical fiber tip is positioned in close proximity to the surface of the NMR, creating a low finesse interferometer between the tip of the optical fiber and the NMR. The reflected light signal is collected by a photodetector and subsequently processed by a lock-in amplifier with built-in PLL frequency tracking.

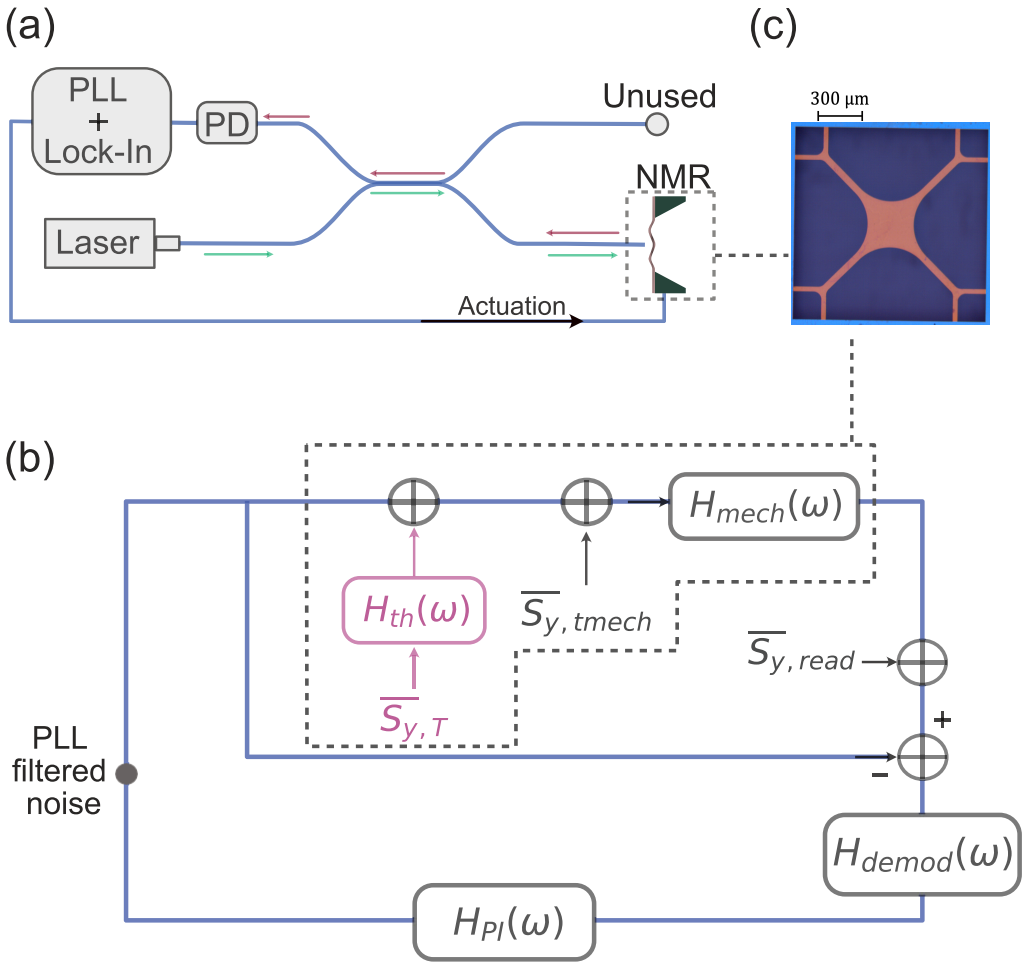

Figure 4.6: **Frequency tracking setup schematics.** (a) Schematic of a frequency tracking apparatus for nanomechanical resonators (NMRs), showing a high-level representation of an optical interferometer and a lock-in amplifier equipped with a phase-locked loop (PLL) function. (b) Block diagram illustrating the signal chain for the filtering process of various fractional frequency noise spectral densities (in units of $\mathrm{Hz}^{-1/2}$). Here, the noise inputs are unfiltered temperature fluctuation noise $\overline{S_{y,T}}$, thermomechanical noise $\overline{S_{y,tmech}}$, and instrument readout noise $\overline{S_{y,read}}$. The overline donation denotes the white noise magnitude before filtering, i.e., $\overline{S_y} = S_y(0)$. (c) Image of the NMR used in this work.

The block diagram in Fig. 4.6(b) outlines the noise filtering process when using a PLL to track the resonance frequency. This block diagram configuration is largely inspired from Demir *et al.* [39], with the addition of temperature fluctuation noise $S_{y,T}$. Under the PLL frequency tracking scheme, the filtered thermomechanical noise can be expressed as

$$S_{y,tmech}^{PLL}(\omega) = \frac{2k_BT}{m_{eff}\omega_r^3 Q A_{rss}^2} \left|H_{mech}^{PLL}(\omega)\right|^2, \tag{4.18}$$

where Q is the mechanical quality factor, ω_r is the resonance frequency at a given eigenmode (in rad/s), m_{eff} is the effective mass, A_{rss} is the resonator driven vibration amplitude (in m), and $H_{mech}^{PLL}(\omega)$ accounts for the PLL filtering effect on thermomechanical noise, as given in [39, 120]:

$$H_{mech}^{PLL}(\omega) = \frac{(j\omega K_p + K_i)H_{demod}(\omega)}{(j\omega)^2 + \frac{j\omega}{\tau_{mech}} + (j\omega K_p + K_i)H_{demod}(\omega)}, \tag{4.19}$$

where K_i and K_p are the corresponding control loop parameters of the PI controller used in the PLL, $\tau_{mech} = 2Q/\omega_r$ is the mechanical time constant of the NMR, and $H_{demod}(\omega)$ is the lock-in amplifier demodulation filter. The filtered instrument readout noise $S_{y,read}$ is given by [6]:

$$S_{y,read}^{PLL}(\omega) = \frac{S_x}{2Q^2A_{rss}^2} \left|\frac{H_{mech}^{PLL}(\omega)}{H_{mech}(\omega)}\right|^2, \tag{4.20}$$

where S_x is the displacement noise floor of the readout instrument in m^2/Hz, and $H_{mech}(\omega) = (1 + j\omega\tau_{mech})^{-1}$ is the intrinsic mechanical filter of the resonator.

We model the fundamental temperature fluctuation $S_{y,T}$ as an external noise whereas the intrinsic thermal filter $H_{th}(\omega)$ of the NMR is outside of the signal loop, as in the block diagram in Fig. 4.6(b). This is analogous to a step frequency change in the resonator described in [48] and is therefore included in the loop in the same way. In this

configuration, the filtered $S_{y,T}$ becomes:

$$S_{y,T}^{PLL}(\omega) = \frac{4k_B T^2 \alpha^2}{G} \left| H_{mech}^{PLL}(\omega) \cdot H_{th}(\omega) \right|^2 . \tag{4.21}$$

Conversely, frequency changes resulting from radiation impinging the resonator follow the same signal chain, such that the intrinsic sensor responsivity R is filtered by the PLL, resulting in:

$$R^{PLL}(\omega) = \frac{\gamma \alpha}{G} \left| H_{mech}^{PLL}(\omega) \cdot H_{th}(\omega) \right| . \tag{4.22}$$

Note that Eq. 4.21–4.22 corrects our previous model for temperature fluctuation noise in [136]. The conclusions of [136] remain unchanged, but the model proposed herein greatly improves predictability over a broad range of PLL parameters.

We find the limit frequencies ($\omega_{c,read}$ and $\omega_{c,tmech}$) by solving for the intersection between $S_{y,T}^{PLL}$ and, respectively, $S_{y,read}^{PLL}$ or $S_{y,tmech}^{PLL}$, as illustrated in Fig. 4.7. The critical frequency above which thermomechanical noise exceeds temperature fluctuation noise is well approximated by:

$$\omega_{c,tmech} \simeq \sqrt{\frac{2T\alpha^2 m_{eff} \omega_r^3 Q A_{rss}^2}{G}} \cdot \omega_{th}, \tag{4.23}$$

when the term under the square root is greater than 1. Here, $\omega_{th} = \tau_{th}^{-1}$ is the thermal cut-off frequency of the NMR. Likewise, the frequency above which readout noise exceeds temperature fluctuation noise is approximated as:

$$\omega_{c,read} \simeq \left(\frac{2k_B T^2 \omega_r^2 \alpha^2 A_{rss}^2}{S_x G} \right)^{1/4} \cdot \sqrt{\omega_{th}}. \tag{4.24}$$

Again, assuming the term under the fourth root is greater than 1.

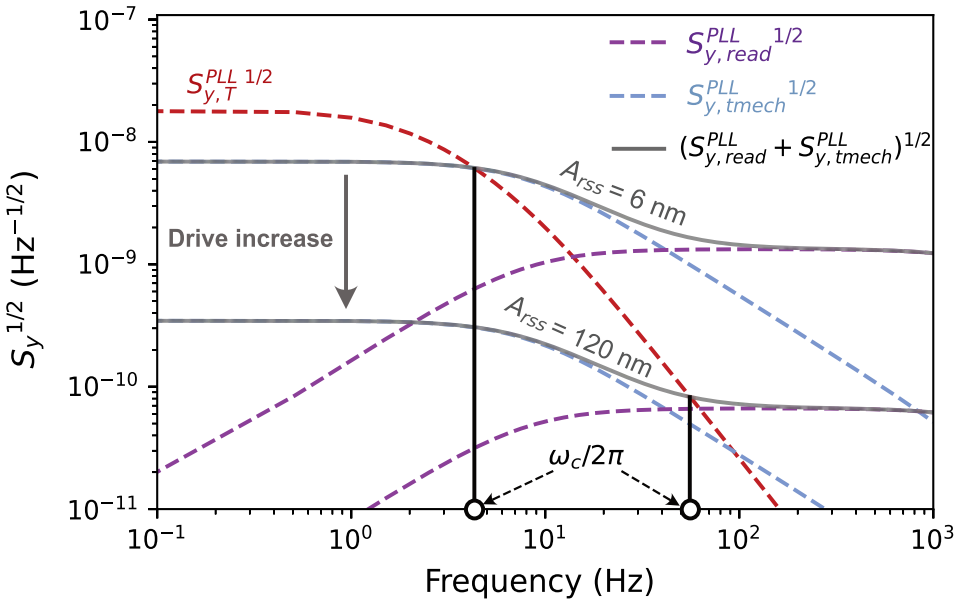

Figure 4.7: **Critical intersection frequency.** Example theoretical frequency fluctuation S_y outlining the critical intersection frequency ω_c for low and high drive amplitude A_{rss}. Resonator parameters are the same as presented in the results section, with a phase-locked loop PLL frequency tracking set at 8 Hz bandwidth, with at demodulation BW set at 5 kHz.

Interestingly, the analytical expressions for $\omega_{c,tmech}$ and $\omega_{c,read}$ indicate that the limit frequencies are independent of the PLL frequency tracking parameters, but rather on parameters intrinsic to the NMR itself (i.e., α, m_{eff}, Q, A_{rss}, ω_r, G) and the instrument readout noise (S_x). In other words, there is no fundamental benefit to adjusting the demodulation bandwidth or PLL control parameter settings to achieve better thermal sensing performance.

Finally, by solving for the intersection between $S_{y,T}^{PLL}$ and $S_{y,read}^{PLL} + S_{y,tmech}^{PLL}$, one can obtain the overall limit frequency ω_c above which all combined non-fundamental noises exceed the fundamental temperature fluctuation. This is not straightforward analytically, and we instead provide a phenomenological approximation using the analytically obtained $\omega_{c,tmech}$ and $\omega_{c,read}$:

$$\omega_c^{-N} \approx \omega_{c,read}^{-N} + \omega_{c,tmech}^{-N}, \tag{4.25}$$

which yields good results in the current work for $N \approx 3$, as illustrated in Fig. 4.7.

It is worth noting that the overall intersection frequency ω_c (Eq. 4.25) can transition from being dominated by either $\omega_{c,read}$ or $\omega_{c,tmech}$, as we vary the drive amplitude. Even though $S^{PLL}_{y,tmech}$ and $S^{PLL}_{y,read}$ both scale with A^{-2}_{rss} (see Eq. 4.18 and 4.20), the intersection equations (Eq. 4.23–4.24) do not, due to the different $H(\omega)$ filters. As shown in Fig. 4.7, for the typical resonator parameters and readout noise used in this work, increasing A_{rss} causes the limit frequency ω_c to shift from being limited by thermomechanical noise (e.g., for $A_{rss} = 6$ nm) to being limited by readout noise (for $A_{rss} = 120$ nm).

Obviously, driving NMR beyond its mechanical linearity would eventually introduce unwanted frequency fluctuation, originating from Duffing nonlinearity. In this work, we consider the amplitude limit given by Manzaneque *et al.* [143]:

$$A_{crit} = \frac{2}{\sqrt[4]{3}}\sqrt{\frac{F_s}{\omega_r \beta}}, \tag{4.26}$$

where β is the Duffing coefficient (in m^{-2}) and F_s is the sampling frequency of the frequency fluctuations signal. Here, Eq. 4.26 accounts for the fast-sensing regime in which the intended sampling frequency is much higher than the mechanical cut-off frequency of the NMR (i.e., $\omega > \tau^{-1}_{mech}$). Note that Eq. 4.26 predicts considerably higher A_{crit} than the more commonly accepted limit [6] (i.e., $A_{crit} = 0.56L(\sigma/QE)^{-1/2}$, where L is the size of the NMR, σ is the tensile stress and E is the Young' s modulus). For example, setting $F_s \approx 50$ Hz and considering our typical resonator parameters (next section), we obtain $A_{crit} \approx 102$ nm using Eq. 4.26.

4.2.6 Methods & Results

In this work, we use a low-stress (70 MPa), 90-nm-thick silicon nitride (SiN) NMR (see Fig. 4.6c) that has a surface area $A \approx 4.2 \times 10^{-7}$ m^2. The structure is fabricated via laser ablation [165, 166] of a plain square SiN membrane. Detailed fabrication process and characterization of multiple mechanical eigenmodes are subject of a separate article

in preparation. We mount this NMR on a steel plate using three pairs of disk magnets and mechanically excite it with a piezoelectric actuator. All components are placed in a custom-built vacuum chamber operating at pressure $\sim 1 \times 10^{-6}$ Torr to sufficiently suppress air damping, therefore maximizing the NMR Q-factor. We measure NMR displacement using a custom-assembled optical fiber interferometer with the configuration shown in Fig. 4.6(a). It consists of a 1564 nm Orion™ distributed feedback (DFB) laser, a 90:10 coupler, a 5 dB optical attenuator, an optical isolator, and a Thorlabs PDA20CS2 photodetector. A Zurich Instrument Ltd. MFLI is used for both exciting and tracking the NMR resonance frequency.

We first perform a set of measurements on some of the NMR fundamental thermal and mechanical properties. We pick a low-order mechanical mode at 60.2 kHz that has both a high Q-factor (2.4×10^6, see Fig. 4.8a) and that shows a strong fluctuation response, i.e., that is well aligned with the tip of our optical fiber readout (see Fig. 4.8c). Using finite element simulation (see Appendix. B.2), we find the effective mass m_{eff} for this particular mode is roughly a third of the actual NMR mass m_0 (i.e., $m_{eff} = m_0/2.9$, where $m_0 = hA\rho$, h is the NMR' s thickness and ρ is SiN material density). Using this mode, we vary the actuation amplitude to measure the Duffing nonlinearity. By fitting the frequency–amplitude data shown in Fig. 4.8(b), we extract an experimental Duffing coefficient of $\beta = 3.2 \times 10^{10}$ m^{-2}.

We also measure the instrument displacement noise floor ($S_x^{1/2} = 0.04$ pm$\cdot$Hz$^{-1/2}$) as pictured in Fig. 4.8(c). This calibration is done in a separate experiment by moving the optical fiber tip towards the membrane by a known distance to calibrate the interferometer sensitivity (in V/m), allowing transformation of raw voltage noise to displacement noise. We measure the NMR thermal response time (τ_{th}) by intermittently exposing the NMR to a broadband IR source modulated using an optical chopper at 4 Hz and 10% duty cycle. From the fitted transient response (Fig. 4.8d), we measure $\tau_{th} = 90$ ms. In this measurement, we set the PLL bandwidth to 40 Hz, which is significantly higher than

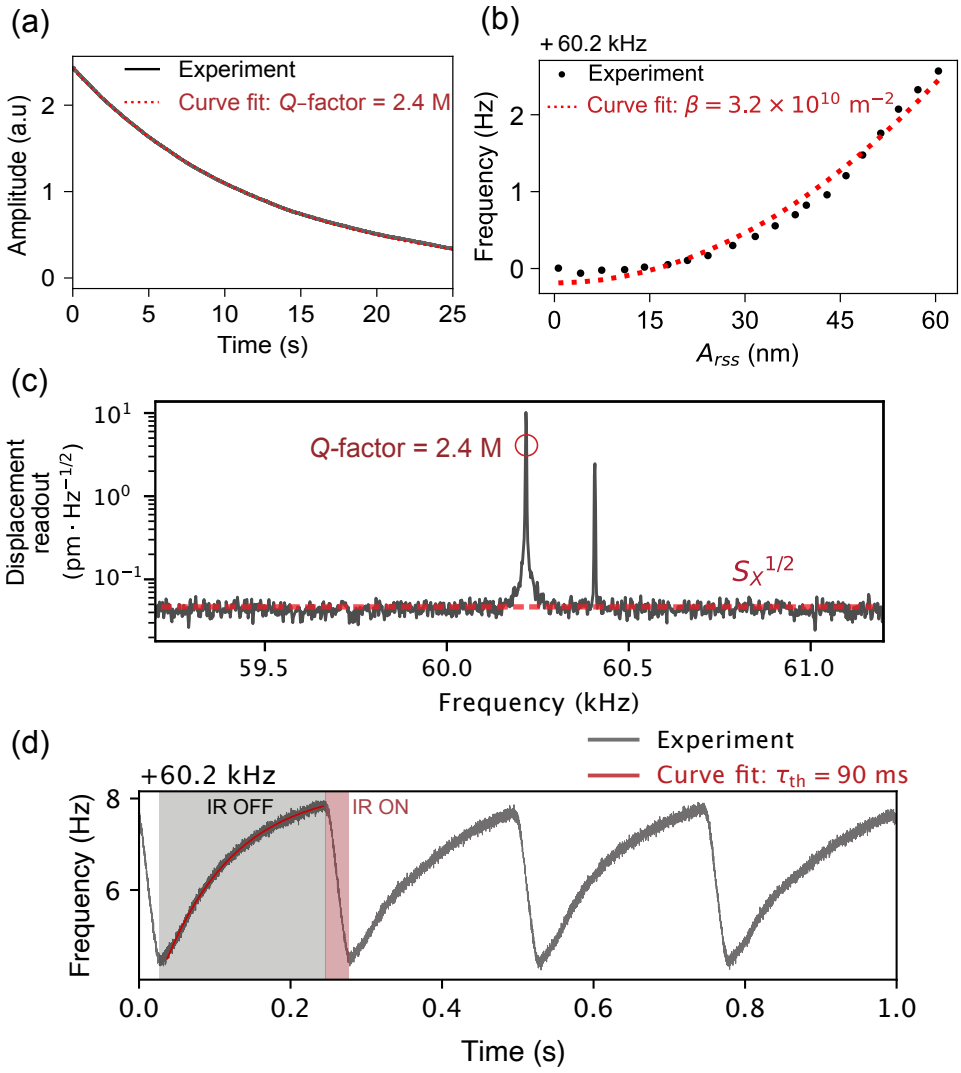

Figure 4.8: **General characterization of the resonator mechanical and thermal response.** (a) Amplitude-time trace of a mechanical ringdown for extracting NMR' s mechanical Q-factor. (b) Frequency-amplitude plot used for determining the Duffing nonlinearity coefficient of the NMR. (c) Snapshot of the readout instrument displacement noise floor $S_x^{1/2}$, with thermally excited mechanical modes. (d) NMR' s thermal time constant τ_{th} measurement by intermittently exposing the NMR to broadband IR source modulated using an optical chopper at 4 Hz and 10% duty cycle.

the thermal cut-off frequency, $\omega_{th}/2\pi = 1.8$ Hz.

The total thermal conductance G between the NMR and its environment, as well as the temperature coefficient of fractional frequency shift α are evaluated by a combination of analytical models and finite-element analysis. We calculate radiative contribution to the thermal conductance using Stefan-Boltzmann law $G_{rad} = 2 \cdot 4\sigma_{SB}\varepsilon AT^3 = 4.8\times10^{-7}$ W/K, considering a total emissivity $\varepsilon = 0.1$ [50]. The factor of 2 accounts for radiative thermal exchange on both front and back NMR surface. Using finite element simulation (see Appendix. B.1) and considering a thermal conductivity of 2.7 W m^{-1}K^{-1} [5] for SiN, we find that $x_{rad} = 65\%$ of the total thermal exchanges with the surrounding environment occurs through radiation (i.e., 35% via solid-state conduction). The total thermal conductance is then given by $G = G_{rad}/x_{rad} = 7.4 \times 10^{-7}$ W/K. Again, using finite element simulation (see Appendix. B.2), we obtain a temperature coefficient of fractional frequency shift $\alpha = 6.5 \times 10^{-3}$ K^{-1}. Noteworthy, this value is very close (within 1%) from the value calculated using the analytical expression derived for drum resonators [50]:

$$\alpha \simeq \frac{E\alpha_T}{2\sigma(1-\nu)}, \tag{4.27}$$

where $E = 300$ GPa is the Young's modulus, $\alpha_T = 2.2 \times 10^{-6}$ K^{-1} is the thermal expansion coefficient of SiN, $\sigma = 70$ MPa is the tensile stress and $\nu = 0.27$ is the Poisson ratio of SiN.

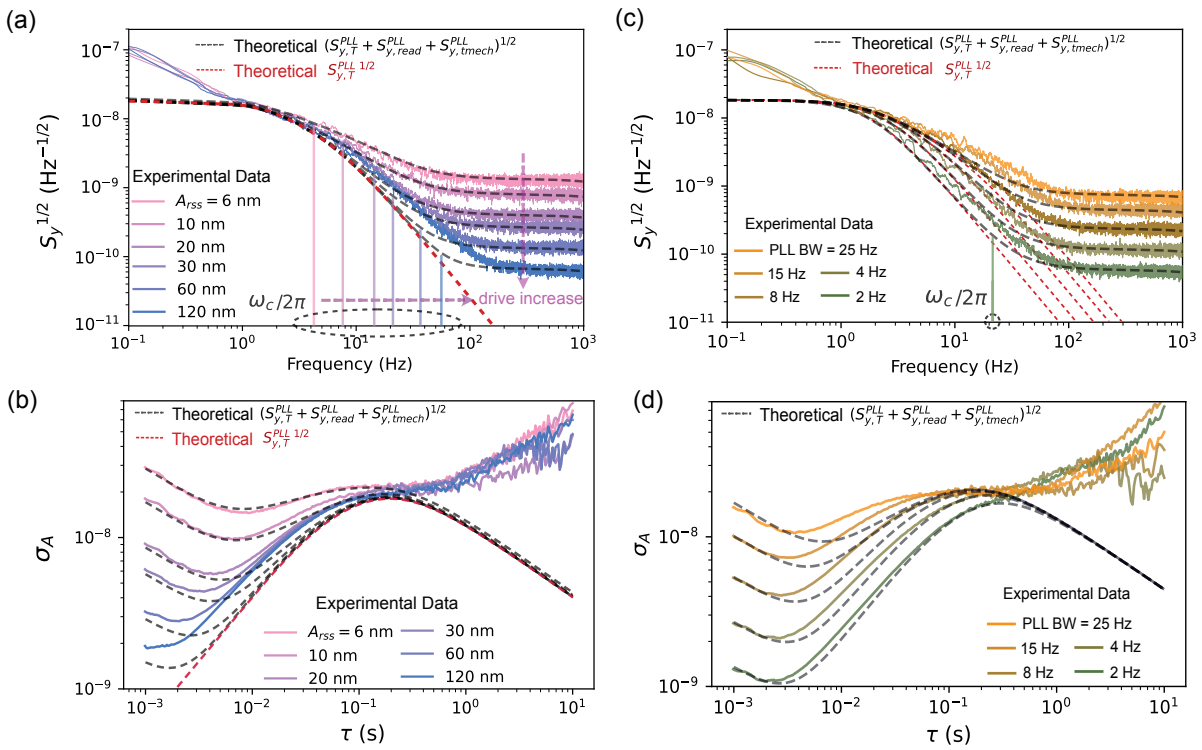

Figure 4.9: **Frequency fluctuation measurements.** (a) Comparison between the experimental fractional frequency spectral density $S_y^{1/2}$ (in colorful solid lines) and their corresponding theoretical predictions (in grey dashed lines), at various vibration amplitude A_{rss} with fixed demodulation bandwidth set to 5 kHz and a phase-locked loop PLL bandwidth of 8 Hz. Theoretical limit frequency $\omega_c/2\pi$ at each A_{rss} is given as a visual guide. (b) Allan deviation σ_A at various A_{rss} using the same data as in (a). (c) Comparison between the experimental $S_y^{1/2}$ (in colorful solid lines) and their corresponding theoretical prediction (in grey dashed lines) at varying PLL bandwidth, with fixed $A_{rss} = 30$ nm, and a demodulation bandwidth of 5 kHz. (d) Allan deviation σ_A at various A_{rss} using the same data as in (c).

When measuring fractional frequency noise of the NMR using PLL, we set the demodulation bandwidth of the lock-in amplifier to a high value (5 kHz), ensuring that noise originating from the readout instrument $S_{y,read}^{PLL}$ remains largely unfiltered. We then set data acquisition rate significantly higher than the demodulation bandwidth (53 kHz) to avoid signal aliasing. We begin by recording frequency-time traces for multiple levels of drive amplitude A_{rss}, at a fixed PLL bandwidth of 8 Hz, and thereafter convert those to noise spectral density $S_y^{1/2}$ and Allan deviation σ_A (Fig. 4.9a–b). The experimental data, in colored lines, closely match our theoretical predictions $(S_{y,tmech}^{PLL}+S_{y,read}^{PLL}+S_{y,T}^{PLL})$

in grey dashed lines, without the need for fitting parameters.

As we increase the drive amplitude (A_{rss}), traces increasingly overlap with the predicted $S_{y,T}^{PLL}$ (red dashed line in Fig. 4.9a–b), indicating that they are dominated by fundamental temperature fluctuation noise over an increasingly wide bandwidth. To make the measurement bandwidth extension effect visually clearer, in Fig. 4.9(a), we include the theoretical overall limit frequency ω_c for each trace, indicating the point where the noise profile is predicted to transition from the fundamental temperature fluctuation dominated regime to non-fundamental noise dominated regime. In specific, we see that at maximum $A_{rss} = 120$ nm, the NMR can operate at the $S_{y,T}^{PLL}$ dominated regime up to slightly above 54 Hz—roughly two orders of magnitude greater than the NMR' s intrinsic thermal cutoff frequency $\omega_{th}/2\pi = 1.8$ Hz. In contrast, this measurement bandwidth enhancement is not seen in Fig. 4.9(c–d) where we solely vary the PLL bandwidth while using a fixed A_{rss} of 30 nm. This aligns with our theoretical prediction, as Eq. 4.23–4.24 are independent of the PLL bandwidth.

In the noise traces of Fig. 4.9, we observe some discrepancy between the experiment and the theoretical prediction. At low sampling frequency $\omega \leq \omega_{th}$, we observe the typically unavoidable additional noise due to systematic drift. At higher sampling frequencies ($\omega > \omega_{th}$), we also observe some discrepancy between the theoretical and experimental roll-off in $S_{y,T}^{PLL}$. This is especially visible for higher A_{rss} traces. We hypothesize that this discrepancy arises from our assumption of $H_{th,eff}(\omega) \approx H_{th}(\omega)$ in our theoretical calculation. As hinted in [164], averaging local energy fluctuations into an effective $H_{th,eff}(\omega)$ thermal filter may result in a greater noise bandwidth than the thermal response measured under uniform heating (i.e., $H_{th,eff}(\omega) > H_{th}(\omega)$). This phenomenon warrants quantitative experimental investigation in future work.

Readout laser back-action [40, 164] and Duffing nonlinearity [143] are also known to cause unwanted frequency fluctuations, but those are unlikely in the present case. We verify that laser power fluctuation plays a negligible role in this experiment by repeating

measurements with a variable optical attenuator (see Appendix. B.3). We also observe that the frequency fluctuation originating from Duffing nonlinearity is negligible. We note in Fig. 4.9(a) that higher A_{rss} never increases noise. High A_{rss} either reduces noise at very high frequencies (where additive noise dominate) or has no effect on the noise (at frequencies where temperature fluctuations noise $S_{y,T}$ dominate). Negligible nonlinear noise is consistent with the critical amplitude predicted by Eq. 4.26. We are mostly interested in $\omega/2\pi$ with sampling frequencies F_s between 4 to 54 Hz. By using our measured β value into Eq. 4.26, we estimate A_{crit} increases from 28 to 102 nm for this range of F_s, which is generally above our experimental A_{rss}.

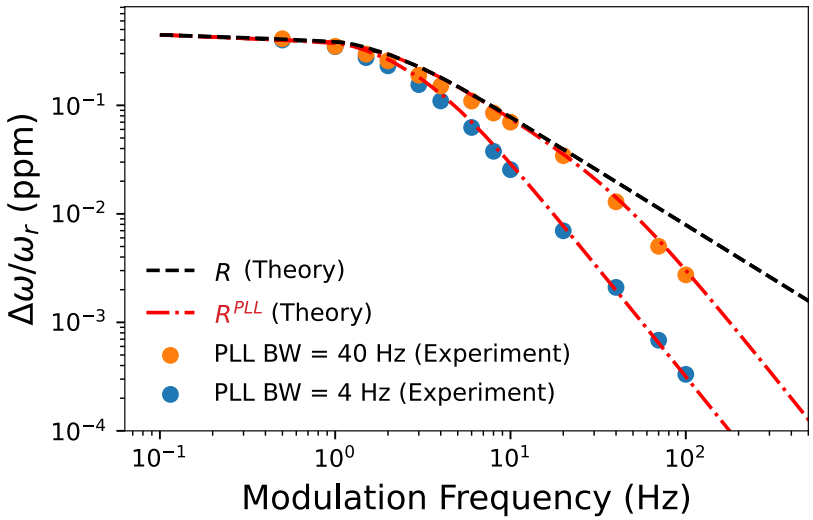

Figure 4.10: **Thermal responsivity measurement.** Circular dots represent experimental fractional frequency shift $\Delta\omega/\omega_r$ induced by impinging thermal radiation at various modulation frequencies under closed-loop frequency tracking. Blue dots represent data with phase-locked loop PLL set to 4 Hz and a demodulation bandwidth of 5 kHz. Orange dots represent with PLL set to 40 Hz and a demodulation bandwidth of 5 kHz. Red dashed lines represent theoretical prediction (Eq. 4.22) corresponding to each experimental trace. Black dashed line represents the modulated theoretical thermal responsivity curve without closed-loop frequency tracking (i.e., without PLL).

Another important aspect to confirm the validity of our model is to confirm the predicted effect of PLL filtering on the NMR' s thermal responsivity, i.e., R^{PLL}. In Fig. 4.10, we record traces of the NMR's responsivity at largely different PLL bandwidths

(4 and 40 Hz). For each trace, we modulate the thermal source from 0.5 Hz to 100 Hz. The experimental data closely matches theoretical prediction from Eq. 4.22 (red dashed lines) in both cases. In contrast, the black dashed line in Fig. 4.10 includes only the NMR' s intrinsic thermal filter $H_{th} = (1 + j\omega\tau_{th})^{-1}$ which, as expected, does not align with our measurement.

Lastly, we obtain our sensor NEP and D^* by combining our experimentally measured noise S_y (i.e., Fig. 4.9) with our experimentally validated responsivity model (Fig. 4.10). We assume $\gamma = 0.4$, which corresponds to the peak material absorption of 90-nm-thick SiN membrane at a wavelength $\lambda = 11$ μm [50]. Of course, in a practical setting, this material absorption peak would be too narrow, and a broadband optical absorber would be required. We expect this step to be straightforward since previous work by our group and others [27,138] have demonstrated that including such a radiation absorber does not degrade the sensor mechanical performances.

We present both NEP and D^* in Fig. 4.11 for various A_{rss} and PLL bandwidth. In all cases, our calculated ω_c values (using Eq. 4.25) accurately predict the corner frequency at which experimental D^* declines. For the highest A_{rss} drive, this decline occurs at 54 Hz, i.e., at a 30 times higher frequency than the sensor intrinsic thermal bandwidth ($\omega_{th}/2\pi = 1.8$ Hz). As a visual guide, in Fig. 4.11(b), we also include both theoretical D^* and theoretical overall limit frequency ω_c for each A_{rss}. We observe strong agreement between the theoretical D^* traces. The minor discrepancies are due to the same reasons as discussed in the context of Fig. 4.9.

As expected also from our theoretical model, PLL bandwidth have negligible influence on the NEP and D^*. At a fixed $A_{rss} = 40$ nm drive, we observe that varying the PLL bandwidth from 2 to 25 Hz leads to no difference in sensing performance as the three traces completely overlap. PLL filtering affects both the responsivity and the noise in the same manner and therefore cancels out in the final NEP and D^*.

In conclusion, we have demonstrated an NMR radiation sensor limited by temper-

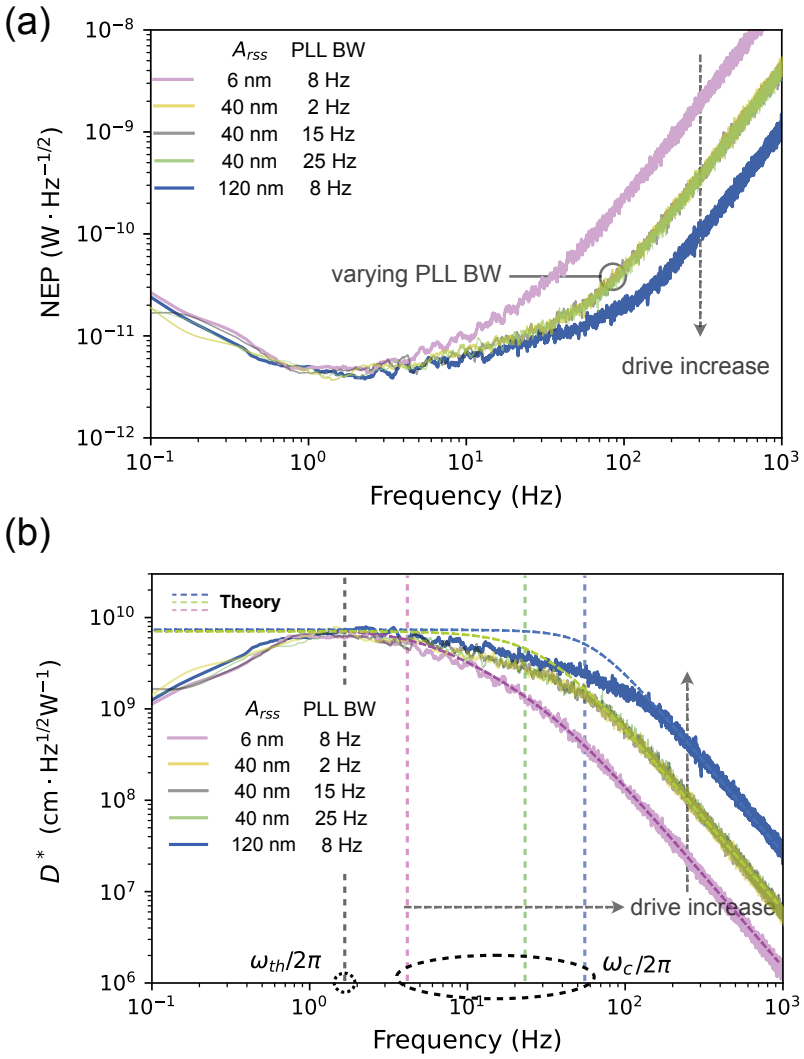

Figure 4.11: **Enhanced NEP and D^* bandwidth.** Experimental noise equivalent power NEP (a) and detectivity (b) of the nanomechanical resonator at various vibration amplitudes A_{rss} and phase-locked loop PLL bandwidths. As predicted, the critical frequency (ω_c) at which sensor performance decline significantly is greater than the thermal cutoff frequency (ω_{th}), by up to a factor 30. The curves also confirm that ω_c depends strongly on the drive amplitude (A_{rss}), but not on the frequency tracking PLL bandwidth (the curves at different PLL completely overlap and appear green). Experimental specific detectivity D^* traces are obtained from the NEP values in (a) using $\sqrt{A}$/NEP, where $\sqrt{A} = 300$ μm is the characteristic size of the center pad of the NMR. Theoretical predictions for D^* are shown in dashed lines with matching colors. These predictions assume $\gamma = 0.4$ as the absorption, which corresponds to the material absorption of 100 nm thick SiN at $\lambda = 11$ μm wavelength.

ature fluctuation noise over an unprecedented measurement bandwidth (i.e., $30 \times \omega_{th}$). This demonstration opens avenues for developing fast NMR-based thermal sensors operating at the fundamental detectivity D^* limit at room temperature, which could serve as next-generation long-wavelength infrared (LWIR) thermal sensors. An obvious next step for this work is to demonstrate the same signal bandwidth enhancement in a sensor comprising a broadband optical absorber, rather than relying solely on the intrinsic material absorption of SiN. This should be straightforward since previous work has demonstrated that including such a radiation absorber does not degrade the sensor mechanical performances.

5. Terahertz sensing

5.1 Article 3: Terahertz sensing

5.1.1 Foreword

The last chapter of this thesis presents a published journal article ***APL Photonics 9, 126105 (2024) [138]*** titled as **High detectivity terahertz radiation sensing using frequency-noise-optimized nanomechanical resonators**. This paper experimentally demonstrates incoherent terahertz (THz) detection at room temperature using a membrane nanomechanical resonator functionalized with a THz absorber. As a result, it outperforms the state-of-the-art commercial pyroelectric THz detector [91] by more than an order of magnitude in specific detectivity D^* at ~ 2 THz. Nevertheless, the non-ideality of our portable vacuum chamber setup prevents our SiN membrane resonator from reaching a temperature fluctuation dominated noise profile in this experiment. To date, this work achieves the highest detectivity ever reported by a nanomechanical resonator operating at THz wavelengths (0.5 to 3 THz). Note that *thermal fluctuation noise* in this article refers to the same concept as temperature fluctuation noise; it is simply a different name.

Author list: Chang Zhang, Eeswar K. Yalavarthi, Mathieu Giroux, Wei Cui, Michel Stephan, Ali Maleki, Arnaud Weck, Jean-Michel Ménard and Raphael St-Gelais.

5.1.2 Author Contributions

Chang Zhang: Lead investigator; responsible for all experimental work and drafting the manuscript.

Eeswar K. Yalavarthi: Assistant investigator; helped build the THz emission setup and provided support during the experiments.

Mathieu Giroux: Assistant investigator; helped verify and sanity-check the mathematical equations in the article.

Wei Cui: Assistant investigator; helped build the THz emission setup.

Michel Stephan: Assistant investigator; helped build the portable vacuum chamber.

Ali Maleki: Assistant investigator; provided support for designing the THz metasurface absorber.

Arnaud Weck: Assistant investigator; provided support for depositing the THz metasurface absorber.

Jean-Michel Ménard: Assistant principal investigator; provided detailed feedback and contributed to the conceptualization of the project.

Raphael St-Gelais: Principal investigator; led the conceptual development of the article, provided guidance during the experiments, and assisted in writing the manuscript.

5.1.3 Abstract

We achieve high detectivity terahertz radiation sensing using a silicon nitride nanomechanical resonator functionalized with a metasurface absorber. High performances are achieved by striking a balance between the frequency stability of the resonator, and its responsivity to absorbed radiation. Using this approach, we demonstrate a detectivity $D^* \approx 3.4 \times 10^9$ cm $\cdot \sqrt{\text{Hz}}/\text{W}$ and a noise equivalent power NEP ≈ 36 pW$/\sqrt{\text{Hz}}$ that outperform the best room-temperature on-chip THz detectors, such as pyroelectric detectors, while maintaining a comparable thermal response time of ≈ 200 ms. Our optical

absorber consists of a 1-mm diameter metasurface, which currently enables a 0.5–3 THz detection range but can easily be scaled to other frequencies in the THz and infrared ranges. In addition to demonstrating high-performance terahertz radiation sensing, our work unveils an important fundamental trade-off between frequency stability and responsivity in thermal-based nanomechanical radiation sensors.

5.1.4 Introduction

Although thermal-based sensors have been used for decades for incoherent long-wavelength (infrared and terahertz) detection, their performance still falls significantly short of the fundamental detectivity limit imposed by the photon fluctuation noise of a blackbody [163] ($D^* = 1.8 \times 10^{10}$ cm $\cdot \sqrt{\text{Hz}}/\text{W}$). This performance gap largely results from non-fundamental imperfections, such as Johnson-Nyquist electrical noise, occurring in existing thermal-based sensing elements. In recent years, temperature-sensitive nanomechanical resonators have been proposed as a promising alternative. Measuring temperature changes with a mechanical resonance can in-principle be made immune from electrical noise, using for example an optical-based de-coupled readout. Resonators made of thin-film materials e.g., silicon nitride (SiN) [167–171], aluminum nitride (AlN) [172], graphene [173], gallium arsenide (GaAs) [174] have been investigated extensively for thermal-based radiation sensing at infrared wavelengths. Using a similar thermal-based sensing approach, resonators coated with additional metal absorbers have been proposed for detection at THz [175] (0.25–3 THz) and sub-THz [176] (0.1–0.3 THz) frequencies.

A common approach for optimizing performances in these nanomechanical sensors is by maximizing the magnitude of the mechanical resonance frequency shift relative to optical power absorption (i.e., maximizing thermal responsivity R). This is typically done by utilizing resonators of very small effective mass (i.e., effective length of the sensing area from 10^1 μm to 10^2 μm [167–169,173]) and by thermally isolating them via extremely thin supporting structures (e.g., tether [171, 173, 176], rod [167, 169], etc). Surprisingly,

resonators frequency stability is typically not as central to the design process as responsivity R, even though it is equally important to the determination of the final noise figure. Considering recent studies on frequency noise in nanomechanical resonators [177–181], we find that approaches for improving the responsivity R, such as mass miniaturization and thermal isolation enhancement, can also significantly degrade resonators frequency stability and hence the overall sensing performance. As a result, the specific detectivity D^* of recently reported resonator-based THz [175] and sub-THz [176] detectors still falls short of the best commercial room-temperature, on-chip THz detectors (i.e., pyroelectric detectors [182, 183] with $D^* \approx 7 \times 10^8$ cm $\cdot \sqrt{\text{Hz}}/\text{W}$) by factors 68 and 2, respectively. Likewise, their performances are at least one order of magnitude below those of Golay cells [184] ($D^* \approx 4 \times 10^9$ cm $\cdot \sqrt{\text{Hz}}/\text{W}$).

Here, we show that maximizing responsivity by miniaturization can be a counterproductive sensor design approach, and that greater detection performance gains can be realized by improving frequency stability using a resonator of relatively large mass. By striking a balance between responsivity and frequency stability, we experimentally demonstrate an uncooled THz detector with NEP ≈ 36 pW$/\sqrt{\text{Hz}}$ and specific detectivity $D^* \approx 3.4 \times 10^9$ cm $\cdot \sqrt{\text{Hz}}/\text{W}$ at 2 THz incident radiation frequency. Our approach therefore exhibits two orders of magnitude improvement in D^* compared with resonator-based detectors operating in THz frequency range [175] and a factor of 5 improvement in D^* compared with the highest performance commercial room-temperature, on-chip THz detectors [182, 183].

5.1.5 Theory

Before diving into the specifics of our nanomechanical THz detector, we outline important parameters of a square SiN membrane resonator for thermal-based detection of radiation (i.e., at any incident wavelength). For simplicity, this theoretical investigation assumes uniform absorption of incident radiation across the entire membrane area. Ad-

justments for a localized absorber are later discussed in Methods & Results Section. We first define noise equivalent power (in $\mathrm{W}/\sqrt{\mathrm{Hz}}$) as:

$$\mathrm{NEP} = \frac{\sqrt{S_y}}{R}, \tag{5.1}$$

where R is the sensor responsivity of the fractional frequency shift to incident radiation (in W^{-1}), S_y is the resonator fractional frequency noise spectral density (in Hz^{-1}) for a given eigenmode of frequency f_r. We express all noise spectral densities and filters in Hz rather than in rad/s, as detailed in Appendix. C.1. This allows for better uniformity with noises in conventional electronic instrumentation (e.g., photodetectors and bolometers) which are more commonly expressed in this unit base.

The frequency noises S_y of a typical nanomechanical resonator can be categorized into intrinsic noises and extrinsic detection noise (i.e., due to non-ideality in readout methods). For this theoretical analysis, we investigate a temperature-sensitive, high-Q factor resonator without detection noise. The total noise profile ($S_y = S_{y,TF} + S_{y,TM}$) therefore comprises thermomechanical $S_{y,TM}$ and thermal fluctuation $S_{y,TF}$ noises (i.e., with intrinsic noises only). Thermomechanical noise (in Hz^{-1}) is given by [185]:

$$S_{y,TM}(f) = \frac{k_B T}{4\pi^3 m_{eff} f_r^3 Q A_{rss}^2} \left| H_{mech}(f) \right|^2, \tag{5.2}$$

where k_B is the Boltzmann constant, T is the background environment temperature, m_{eff} is the resonator effective mass, A_{rss} is the driven oscillation amplitude, $H_{mech}(f) = 1/(1 + j2\pi f \tau_{mech})$ is a one-pole low-pass filter that accounts for the intrinsic mechanical response of the resonator, where $\tau_{mech} = Q/\pi f_r$ is the mechanical time constant of the resonator, and Q is the mechanical quality factor at eigenfrequency f_r. In turn, thermal fluctuation noise (in Hz^{-1}) is given by [181, 186, 187]:

$$S_{y,TF}(f) = \frac{4 k_B T^2 \alpha^2}{G} \left| H_{th}(f) \right|^2, \tag{5.3}$$

where G (in W/K) is the total thermal conductance between the resonator and its environment and $H_{th}(f) = 1/(1 + j2\pi f\tau_{th})$ is a one-pole low-pass filter that accounts for the intrinsic thermal response of the resonator, where τ_{th} is the thermal time constant. α is the temperature coefficient of fractional frequency shifts (in K^{-1}).

The responsivity of the fractional frequency shift to incident radiation (in W^{-1}) can be expressed as:

$$R = \frac{\gamma\alpha}{G_{eff}}\left|H_{th,eff}(f)\right|, \tag{5.4}$$

where γ is the absorption coefficient at the target detection wavelength (e.g., $\gamma = 0.4$ at 2 THz in this work). G_{eff} and $H_{th,eff}$ are the effective thermal conductance and thermal filter. They are equal to G and H_{th} for uniform absorption of radiation across the entire membrane area. We assume $G_{eff} = G$ in this section, and re-evaluate them using finite element analysis for the membrane functionalizes with a localized absorber in the following Methods & Results Section.

In the limit case where thermomechanical noise is minimized relative to thermal fluctuation noise, we can substitute Eq. 5.3 and 5.4 into Eq. 5.1 which yields the performance limit:

$$\mathrm{NEP_{TF}} = \frac{\sqrt{S_{y,TF}}}{R} = \frac{\sqrt{4k_BT^2G}}{\gamma}. \tag{5.5}$$

It is worth noting that in this limit, NEP becomes independent of both the intrinsic thermal filter H_{th} and the temperature coefficient α.

Since many noise sources scale with detector area A_{det}, the smallest detectable radiation intensity (in W/m^2) is often a more universal metric than the smallest measurable power (in W). Specific detectivity $D^* = \sqrt{A_{det}}/\mathrm{NEP}$ is therefore useful for quantifying the ultimate performance limit of detectors. The limit case for D^* occurs when

$S_y = S_{y,TF}$ and all heat transfer occurs via radiation, yielding

$$G = G_{rad} = 4A_{rad}\sigma_{SB}\varepsilon T^3, \tag{5.6}$$

where $A_{rad} = 2L^2$ accounts for radiative heat transfer on both sides of the membrane. By substituting G_{rad} into Eq. 5.5, we obtain the expression of D^* limited solely by thermal photon fluctuation:

$$D^*_{\text{TF, photon}} = \frac{\sqrt{A_{det}}}{\text{NEP}_{\text{TF}}|_{G=G_{rad}}} = \frac{\gamma}{\sqrt{32k_B\sigma_{SB}T^5\varepsilon}}. \tag{5.7}$$

For the case of a blackbody thermal detector (i.e., $\gamma = \varepsilon = 1$), and for $A_{det} = L^2$, Eq. 5.7 yields $D^*_{\text{TF, photon}} \approx 1.3 \times 10^{10}$ cm $\cdot \sqrt{\text{Hz}}$/W. This is slightly different from the commonly known fundamental limit $D^* \approx 1.8 \times 10^{10}$ cm $\cdot \sqrt{\text{Hz}}$/W for thermal detectors [163], that assumes thermal radiation occurring on one side of the detector only (i.e., $A_{det} = A_{rad}$). Furthermore, considering our specific case of a THz absorbing membrane resonator in which $\gamma = 0.4$ in the THz range and $\varepsilon = 0.1$ in the thermal range, the limit for the sensor in this work is $D^*_{\text{TF, photon}} \approx 1.6 \times 10^{10}$ cm $\cdot \sqrt{\text{Hz}}$/W.

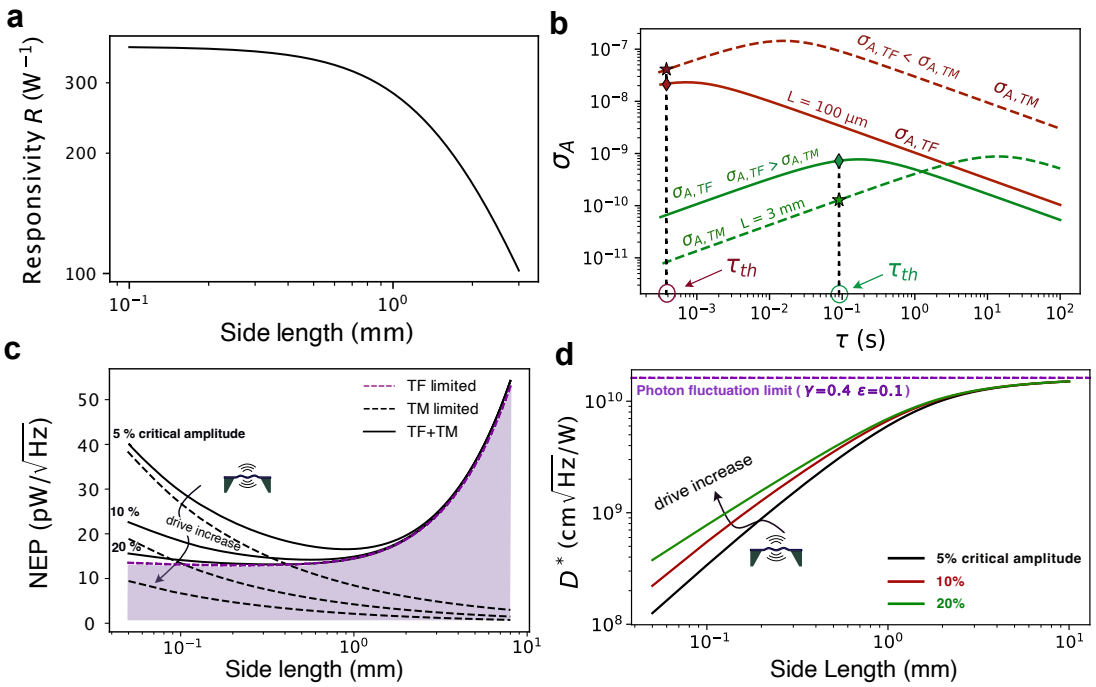

Figure 5.1: (a) Thermal responsivity of fractional frequency shifts for square SiN membranes of various lengths L, and a fixed thickness of 90 nm. (b) Theoretical Allan deviations σ_A of two SiN membranes with significantly different side lengths ($L = 3$ mm & $L = 100$ μm), considering thermomechanical noise $\sigma_{A,TM}$ (dashed lines) and thermal fluctuation noise $\sigma_{A,TF}$ (solid lines). (c) Noise equivalent power (NEP) of SiN membranes of various side lengths L with fixed thickness of 90 nm, considering thermomechanical (TM) and thermal fluctuation (TF) noise. Three sets of traces represent NEP of resonator at different driven vibration amplitudes. (d) Specific detectivity $D^* = \sqrt{A_{det}}/\text{NEP}$ of SiN membrane resonators considering both thermomechanical and thermal fluctuation noises at different vibration amplitudes. All calculations consider a total emissivity of $\varepsilon = 0.1$ and absorption $\gamma = 0.4$ at the detection frequency (~ 2 THz in this work).

For optimizing NEP of membrane resonator-based radiation sensors, Eq. 5.1 outlines that we can either seek to minimize S_y or maximize R. We first investigate the contribution of R, assuming $H_{th,eff} = 1$ (i.e., sampling time $\tau \gg \tau_{th}$). As shown in Fig. 5.1, we find that R is optimized for smaller membranes, but only with modest gains at sub-mm dimensions. In Eq. 5.4, we evaluate G using a closed-form heat transfer model [170] that depends on the resonator dimensions (side length L, thickness t), on the material thermal conductivity ($k = 2.7$ W/m $\cdot$ K) and on the membrane hemispherical total emissivity ε of approximately 0.1 for a plain 90-nm-thick SiN [170]. In turn, for the first few mechanical

modes, α is well approximated by [170]:

$$\alpha \cong \frac{E\alpha_T}{2\sigma(1-\nu)}, \tag{5.8}$$

where $E = 300$ GPa is Young' s modulus, $\alpha_T = 2.2\times10^{-6}$ K^{-1} is the membrane material thermal expansion coefficient, $\sigma = 100$ MPa is the built-in tensile stress, and $\nu = 0.28$ is the Poisson ratio. For higher order modes, Eq. 5.8 generally yields an error of less than 20%, which is detailed in previous works [170, 188]. Thus, for a given set of material constants, the dependency of R on the dimensions of the membrane resonators arises solely from the dimensional dependency of G. As shown in Fig. 5.1(a), minimizing L increases the membrane responsivity by reducing thermal radiative heat transfer with the environment. However, such improvement gradually plateaus for sub-mm values of L, when G becomes strongly dependent on solid-state conduction and weakly dependent on L. Extended discussion on the contribution of radiation and conduction heat transfer in membranes can be found in previous works [170, 180].

In contrast to R varying weakly with membrane dimensions at $L < 1$ mm, we find that frequency noises can be minimized significantly using membrane resonators with large dimensions (i.e., $L > 1$ mm). We compute theoretical Allan deviation σ_A (see Appendix. C.2) from expected fractional frequency noise spectral density $S_{y,TF}$ and $S_{y,TM}$. In Fig. 5.1(b) we compute, as an example, the theoretical σ_A of 90-nm-thick SiN membrane resonators of significantly different sizes (i.e., $L = 3$ mm, and $L = 100$ μm), considering actuation of mode (1,1) at an arbitrary low drive amplitude (i.e., 10% of the critical drive given by $A_{crit} = 0.56\ L\sqrt{\sigma/QE}$ [188]). We scale m_{eff}, f_r, Q, A_{crit} and G with the dimension L using the relations given in Appendix. C.3, from which we consider $Q \approx 3\times10^5$ and 1×10^6 for membranes of $L = 100$ μm and 3 mm. For the large membrane, we obtain $\tau_{mech} \gg \tau_{th}$ such that thermomechanical noise ($\sigma_{A,TM}$) is significantly filtered (i.e., attenuated) when sampling at the resonator thermal time constant τ_{th}, i.e.,

when sampling as fast as the membrane can thermally respond ($\tau_{th} = 100$ ms). This is not the case for the smaller membrane, in which thermomechanical noise is a dominant noise source that adds to thermal fluctuations. As a result, at $\tau_{th} = 100$ ms, the total noise in the large membrane ($\sigma_A \approx \sigma_{A,TF} \approx 1 \times 10^{-9}$) is two orders of magnitude lower than in the small membrane ($\sigma_A \approx \sigma_{A,TM} \approx 1 \times 10^{-7}$).

Finally, we strike a balance between optimizing responsivity R and frequency stability, from which we find that the optimal resonator dimensions are on the order of 1 mm. Fig. 5.1(c) presents a more comprehensive view on resonators NEP over a range of commonly used sizes (i.e., $L = 50$ μm and 10 mm). Here, we calculate NEP directly using Eq. 5.1 considering $S_y = S_{y,TF} + S_{y,TM}$. We note that NEP deteriorates at both extreme large and small L. As L becomes smaller than 1 mm, the NEP is affected by excessive levels of thermomechanical noise, unless driven at an amplitude close to A_{crit}, which is often challenging in practice [124, 189–191]. Conversely, as L gets exceedingly large (i.e., $L > 3$ mm), NEP is harmed by diminishing R (see Fig. 5.1(a)). Consequently, as shown in Fig. 5.1(c), NEP is inherently optimal within the range 1 mm $< L <$ 3 mm. Interestingly, a similar optimal range was recently observed experimentally in [192] by systematic testing of membranes of several dimensions. We then normalize the NEP values presented in Fig. 5.1(c) by $\sqrt{A_{det}} = L$ to obtain D^* in Fig. 5.1(d) and compare it to our photon fluctuation-limited $D^*_{\text{TF, photon}} \approx 1.6 \times 10^{10}$ cm $\cdot \sqrt{\text{Hz}}/\text{W}$. We note that when $L < 1$ mm, D^* degrades quickly to below $D^*_{\text{TF, photon}}$ due to excessive thermomechanical noise and plateauing thermal responsivity as membrane size decreases. In contrast, at larger L, D^* gradually approaches $D^*_{\text{TF, photon}}$ due to thermal conductance being dominated by radiation ($G \approx G_{rad}$).

5.1.6 Methods & Results

Building on this analysis we opt for a relatively large 3.2×3.2 mm square SiN membrane resonator as the sensing platform, which we functionalize with a 70-nm-thick ti-

tanium metasurface to enable THz absorption. The THz absorption spectrum of the metasurface is designed using Ansys Lumerical finite-difference-time-domain (FDTD) simulation software, from which we expect a peak $\gamma_{peak} = 0.4$ at ~ 2 THz, as shown in Fig. 5.2(a). We deposit this metasurface with a 1-mm diameter D at the center of the membrane (see Fig. 5.2a) to ensure a sufficiently large peripheral area of plain SiN for optomechanical interrogation. This metal-free region prevents the interrogation laser source (i.e., a 1564 nm distributed feedback laser) from impinging and heating the titanium metasurfaces which could degrade resonators frequency stability due to laser fluctuation [179, 181, 193].

By covering only part of the membrane resonator, we need to adjust our responsivity, NEP and D^* calculation from those of a uniform membrane in Theory Section. We therefore solve a combined modes heat equation (i.e., coupled radiation and conduction) of the SiN membrane resonator numerically in MATLAB by defining a heating zone at the geometric center of the membrane, which accounts for the effective localized heating area (i.e., effective diameter of the titanium metasurface D). Fig. 5.2(b) exhibits the variation in R when a $D = 1$ mm localized titanium metasurface incorporated at the geometric center of a SiN membrane resonator at different sizes L. We find that our approach (i.e., $D = L/3 = 1$ mm) sacrifices $\sim 40\%$ of R, compared with a uniformly heated (i.e., $D = L = 3$ mm) SiN membrane resonator. Using this adjusted R and the thermal fluctuation noise $S_{y,TF}$ for a full membrane (See Eq. 5.3), we predict theoretical minimum NEP ≈ 13 pW/$\sqrt{\text{Hz}}$ for our sensor geometry in Fig. 5.2(a). In addition, using detector area $A_{det} \approx 0.79$ mm^2, we predict $D^* \approx 7 \times 10^9$ cm $\cdot \sqrt{\text{Hz}}$/W as the theoretical maximum detectivity for this particular geometry.

The plain SiN membrane resonator is fabricated in-house using a 90-nm-thick low-pressure chemical vapor deposition (LPCVD) low-stress SiN-on-silicon wafer. The titanium is deposited onto the surface of the SiN membrane resonator via electron beam evaporation through a custom-made shadow mask to form the metasurface. Detailed

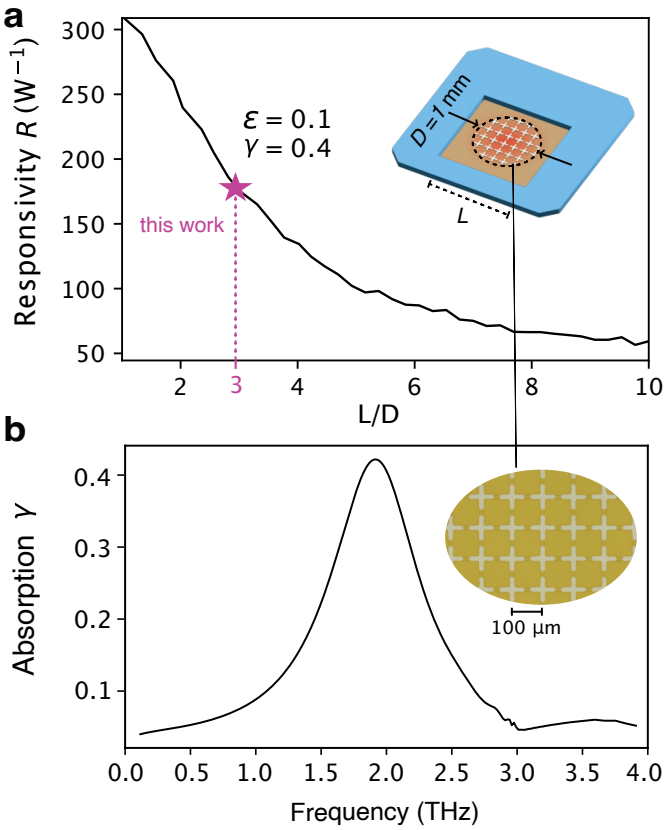

Figure 5.2: (a) Numerically computed thermal responsivity R of a $D = 1$ mm diameter localized THz metasurface absorber incorporated on top of SiN membrane resonators of various side lengths L. The purple star indicates the responsivity of the fabricated device. (b) Numerically computed absorption spectrum of the fabricated metasurface in the THz frequency range. Inset: microscope photograph of the fabricated metasurface.

fabrication processes are described in previous work [194].

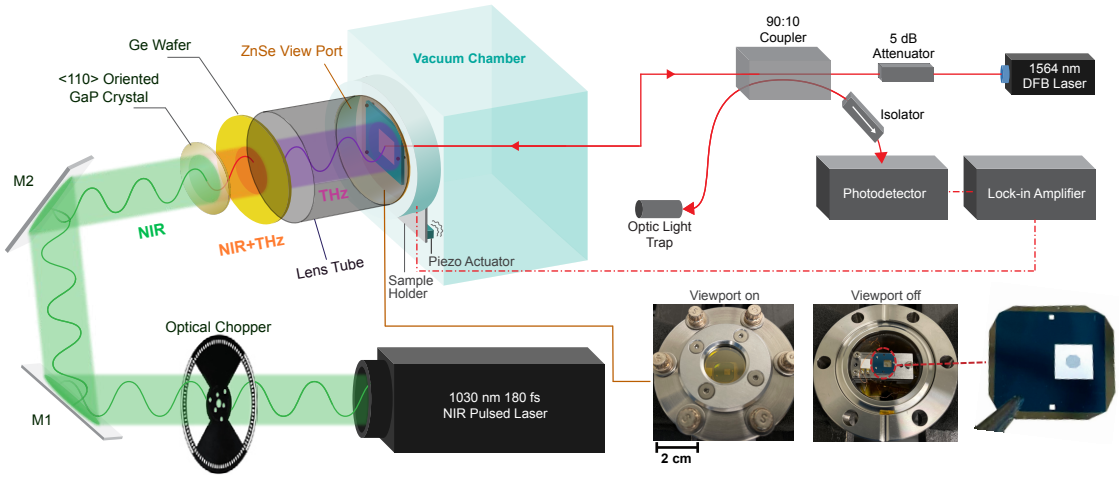

Figure 5.3: Schematics of the overall experimental setup which includes a laser interferometer outside of the vacuum chamber for resonator readout, SiN membrane resonator mounted inside the chamber, and terahertz nonlinear generation process using near infrared (NIR) pulsed laser incident on a gallium phosphite GaP crystal.

Once fabricated, the resonator is placed in a custom-made portable high vacuum ($\sim 10^{-6}$ hPa) chamber [195] to minimize convective heat transfer and damping by air. The resonator is mounted on a steel plate by three pairs of disc magnets and mechanically excited via a piezo actuator. The membrane is aligned with the center of a Zinc Selenide (ZnSe) view port for easy optical alignment (See Fig. 5.3). A single-mode optical fiber tip is pointed at the back side of the resonator for optical interrogation of its mechanical vibration. We probe vibration signal of the resonator using a custom-assembled laser interferometer [196] located outside the vacuum chamber and consisting of a 1564 nm Orion^{TM} distributed feedback (DFB) laser, a 5 dB optical attenuator, a 90:10 coupler and a Thorlabs PDA20CS2 photodetector. The combined use of the optical attenuator and coupler reduces the laser power to 11.7 μW before reaching the SiN membrane resonator. This largely attenuated laser power produces sufficient signal for detection, while preventing any noticeable laser fluctuation from degrading resonator frequency stability [179, 181, 193].

Choosing an ideal mechanical mode for thermal sensing requires simultaneously op-

timizing three parameters: f_r, Q and A_{rss}, to suppress thermomechanical noise $S_{y,TM}$ as Eq. 5.2 indicated. We therefore first perform a frequency sweep to locate the optimum mechanical mode of our sample. Note that the optimum mode must be determined experimentally since these three parameters are sensitive to variations in sample mounting conditions. During our experiment, we chose a high Q-factor ($Q = 870,000$) mechanical eigenmode (i.e., mode order 2,3) at 124 kHz. This eigenmode also exhibits a higher demodulated signal amplitude (i.e., higher A_{rss}) compared with other modes under the same actuation signal. Additional information regarding other mechanical modes can be found in Appendix. C.6. We use a Zurich Instrument Ltd. MFLI lock-in amplifier (LIA) to excite our sample at this mode below the critical amplitude A_{crit} to avoid frequency stability degradation due to nonlinearity. We track its resonance frequency shift upon THz light absorption via a built-in phase-locked loop (PLL) frequency tracking function. We set both demodulation bandwidth (5 kHz), and sampling rate (32,000 Sa/S) to very high values, which we can numerically average to lower effective sampling rates in post processing. We set the PLL bandwidth to 8 Hz, which ensures that the PLL tracking speed is roughly five times faster than the thermal time constant $\tau_{th} \approx 100$ ms) of our plain 3.2×3.2 mm SiN membrane [180, 181], such that the true thermal response of the SiN membrane resonator can be recorded without filtering.

We generate collimated THz radiation with spectrum centered around 1.8 THz via optical rectification of a collimated near-infrared (NIR) pulsed laser beam (1 mJ pulse energy, 180 fs pulse duration, 6 kHz pulse repetition rate) in a 2-mm-thick $< 110 >$-oriented gallium phosphide (GaP) crystal (see Fig. 5.3). The generated THz radiation is pulsed with the same repetition rate but is perceived as CW by our sensor of comparatively slow response time ($\tau_{th} \approx 200$ ms). Similar THz generation process is detailed in Cui *et. al* [197]. A germanium (Ge) wafer that is transparent to THz radiation is placed in the optical path (see Fig. 5.3) to block the residual NIR light, ensuring that only the THz light can reach the SiN membrane resonator. Additionally, a 20-cm long,

circular hollow lens tube is positioned between the Ge wafer and the ZnSe viewport of the portable vacuum chamber (see Fig. 5.3), to prevent any possible external stray light from reaching the sample. This relatively long (20 cm) propagation length also geometrically attenuates, via divergence, parasitic thermal radiation generated in the Ge wafer due to NIR absorption, while the coherent THz beam remains collimated to an approximately constant beam diameter (6 mm).

We first validate the heat transfer model in our resonators by recording the fractional mechanical frequency shifts $\delta f/f_r$ in our sample when exposed to a 6-mm-diameter THz beam, modulated at 2 Hz via an optical chopper. This is shown in Fig. 5.4(a), in which the effective sampling rate is set to match the PLL bandwidth (8 Hz). From this figure, we obtain an experimental thermal response time $\tau_{th} \approx 200$ ms that is roughly two times larger than the expected τ_{th} of a plain SiN membrane [180, 181]. This is in close agreement with finite element simulations (see Appendix. C.4), that predicts reduced response speed due to THz absorption occurring in a localized region, and the additional thermal mass of the titanium metastructures. We then repeat the same experiment at different optical modulation frequencies (from 2 Hz to 8 Hz), from which we obtain the expected frequency roll-off a one-pole low pass filter of thermal time constant τ_{th} (see Fig. 5.4b).

We then measure the effective optical absorption ($\gamma_{eff} \approx 27\%$) of our metasurface for the specific THz source used in for our experiment, which allow us to extract the sensor responsivity. We perform electro-optic sampling (EOS) [197] to measure the THz emission power spectrum generated by non-linear conversion in the GaP crystal (see Fig. 5.3c, purple curve). We then compare this emission spectrum to the absorption spectrum of our metasurface (see Fig. 5.2b). This comparison is shown in Fig. 5.4(c), from which we infer that our metasurfaces absorbs $\gamma_{eff} \approx 27\%$ of the incident THz light for the source used in the present experiments (i.e., for a source frequency spanning from 0.5 THz to 4 THz, see Fig. 5.4(c). This is different than the peak absorption

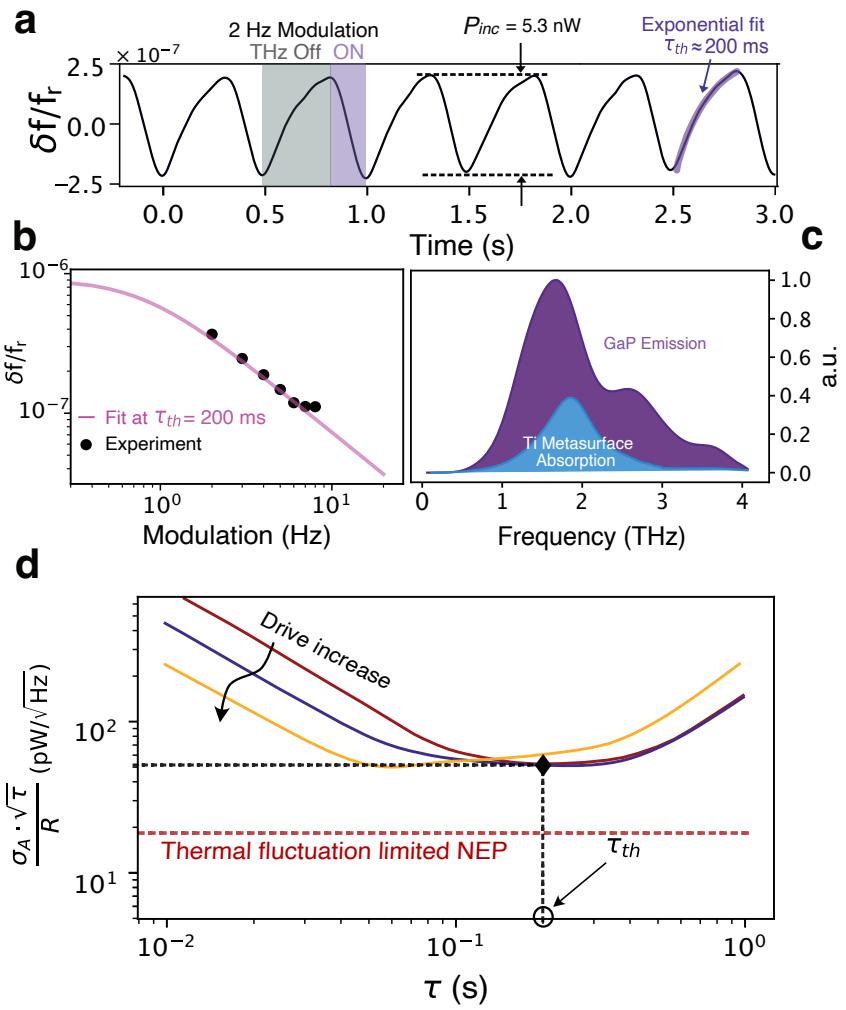

Figure 5.4: (a) Experimental fractional frequency shift $\delta f/f_r$ time trace upon terahertz absorption at 2 Hz optical modulation and filtered at phase-lock loop (PLL) bandwidth of 8 Hz. The exponential fit shown in purple line yields the thermal time constant τ_{th}. (b) $\delta f/f_r$ amplitude at various optical modulation frequencies. (c) Normalized experimental GaP emission power spectrum matched with simulated absorption power spectrum of the Ti metasurface. (d) Experimental noise equivalent power of our device at different drive amplitudes, estimated from experimental Allan deviation σ_A and thermal responsivity R.

of $\gamma_{eff} \approx 40\%$ at our designed frequency (2 THz in Fig. 5.2b). We therefore adjust our predicted responsivity by 33% from the value predicted in Fig. 5.2(a), i.e., we use $R \approx 120$ W^{-1} in the following. Therefore, the theoretical performance limit can be adjusted by the same 33% as $\text{NEP}_{\text{eff}} \approx 19$ pW/$\sqrt{\text{Hz}}$ and $D^*_{\text{eff}} \approx 4.7 \times 10^9$ cm $\cdot \sqrt{\text{Hz}}$/W.

Using this responsivity, we can relate the measured fractional frequency shift $\delta f/f_r$

in Fig. 5.4(a), to the THz power incident on our metasurface using

$$P_{inc} = \frac{\delta f / f_r}{R}. \tag{5.9}$$

This yields an incident power of 5.3 nW as indicated in Fig. 5.4(a). Likewise, we can normalize this incident power by the area of our metasurface ($\pi D^2/4 = 0.79$ mm^2) to estimate the average intensity of the THz light to 6.7 nW/mm^2 at the metasurface location. We also estimate that $\approx 40\%$ of the generated THz light transmits through the ZnSe viewport [198], such that the incident intensity prior to entering our vacuum chamber is ≈ 16.7 nW/mm^2. Interestingly, this value is close agreement with a comparison measurement taken using a Tydex GC-1D Golay cell, which yields a ≈ 16 nW/mm^2 measured intensity.

Using this confirmed responsivity ($R = 120$ W^{-1}), we can estimate our detector NEP by measuring the Allan deviation noise trace (σ_A) in the absence of incident THz radiation. When noise is predominantly white (as in our case for $\tau \leq \tau_{th}$), NEP can be estimated from the Allan deviation using [167, 171, 173]

$$\text{NEP} \approx \frac{\sigma_A(\tau) \cdot \sqrt{\tau}}{R}. \tag{5.10}$$

From this, we obtain Fig. 5.4(d), which indicates a minimum $\text{NEP}_{\text{eff}} \approx 51$ pW/$\sqrt{\text{Hz}}$ at a sampling time τ_{th}, for our specific broadband terahertz source spanning 0.5–4 THz. Correspondingly, we obtain $\text{NEP}_{\text{peak}} \approx 36$ pW/$\sqrt{\text{Hz}}$ and $D^* = 3.4 \times 10^9$ cm $\cdot \sqrt{\text{Hz}}$/W at our central metasurface design wavelength (2 THz) where absorption is $\gamma_{peak} \approx 0.4$. In addition, we plot theoretical $\text{NEP}_{\text{eff}} \approx 19$ pW/$\sqrt{\text{Hz}}$ in Fig. 5.4(d), indicating the ideal performance of detector when being limited by thermal fluctuation $S_{y,th}$. Our experimental NEP_{eff} is therefore only a factor of 3 from this limit. Reducing this factor will likely be readily possible in future experiments, as we previously achieved frequency noise limited by thermal fluctuations in [181] using a different experimental apparatus.

In the present case, mechanical limitations of our portable vacuum chamber most likely caused non-idealities in our displacement readout interferometer. In Fig. 5.4(d), at $\tau \ll \tau_{th}$, the uptick of our experimental $\mathrm{NEP}_{\mathrm{eff}}$ is caused by noise in our optical readout, combined with R approaching zero for decreasing τ in the denominator of Eq. 5.1. At $\tau \gg \tau_{th}$, $\mathrm{NEP}_{\mathrm{eff}}$ is negatively affected by systematic drift.

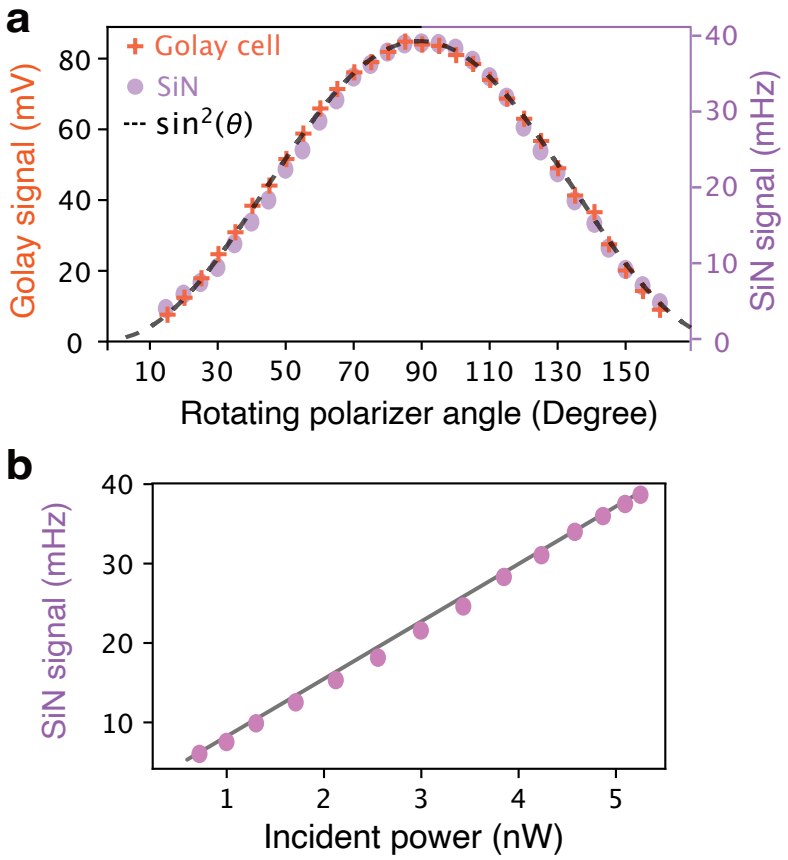

Figure 5.5: (a) Comparison experiment between a commercial Golay cell signal and SiN membrane resonator frequency shift signal δf. The polarizer angle attenuates the incident optical power by a factor $\sin(\theta)^2$. (b) SiN membrane resonator frequency shift signal δf as a function of incident power retrieved from (a).

We finally test our detector with attenuated incident THz optical power to test its linearity. We employ a metasurface thin-film polarizer in front of the ZnSe viewport of the vacuum chamber for varying the intensity of the linearly polarized THz light. When rotating the polarizer away from the maximum transmission orientation by an angle θ, we expect the transmitted THz power to vary by a factor $\sin(\theta)^2$. This is recovered exactly

in Fig. 5.5(a), for both our sensor and the control Golay cell. This exact correspondence with the Golay cell and the expected $\sin(\theta)^2$ signal attenuation confirms the linearity of our sensor, which is better illustrated by plotting the same measured SiN signal against the incident THz power in Fig. 5.5(b). We also note that the polarization sensitivity observed in Fig. 5.5 rules out the possibility that we are detecting thermal light emitted from the NIR-absorbing Germanium wafer, which would be unpolarized.

The same attenuation experiment confirms the performance of our sensor at low optical power. Fig. 5.6 presents the same response as in Fig. 5.4(a), but at different attenuation power (i.e., polarizer angle θ). We confirm that our sensor can clearly detect optical power of 0.7 nW, which was expected by our measured $\mathrm{NEP_{eff}} \approx 51\ \mathrm{pW}/\sqrt{\mathrm{Hz}}$ and data sampling rate of 8 Hz, from which the expected detection limit is 0.14 nW.

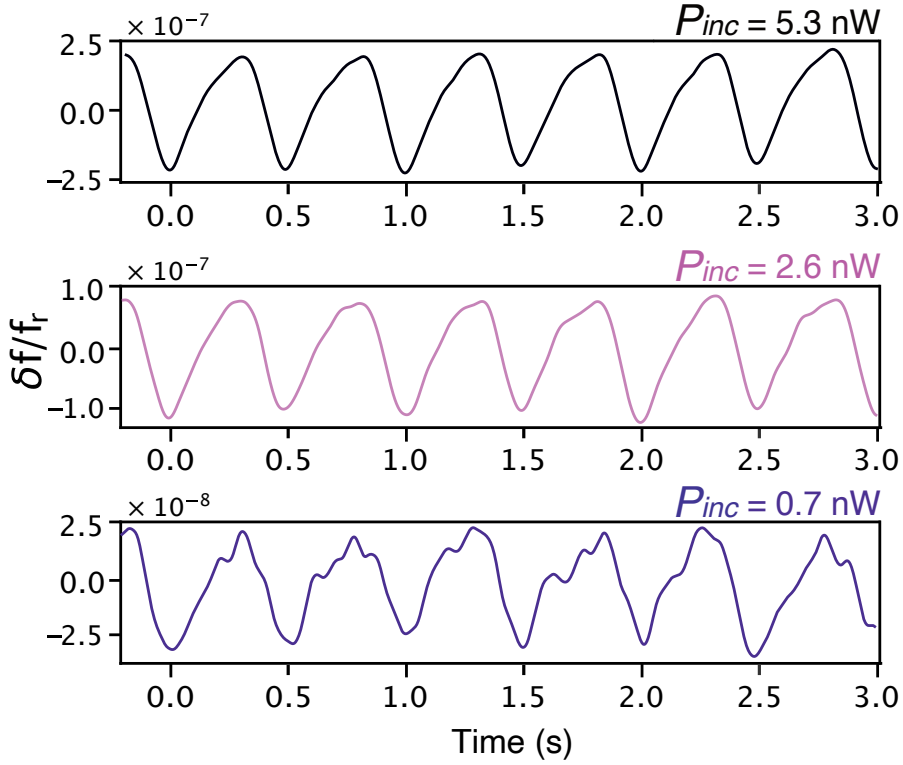

Figure 5.6: Fractional frequency shift $\delta f/f_r$ time trace of the SiN membrane resonator at various levels of attenuated incoming THz power, confirming performances at optical power as low as 0.7 nW.

In conclusion, we show that, when noise sources are well estimated and designed-

for, high performance radiation sensing at long optical wavelengths is possible using ubiquitous square SiN membrane resonators. Using localized terahertz metasurfaces absorbers, a peak detectivity of 3.4×10^9 cm $\cdot \sqrt{\text{Hz}}/\text{W}$ at around 2 THz is experimentally demonstrated. Such detectivity has not been previously realized by any existing nanomechanical resonator, nor by any commercial room-temperature on-chip terahertz detectors. More generally, it is on par with recent record-breaking devices at infrared wavelengths [199,200]. With improvement of our optical readout method already achieved in [181], the performance of our device can feasibly be improved by another factor of 3. Achieving such high level of detectivity while operating at room temperature makes this nanomechanical resonator THz detector particularly interesting for applications that require high-performance single-point detection, such as far-infrared spectroscopy, where response time is often less critical than high detectivity and room-temperature operation.

6. Conclusions & Outlook

In this thesis, we demonstrate that temperature-sensitive, high-Q nanomechanical resonators (NMRs) can exhibit an overall noise profile overwhelmingly dominated by fundamental temperature fluctuation noise. This enables thermal sensing at peak performance, extending far beyond the intrinsic thermal cut-off frequency—by up to 30 times. Reaching the temperature fluctuation noise limit over a large bandwidth thus represents the most significant contribution to the field of nanomechanical thermal sensing. Furthermore, through a comprehensive set of experiments, we validate the proposed frequency noise model, which encompasses commonly encountered frequency noise sources in NMR-based thermal sensors and accounts for the closed-loop frequency tracking scheme. Lastly, we use a membrane resonator functionalized with a localized THz absorber, demonstrating more than an order of magnitude sensing performance (D^*) improvement, compared to state-of-the-art on-chip commercial sensors operating in the THz regime [91]. This body of work, consisting of three articles, therefore contributes to the development of next-generation long-wavelength infrared (LWIR) sensing using nanomechanical resonators.

In the effort to continue developing NMR-based thermal sensors, improvements are needed in both **theoretical** and **practical** aspects. On the **theoretical side**, expanding the scope of the frequency noise model remains a high priority. In this work, our model considers only frequency fluctuations originating from thermomechanical noise, instrument readout noise, and fundamental temperature fluctuation noise. However, frequency fluctuations arising from Duffing nonlinearity may also contribute to the overall noise figure. Therefore, further developing a theoretical model that accurately predicts frequency noise induced by Duffing nonlinearity could further improve the predictability of the model. In addition, as mentioned in **Chapter 4.2**, there is a slight discrepancy in

thermal processes (e.g., thermal filtering and thermal conductance) observed in NMRs, depending on whether one is estimating temperature fluctuations or evaluating thermal responsivity under uniform external heating. Therefore, this newly proposed observation warrants further investigation.

On the **practical side**, although we are able to systematically operate NMRs in a temperature fluctuation noise–dominated regime within our stationary custom-built vacuum chamber, this has not yet been achieved when using a smaller-scale, portable vacuum chamber setup, as shown in **Chapter. 5 (Article 3)**. This is largely because, unlike in the stationary setup where the distance between the optical fiber tip and the NMR surface can be precisely controlled via piezo linear actuators, the portable setup imposes an arbitrarily fixed distance due to manufacturing constraints. This results in an undesirably large optical interferometer cavity length (i.e., 1 mm), as compared with the ideal length of roughly 100 μm, which consequently degrades sensing performance. This issue can be resolved by further modifying the mechanical design of the portable vacuum chamber.

Lastly, a thin-film metal absorber can be deposited on the surface of the NMR, enabling broadband infrared sensing that spans from the mid- to far-infrared range. Combined with a redesigned portable chamber that allows for an optimal interferometer cavity length, this approach could yield the highest-detectivity, room-temperature thermal-based sensor. This, therefore, can be commercially attractive for applications such as Fourier-transform infrared spectroscopy.

A. Supplementary for Article 1

A.1 Finding an optimum range of laser power

The laser power used during the experiment plays a critical role: too high power may cause spurious heating that affects thermal fluctuation readings, while low power increases additive phase noise (thermomechanical and instrumental readout noise) and can therefore prevent observation of fundamental thermal fluctuations. In this supplementary experiment, we empirically identify a suitable range of laser power for observing the dominant effect of thermal fluctuation noise in SiN resonators. We replace the fixed optical attenuator in Fig. 4.3(c) by variable optical attenuator (Thorlabs V1550A) such that the laser power incident on the SiN resonator can be varied. We then drive the 3.2×3.2 mm SiN resonator to an amplitude (≈40 nm) suitable for observation of thermal fluctuation noise, and we record Allan deviations for different laser powers. As shown in Fig. A.1, in the thermal fluctuation region, the Allan deviation varies with laser power when the attenuation is the 0–2.5 dB range, meaning that laser at this intensity heats up the membrane and adds to thermal fluctuation noise. In the optimal 2.5–5.3 dB attenuation range, the characteristic bump of thermal fluctuations frequency noise is clearly noticeable and is now independent of laser power.

Note that a smaller drum resonator can tolerate less laser-absorbed power due to its smaller thermal conductance G [W/K]. To compare with a 3.2×3.2 mm drum resonator which has $G_{3.2\times3.2} = 1.8 \times 10^{-5}$ W/K, a 1.7×1.7 mm SiN drum resonator thermal conductance reduces almost exactly by 50% (e.g., $G_{1.7\times1.7} = 9.3\times10^{-6}$ W/K). In Fig. A.1, we note that for a 3.2×3.2 mm resonator, the effect of laser heating starts to be noticeable at 1.6–2.5 dB attenuation. Therefore, we added a 3 dB safety factor and used a 5 dB attenuator in the experiment to also minimize laser heating for the 1.7×1.7 mm drum resonator. A safety factor larger than 3 dB is unfortunately not possible in our experimental conditions. Such high attenuation would increase detection noise, thus preventing observation of fundamental thermal fluctuation noise.

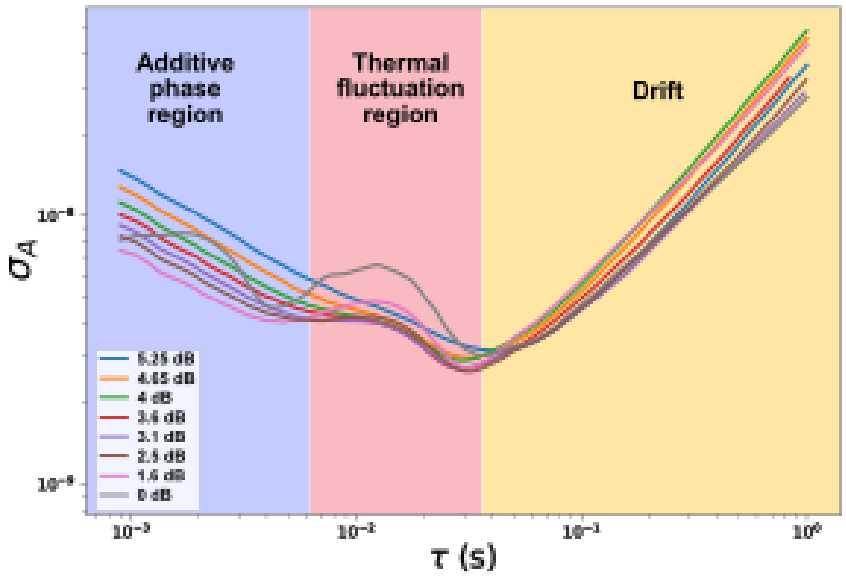

Figure A.1: Experimental Allan deviations of a 3.2×3.2 mm SiN membrane at varying incident laser power.

A.2 Fitting parameters for this study

Device	**Measured A_{rss} (nm)**	**Fitted A_{rss} (nm)**	**Measured κ_d**	**Fitted κ_d**
1.7 × 1.7 mm SiN drum resonator	4	3.5	**0.057**	**0.085**
	9	7.5		
	11	9.5		
	16	14		
	21	18		
3.2 × 3.2 mm SiN drum resonator	7.6	8.4	**0.009**	**0.012**
	14.5	16		
	21	23		
	30	33		
	35.5	39		
6.2 × 6.2 mm SiN drum resonator	5	12	**0.09**	**0.1**
	8.3	20		
	12.9	31		
	16.7	40		
	21.7	52		

Table A.1: Comparison of measured and fitted A_{rss} and κ_d for different SiN drum resonators.

B. Supplementary for Article 2

B.1 Heat transfer simulation

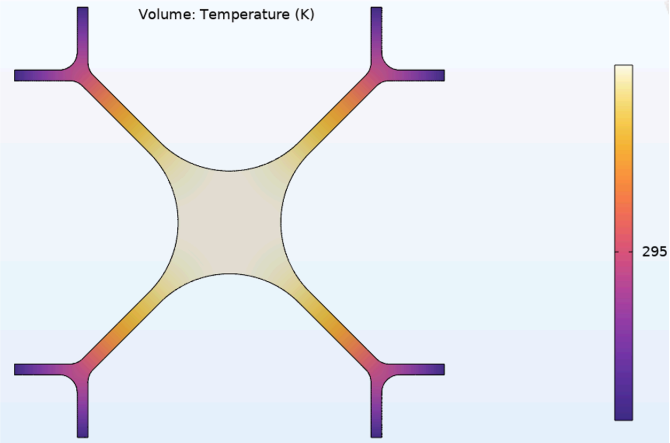

Figure B.1: 2-D temperature profile of the SiN nanomechanical resonator considering solid-state conduction and radiative heat transfer during 1 μWconstant heating.

We perform a heat transfer simulation via COMSOL, considering both solid-state conduction and radiative heat transfer. We apply a uniform heat flux of $Q = 1$ μW being absorbed by the SiN nanomechanical resonator (NMR) surface and set the boundary condition at constant room temperature $T_{room} = 294.15$ K. Fig. B.1 shows the 2-D temperature profile in steady state during constant heating.

In COMSOL, we obtain heat flux leaving the NMR via solid-state conduction for a single tether to be $Q_{cond,1\ tether} = 43.425$ nW. The total heat flux leaving the NMR via conduction can be calculated as $Q_{cond} = 8 \times 43.425 = 347.4$ nW in which the factor of 8 accounts for the total number of tethers supporting the NMR. Due to only two heat transfer modes (e.g., conduction and radiation) included in this simulation, we can

calculate the percentage of heat flux leaving the NMR via radiation as:

$$x_{rad} = \frac{Q - Q_{cond}}{Q} = \frac{1 \times 10^{-6} - 347.4 \times 10^{-9}}{1 \times 10^{-6}} \approx 65\%. \tag{B.1}$$

B.2 Effective mass and temperature coefficient of fractional frequency shift simulation

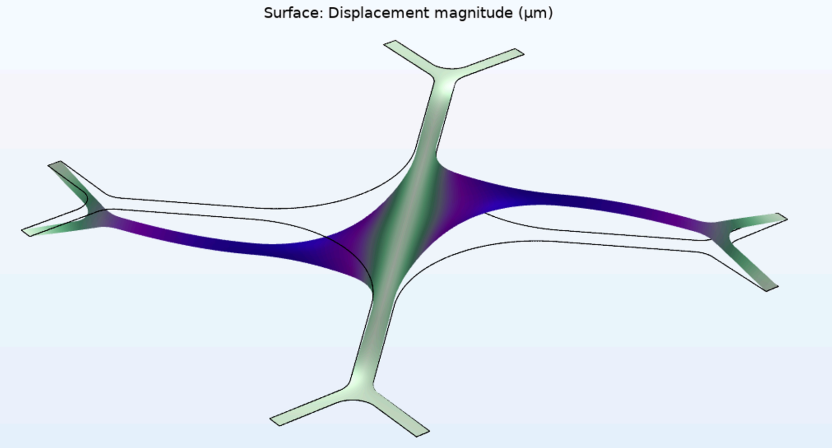

Figure B.2: Mechanical mode (1,2) of the SiN nanomechanical resonator in COMSOL simulation.

Using SiN material density $\rho = 2900$ kg/m^3, and the dimension of the fabricated NMR, we perform dynamic vibration analysis in COMSOL which solves for eigen modes and their corresponding eigen frequencies f_r. According to this simulation, at room temperature $T_0 = 294.15$ K, f_r of mechanical mode (1,2) is 60.8 kHz (see Fig. B.2) when the tensile stress of the SiN membrane is set to $\sigma = 70$ MPa. This closely aligns with the chosen mode in our experiment ($f_r = 60.2$ kHz, see main text). From this simulation, we also obtain an effective mass, $m_{eff} \approx 36.5$ ng for mode (1,2). This value is roughly a third of the actual mass, $m_0 = hA \cdot \rho$ of the NMR (i.e., $m_{eff} = m_0/2.9$).

By applying uniform heating on the surface of the NMR in COMSOL until its average temperature increases by ≈ 1 K, we observe f_r of the mechanical mode (1,2) decreases

by 393 Hz. From this, we extract the temperature coefficient of fractional frequency $\alpha \approx 6.45 \times 10^{-3}$ K^{-1}. Intriguingly, this value matches closely (i.e., $< 1\%$ discrepancy) with the commonly used equation for estimating α of the fundamental mechanical mode of a drum resonator under tensile stress, listed as follows:

$$\alpha = \frac{E\alpha_T}{2\sigma(1-\nu)}. \tag{B.2}$$

We use Young' s modulus $E = 300$ GPa, Poisson' s ratio: $\nu = 0.27$, thermal expansion coefficient $\alpha_T = 2.2 \times 10^{-6}$ K^{-1} and tensile stress $\sigma = 70$ MPa for this work.

B.3 Frequency fluctuation under varying probing laser power

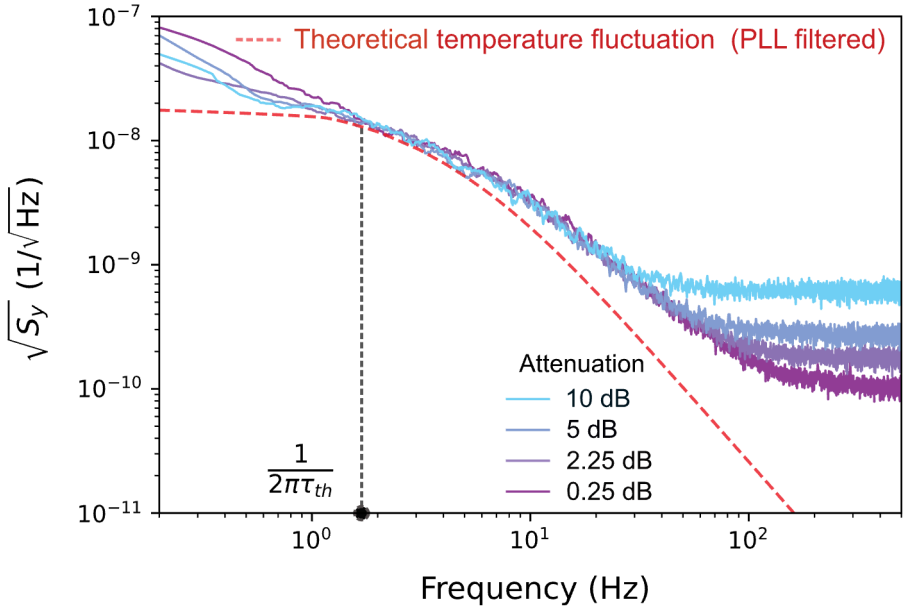

Figure B.3: Frequency fluctuation measurement at fixed vibration amplitude A_{rss} and phase-locked loop settings (i.e., PLL and demodulation bandwidth) with varying laser power. 5dB attenuation is used in the main text.

The power intensity fluctuation of the probing laser is known to induce unwanted frequency noise to the temperature-sensitive NMR. This effect arises from the probing laser acting as a continuous, point heat source on the NMR. When the laser power fluctuates, it induces frequency fluctuation whose magnitude scales with both the laser power and the NMR' s thermal responsivity R (see Eq. 4.12 in main text), on the timescale set by NMR' s thermal time constant τ_{th}.

To investigate this, we use a variable optical attenuator (Thorlabs V1550A) to vary the incident laser power on the NMR for multiple traces of frequency noise measurement. In Fig. B.3, we present frequency noise measurements at different laser power attenuation levels, ranging from 0.25 to 10 dB. We see no increase of the NMR noise when reducing attenuation below the value used in the main text (5 dB). In turn, a low attenuation (i.e., high laser power) helps improve the displacement sensitivity S_x of the readout instrument, resulting in a reduction in readout noise $S_{y,read}^{PLL}$ at higher sampling frequency ($f \gg 1/2\pi\tau_{th}$).

C. Supplementary for Article 3

C.1 Fractional frequency noise spectral density in angular frequency $S_y(\omega)$

In this paper we express $S_y(f)$ in units of Hz^{-1} to match the commonly used unit for noise equivalent power NEP ($\mathrm{W}/\sqrt{\mathrm{Hz}}$). However, in the context of mechanical oscillator (i.e., resonator), frequency noise is often expressed as $S_y(\omega)$ in angular frequency $\mathrm{rad/s}^{-1}$. Below, we provide the relevant equations for one-sided $S_y(\omega)$. Thermomechanical noise in $\mathrm{rad/s}^{-1}$ is given by:

$$S_{y,TM}(\omega) = \frac{k_B T}{\pi m_{\mathrm{eff}} \omega_0^3 Q A_{\mathrm{rss}}^2} \left| H_{\mathrm{mech}}(\omega) \right|^2 \tag{C.1}$$

where $H_{\mathrm{mech}}(\omega) = \frac{1}{1+j\omega\tau_{\mathrm{mech}}}$. Thermal fluctuation in $\mathrm{rad/s}^{-1}$ is given by:

$$S_{y,TF}(\omega) = \frac{2k_B T^2 \alpha^2}{\pi G} \left| H_{\mathrm{th}}(\omega) \right|^2 \tag{C.2}$$

where $H_{\mathrm{th}}(\omega) = \frac{1}{1+j\omega\tau_{\mathrm{th}}}$.

C.2 Transformation between fractional frequency noise spectral density $S_y(\omega)$ and Allan deviation σ_A

The theoretical Allan deviation plots in Fig. 5.1(b) are computed by evaluating the following integral:

$$\sigma_A(\tau) = \frac{2}{\sqrt{\pi}\tau} \left[\int_0^\infty \frac{\sin^4(\pi\tau f)}{f^2} S_y(f)\, df \right]^{\frac{1}{2}} \tag{C.3}$$

Note that in Fig. 5.1(b), Allan deviations limited by thermomechanical noise $\sigma_{A,TM}$ and thermal fluctuation noise $\sigma_{A,TF}$ are plotted by plugging Eq. 5.3 and 5.4 into Eq. Eq. C.3 accordingly. To solve Eq. C.3 numerically, we particularly use the built-in `integrate.quad` function in SciPy library with minimum absolute error tolerance (10E-30) to ensure solution accuracy. In Fig. 5.4(d), we estimate the experimental amplitude spectral density $\sqrt{S_y}$ using $\sigma_A(\tau) \cdot \sqrt{\tau}$ due to noise being predominantly white in our case at $\tau \leq \tau_{\text{th}}$.

C.3 Scaling Noise Equivalent Power NEP parameters with SiN membrane resonator sizes

In Fig. 5.1(c), we plotted SiN membrane resonators noise equivalent power NEP as a function of resonator side length L for a 90 nm-thick SiN membrane by dimensionally scaling all parameters in the following equation Eq. 5.1. We begin by scaling all parameters (i.e., $m_{\text{eff}}, f_r, Q, \tau_{\text{mech}}, G, \tau_{\text{th}}$) in $S_{y,TM}(f)$ and $S_{y,TF}(f)$ (refer to Eq. 5.2 and 5.3) with L. For parameters in $S_{y,TM}(f)$, we first scale the effective mass of square SiN membrane resonator m_{eff} with L by:

$$m_{\text{eff}} = \frac{1}{4} L^2 t \rho, \tag{C.4}$$

where $t = 90$ nm is membrane thickness and $\rho = 2900$ kg/m^3 is SiN material density. We then scale the resonance frequency f_r according to m_{eff} by:

$$f_r = \frac{1}{4} \sqrt{\frac{\sigma(m^2 + n^2)t}{m_{\text{eff}}}}, \tag{C.5}$$

where $\sigma = 100$ MPa is the membrane built-in tensile stress, m and n are vibrational mode indices in which for fundamental mode, $m = n = 1$. To scale SiN membrane resonator Q-factor with its side length L, we assume a typical Q-factor of 1 million for a

$L = 3$ mm SiN membrane and then scale Q-factor linearly with L/t, due to the dominant contribution of edge shape in dissipation dilution for membranes. After scaling Q-factor and f_r with L, we can thereafter use these two parameters to obtain the mechanical time constant τ_{mech} using $Q/(f_r\pi)$.

For parameters in $S_{y,TF}(f)$, note that the temperature coefficient of fractional frequency shift α purely depends on material constant, hence, remains the same when L changes. We scale G and τ_{th} according to L using the closed-form heat transfer model presented in our previous work [50]. By scaling all aforementioned parameters in Eq. 5.1 with membrane side length L, we generate Fig. 5.1(c).

C.4 Defining the effective heat transfer area of SiN membrane resonator during terahertz absorption

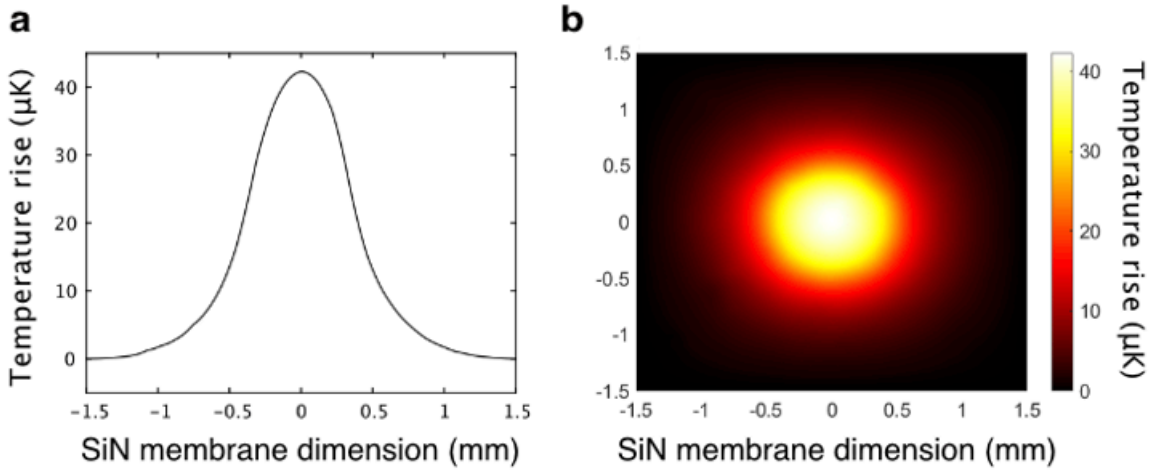

Figure C.1: (a) Interpolation of 2D temperature profile in 1D. (b) 2D temperature profile of SiN membrane when absorbing 1 nW radiation locally.

We construct a volumetric heat transfer equation that includes linearized (i.e., assuming small temperature difference) radiative and solid-state conductive heat transfer

to obtain membrane temperature profile T_{SiN}:

$$-k\nabla^2 T_{\mathrm{SiN}} + \dot{q}_{\mathrm{rad}} = \dot{q}_{\mathrm{absorb}}. \tag{S6}$$

The full details of this heat transfer model is presented in [134]. We then use MATLAB built-in partial differential equation solver to solve Eq. S6 in 2D. To account for localized, non-uniform terahertz absorption $\dot{q}_{\mathrm{absorb}}$ of SiN membrane resonator, we use a rectangular pulse function in MATLAB. In specific, we set the width of the pulse to the effective diameter $D_{\mathrm{absorb}} = 1$ mm of the terahertz metasurface absorber and the amplitude of the pulse to an arbitrary value to represent terahertz power absorption.

After solving Eq. S6, we obtain temperature profile (see Fig.C.1(a) of the SiN membrane during terahertz absorption. Therefore, the effective diameter of heating area ($D_{\mathrm{heating}} \approx 2.2$ mm) can be extracted from this simulation. Note that D_{heating} is mainly affected by SiN membrane internal solid-state conduction (i.e., thermal conductivity and thickness of SiN) and effective absorbing diameter D_{absorb}, thus, independent of SiN membrane side length L and $\dot{q}_{\mathrm{absorb}}$. Inferring from the effective heating area $A_{\mathrm{heating}} = \frac{\pi D_{\mathrm{heating}}^2}{4} = 3.5$ mm^2. Since all solid-state heat transfer is confined within A_{heating}, we can estimate subsequent thermal conductance $G \approx 4.4 \times 10^{-6}$ W/K by solely considering radiation:

$$G = 8A_{\mathrm{heating}}\sigma_{\mathrm{sb}}\varepsilon_{\mathrm{SiN}}T_{\mathrm{room}}^3, \tag{C.6}$$

where σ_{sb} is Stefan–Boltzmann constant, $\varepsilon_{\mathrm{SiN}}$ is the hemispherical total emissivity of SiN membrane of 90 nm thickness and T_{room} is the room temperature. We can then use G to estimate the theoretical thermal time constant τ_{th} of our SiN membrane resonator under localized THz radiation absorption by:

$$\tau_{\mathrm{th}} = \frac{c_{p_{\mathrm{SiN}}}\rho_{\mathrm{SiN}}V_{\mathrm{SiN}} + c_{p_{\mathrm{Ti}}}\rho_{\mathrm{Ti}}V_{\mathrm{Ti}}}{G}, \tag{C.7}$$

where $\rho_{\mathrm{SiN}} = 2900$ kg/m^3 is the SiN membrane density, $c_{p_{\mathrm{SiN}}} = 700$ J/kgK is SiN membrane specific heat capacity, $V_{\mathrm{SiN}} = 3.4\times10^{-13}$ m^3 is the SiN membrane volume associated with A_{heating}, $\rho_{\mathrm{Ti}} = 4500$ kg/m^3 is the titanium density, $c_{p_{\mathrm{Ti}}} = 500$ J/kgK is the specific heat capacity of titanium, $V_{\mathrm{Ti}} = 2.3 \times 10^{-14}$ m^3 is the titanium volume. Eq. C.7 yields a τ_{th} of 170 ms which is in close agreement with our experimental τ_{th} of 200 ms. The 15% discrepancy can be due to uncertainties in documented SiN and Ti material properties values.

C.5 Estimating thermal responsivity R under localized heating

With the localized temperature profile T_{SiN} solved in C.4, we can then calculate the in-plane stress variation profile upon localized heating σ_r in cylindrical coordinate system using:

$$\sigma_r(r) = -\alpha E \left[\frac{1}{r^2} \int_0^r r \Delta T_{\mathrm{SiN}}(r)\, dr + \frac{1+\nu}{1-\nu} \cdot \frac{\overline{\Delta T_{\mathrm{SiN}}}}{2} \right], \tag{C.8}$$

where $\Delta T_{\mathrm{SiN}} = T_{\mathrm{SiN}}(r) - T_{\mathrm{room}}$ and $\overline{\Delta T_{\mathrm{SiN}}}$ is the average temperature difference. After obtaining the stress variation profile, we can then solve the eigenvalue of the following partial differential equation numerically in MATLAB to obtain SiN membrane resonance frequency f_r upon a specific amount of localized heat absorption:

$$\frac{1}{r}\frac{\partial}{\partial r}\left((\sigma + \sigma_r) r \frac{\partial U(r,t)}{\partial r} \right) - \rho \frac{\partial^2 U(r,t)}{\partial t^2} = 0, \tag{C.9}$$

where $U(r,t)$ represents the out-of-plane displacement of the membrane. We vary $\dot{q}_{\mathrm{absorb}}$ in Eq. S6 and record the corresponding fractional resonance frequency shift $\delta f / f_r$ in Eq. C.9 to simulate thermal responsivity R under the condition of localized heating (i.e., $R = \frac{\delta f / f_r}{\delta P_{\mathrm{abs}}}$).

C.6 Mechanical modes, Q-factors and demodulated signal amplitudes

f_r	Q-factor	Demodulation amplitude under 500 μV actuation signal
39 kHz	122,980	12 μV
57 kHz	210,116	11 μV
79 kHz	86,964	32 μV
86.5 kHz	281,126	180 μV
103.5 kHz	88,902	190 μV
104.5 kHz	115,326	8 μV
124.45 kHz	870,334	190 μV

Table C.1: Measured Q-factors and demodulation amplitudes for various resonance frequencies under 500 μV actuation signal.

References

[1] A. Das, M. L. Mah, J. Hunt, and J. J. Talghader, "Thermodynamically limited uncooled infrared detector using an ultra-low mass perforated subwavelength absorber," *Optica*, vol. 10, no. 8, pp. 1018–1028, 2023.

[2] A. Rogalski, "Infrared detectors: Status and trends," *Prog. Quantum. Electron.*, vol. 27, no. 2-3, p. 59–210, 2003.

[3] Antoni Rogalski, *Infrared Detectors, 2nd Edition*. CRC Press, 2010.

[4] M. R. Watts, M. J. Shaw, and G. N. Nielson, "Microphotonic thermal imaging," *Nature Photonics*, vol. 1, no. 11, pp. 632–634, 2007.

[5] N. Snell, C. Zhang, G. Mu, A. Bouchard, and R. St-Gelais, "Heat transport in silicon nitride drum resonators and its influence on thermal fluctuation-induced frequency noise," *Physical Review Applied*, vol. 17, no. 4, p. 044019, 2022.

[6] S. Schmid, L. G. Villanueva, and M. L. Roukes, *Fundamentals of nanomechanical resonators*, vol. 49. Springer, 2016.

[7] B. Xu, P. Zhang, J. Zhu, Z. Liu, A. Eichler, X.-Q. Zheng, J. Lee, A. Dash, S. More, S. Wu, *et al.*, "Nanomechanical resonators: toward atomic scale," *Acs Nano*, vol. 16, no. 10, pp. 15545–15585, 2022.

[8] M. LaHaye, O. Buu, B. Camarota, and K. Schwab, "Approaching the quantum limit of a nanomechanical resonator," *Science*, vol. 304, no. 5667, pp. 74–77, 2004.

[9] B. Arash, J.-W. Jiang, and T. Rabczuk, "A review on nanomechanical resonators and their applications in sensors and molecular transportation," *Applied physics reviews*, vol. 2, no. 2, 2015.

[10] A. Cupertino, D. Shin, L. Guo, P. G. Steeneken, M. A. Bessa, and R. A. Norte, "Centimeter-scale nanomechanical resonators with low dissipation," *Nature Communications*, vol. 15, no. 1, p. 4255, 2024.

[11] M. S. Hanay, S. Kelber, A. K. Naik, D. Chi, S. Hentz, E. C. Bullard, E. Colinet, L. Duraffourg, and M. L. Roukes, "Single-protein nanomechanical mass spectrometry in real time," *Nature Nanotechnology*, vol. 7, no. 9, pp. 602–608, 2012.

[12] J. Chaste, A. Eichler, J. Moser, G. Ceballos, R. Rurali, and A. Bachtold, "A nanomechanical mass sensor with yoctogram resolution," *Nature Nanotechnology*, vol. 7, no. 5, pp. 301–304, 2012.

[13] Y.-T. Yang, C. Callegari, X. Feng, K. L. Ekinci, and M. L. Roukes, "Zeptogram-scale nanomechanical mass sensing," *Nano letters*, vol. 6, no. 4, pp. 583–586, 2006.

[14] E. Buks and B. Yurke, "Mass detection with a nonlinear nanomechanical resonator," *Physical Review E—Statistical, Nonlinear, and Soft Matter Physics*, vol. 74, no. 4, p. 046619, 2006.

[15] G. Bhattacharya, S. McMichael, I. Lionadi, P. Biglarbeigi, D. Finlay, P. Fernandez-Ibanez, and A. F. Payam, "Mass and stiffness deconvolution in nanomechanical resonators for precise mass measurement and in vivo biosensing," *ACS nano*, 2024.

[16] A. Martín-Pérez and D. Ramos, "Nanomechanical hydrodynamic force sensing using suspended microfluidic channels," *Microsystems & nanoengineering*, vol. 9, no. 1, p. 53, 2023.

[17] J. Moser, J. Güttinger, A. Eichler, M. J. Esplandiu, D. Liu, M. Dykman, and A. Bachtold, "Ultrasensitive force detection with a nanotube mechanical resonator," *Nature Nanotechnology*, vol. 8, no. 7, pp. 493–496, 2013.

[18] D. Hälg, T. Gisler, Y. Tsaturyan, L. Catalini, U. Grob, M.-D. Krass, M. Héritier, H. Mattiat, A.-K. Thamm, R. Schirhagl, *et al.*, "Membrane-based scanning force microscopy," *Physical Review Applied*, vol. 15, no. 2, p. L021001, 2021.

[19] Y. Chen, S. Liu, G. Hong, M. Zou, B. Liu, J. Luo, and Y. Wang, "Nano-optomechanical resonators for sensitive pressure sensing," *ACS Applied Materials & Interfaces*, vol. 14, no. 34, pp. 39211–39219, 2022.

[20] S. Jiang, X. Gong, X. Guo, and X. Wang, "Potential application of graphene nanomechanical resonator as pressure sensor," *Solid State Communications*, vol. 193, pp. 30–33, 2014.

[21] C. Reinhardt, H. Masalehdan, S. Croatto, A. Franke, M. B. K. Kunze, J. Schaffran, N. Sültmann, A. Lindner, and R. Schnabel, "Self-calibrating gas pressure sensor with a 10-decade measurement range," *ACS Photonics*, vol. 11, no. 4, pp. 1438–1446, 2024.

[22] S. Barzanjeh, A. Xuereb, S. Gröblacher, M. Paternostro, C. A. Regal, and E. M. Weig, "Optomechanics for quantum technologies," *Nature Physics*, vol. 18, no. 1, pp. 15–24, 2022.

[23] A. H. Safavi-Naeini, J. Chan, J. T. Hill, T. P. M. Alegre, A. Krause, and O. Painter, "Observation of quantum motion of a nanomechanical resonator," *Physical Review Letters*, vol. 108, no. 3, p. 033602, 2012.

[24] L. Laurent, J.-J. Yon, J.-S. Moulet, M. Roukes, and L. Duraffourg, "12-μ m-pitch electromechanical resonator for thermal sensing," *Physical Review Applied*, vol. 9, no. 2, p. 024016, 2018.

[25] M. Piller, P. Sadeghi, R. G. West, N. Luhmann, P. Martini, O. Hansen, and S. Schmid, "Thermal radiation dominated heat transfer in nanomechanical silicon nitride drum resonators," *Applied Physics Letters*, vol. 117, no. 3, 2020.

[26] X. Zhang, E. Myers, J. Sader, and M. Roukes, "Nanomechanical torsional resonators for frequency-shift infrared thermal sensing," *Nano Letters*, vol. 13, no. 4, pp. 1528–1534, 2013.

[27] M. Piller, J. Hiesberger, E. Wistrela, P. Martini, N. Luhmann, and S. Schmid, "Thermal ir detection with nanoelectromechanical silicon nitride trampoline resonators," *IEEE Sensors Journal*, vol. 23, no. 2, pp. 1066–1071, 2022.

[28] Y. Hui, J. S. Gomez-Diaz, Z. Qian, A. Alu, and M. Rinaldi, "Plasmonic piezoelectric nanomechanical resonator for spectrally selective infrared sensing," *Nature communications*, vol. 7, no. 1, p. 11249, 2016.

[29] A. Blaikie, D. Miller, and B. J. Alemán, "A fast and sensitive room-temperature graphene nanomechanical bolometer," *Nature communications*, vol. 10, no. 1, p. 4726, 2019.

[30] Y. Zhang, Y. Watanabe, S. Hosono, N. Nagai, and K. Hirakawa, "Room temperature, very sensitive thermometer using a doubly clamped microelectromechanical beam resonator for bolometer applications," *Applied Physics Letters*, vol. 108, no. 16, 2016.

[31] Y. Zhang, S. Hosono, N. Nagai, S.-H. Song, and K. Hirakawa, "Fast and sensitive bolometric terahertz detection at room temperature through thermomechanical transduction," *Journal of Applied Physics*, vol. 125, no. 15, 2019.

[32] L. Vicarelli, A. Tredicucci, and A. Pitanti, "Micromechanical bolometers for subterahertz detection at room temperature," *ACS Photonics*, vol. 9, no. 2, pp. 360–367, 2022.

[33] C. Zhang, M. Giroux, T. A. Nour, and R. St-Gelais, "Thermal radiation sensing using high mechanical Q-factor silicon nitride membranes," in *2019 IEEE SENSORS*, pp. 1–4, oct 2019.

[34] P. Sadeghi, M. Tanzer, N. Luhmann, M. Piller, M.-H. Chien, and S. Schmid, "Thermal transport and frequency response of localized modes on low-stress nanomechanical silicon nitride drums featuring a phononic-band-gap structure," *Physical Review Applied*, vol. 14, no. 2, p. 024068, 2020.

[35] M. Sansa, E. Sage, E. C. Bullard, M. Gély, T. Alava, E. Colinet, A. K. Naik, L. G. Villanueva, L. Duraffourg, M. L. Roukes, *et al.*, "Frequency fluctuations in silicon nanoresonators," *Nature nanotechnology*, vol. 11, no. 6, p. 552, 2016.

[36] A. N. Cleland and M. L. Roukes, "Noise processes in nanomechanical resonators," *J. Appl. Phys.*, vol. 92, pp. 2758–2769, 9 2002.

[37] J. R. Vig and Y. Kim, "Noise in microelectromechanical system resonators," *IEEE transactions on ultrasonics, ferroelectrics, and frequency control*, vol. 46, no. 6, pp. 1558–1565, 1999.

[38] A. Demir, "Understanding fundamental trade-offs in nanomechanical resonant sensors," *Journal of Applied Physics*, vol. 129, no. 4, 2021.

[39] A. Demir and M. S. Hanay, "Fundamental sensitivity limitations of nanomechanical resonant sensors due to thermomechanical noise," *IEEE Sensors Journal*, vol. 20, no. 4, pp. 1947–1961, 2019.

[40] P. Sadeghi, A. Demir, L. G. Villanueva, H. Kähler, and S. Schmid, "Frequency fluctuations in nanomechanical silicon nitride string resonators," *Physical Review B*, vol. 102, no. 21, p. 214106, 2020.

[41] A. Suhel, B. Hauer, T. S. Biswas, K. S. Beach, and J. P. Davis, "Dissipation mechanisms in thermomechanically driven silicon nitride nanostrings," *Applied Physics Letters*, vol. 100, no. 17, 2012.

[42] A. N. Cleland, "Thermomechanical noise limits on parametric sensing with nanomechanical resonators," *New Journal of Physics*, vol. 7, no. 1, p. 235, 2005.

[43] S. K. Roy, V. T. Sauer, J. N. Westwood-Bachman, A. Venkatasubramanian, and W. K. Hiebert, "Improving mechanical sensor performance through larger damping," *Science*, vol. 360, no. 6394, p. eaar5220, 2018.

[44] J. M. Miller, N. E. Bousse, D. B. Heinz, H. J. K. Kim, H.-K. Kwon, G. D. Vukasin, and T. W. Kenny, "Thermomechanical-noise-limited capacitive transduction of encapsulated mem resonators," *Journal of Microelectromechanical Systems*, vol. 28, no. 6, pp. 965–976, 2019.

[45] J. Aldridge and A. Cleland, "Noise-enabled precision measurements of a duffing nanomechanical resonator," *Physical review letters*, vol. 94, no. 15, p. 156403, 2005.

[46] Y. Qiao, A. Elhady, M. Arabi, E. Abdel-Rahman, and W. Zhang, "Thermal noise-driven resonant sensors," *Microsystems & Nanoengineering*, vol. 10, no. 1, p. 90, 2024.

[47] T. Gisler, M. Helal, D. Sabonis, U. Grob, M. Héritier, C. L. Degen, A. H. Ghadimi, and A. Eichler, "Soft-clamped silicon nitride string resonators at millikelvin temperatures," *Physical Review Letters*, vol. 129, no. 10, p. 104301, 2022.

[48] H. Bešić, A. Demir, J. Steurer, N. Luhmann, and S. Schmid, "Schemes for tracking resonance frequency for micro-and nanomechanical resonators," *Physical Review Applied*, vol. 20, no. 2, p. 024023, 2023.

[49] H. Bešić, A. Demir, V. Vukićević, J. Steurer, and S. Schmid, "Adaptable frequency counter with phase filtering for resonance frequency monitoring in nanomechanical sensing," *IEEE Sensors Journal*, 2024.

[50] C. Zhang, M. Giroux, T. A. Nour, and R. St-Gelais, "Radiative heat transfer in free-standing silicon nitride membranes," *Physical Review Applied*, vol. 14, p. 024072, Aug 2020.

[51] M. Piller, N. Luhmann, M.-H. Chien, and S. Schmid, "Nanoelectromechanical infrared detector," in *Optical Sensing, Imaging, and Photon Counting: From X-Rays to THz 2019*, vol. 11088, pp. 9–15, SPIE, 2019.

[52] Q. Wu and X.-C. Zhang, "Free-space electro-optic sampling of terahertz beams," *Applied Physics Letters*, vol. 67, no. 24, pp. 3523–3525, 1995.

[53] A. Nahata, A. S. Weling, and T. F. Heinz, "A wideband coherent terahertz spectroscopy system using optical rectification and electro-optic sampling," *Applied physics letters*, vol. 69, no. 16, pp. 2321–2323, 1996.

[54] N. T. Yardimci and M. Jarrahi, "Nanostructure-enhanced photoconductive terahertz emission and detection," *Small*, vol. 14, no. 44, p. 1802437, 2018.

[55] S. Lepeshov, A. Gorodetsky, A. Krasnok, N. Toropov, T. A. Vartanyan, P. Belov, A. Alú, and E. U. Rafailov, "Boosting terahertz photoconductive antenna performance with optimised plasmonic nanostructures," *Scientific reports*, vol. 8, no. 1, p. 6624, 2018.

[56] H. Minamide, J. Zhang, R. Guo, K. Miyamoto, S. Ohno, and H. Ito, "High-sensitivity detection of terahertz waves using nonlinear up-conversion in an organic 4-dimethylamino-n-methyl-4-stilbazolium tosylate crystal," *Applied Physics Letters*, vol. 97, no. 12, 2010.

[57] A. Graf, M. Arndt, M. Sauer, and G. Gerlach, "Review of micromachined thermopiles for infrared detection," *Measurement Science and Technology*, vol. 18, no. 7, pp. R59–R75, 2007.

[58] T. J. Seebeck, *Magnetische polarisation der metalle und erze durch temperatur-differenz*. No. 70 in Scientific Contributions Series, W. Engelmann, 1895.

[59] X. Zhu, Y. Yu, and F. Li, "A review on thermoelectric energy harvesting from asphalt pavement: Configuration, performance and future," *Construction and Building Materials*, vol. 228, p. 116818, 2019.

[60] A. Van Herwaarden and P. Sarro, "Thermal sensors based on the seebeck effect," *Sensors and Actuators*, vol. 10, no. 3-4, pp. 321–346, 1986.

[61] A. Van Herwaarden, D. Van Duyn, B. Van Oudheusden, and P. Sarro, "Integrated thermopile sensors," *Sensors and Actuators A: Physical*, vol. 22, no. 1-3, pp. 621–630, 1990.

[62] S. B. Mbarek, N. Alcheikh, and M. I. Younis, "Recent advances on mems based infrared thermopile detectors," *Microsystem Technologies*, vol. 28, no. 8, pp. 1751–1764, 2022.

[63] D. White, R. Galleano, A. Actis, H. Brixy, M. De Groot, J. Dubbeldam, A. Reesink, F. Edler, H. Sakurai, R. Shepard, *et al.*, "The status of johnson noise thermometry," *Metrologia*, vol. 33, no. 4, p. 325, 1996.

[64] J. Schieferdecker, R. Quad, E. Holzenkämpfer, and M. Schulze, "Infrared thermopile sensors with high sensitivity and very low temperature coefficient," *Sensors and Actuators A: Physical*, vol. 47, no. 1-3, pp. 422–427, 1995.

[65] S. Allison, R. Smith, D. Howard, C. Gonzalez, and S. Collins, "A bulk micromachined silicon thermopile with high sensitivity," *Sensors and Actuators A: Physical*, vol. 104, no. 1, pp. 32–39, 2003.

[66] R. Buchner, C. Sosna, M. Maiwald, W. Benecke, and W. Lang, "A high-temperature thermopile fabrication process for thermal flow sensors," *Sensors and Actuators A: Physical*, vol. 130, pp. 262–266, 2006.

[67] D. Xu, B. Xiong, and Y. Wang, "Design, fabrication and characterization of a front-etched micromachined thermopile for ir detection," *Journal of Micromechanics and Microengineering*, vol. 20, no. 11, p. 115004, 2010.

[68] J. Martin, T. Tritt, and C. Uher, "High temperature seebeck coefficient metrology," *Journal of Applied Physics*, vol. 108, no. 12, 2010.

[69] F. Völklein, "Review of the thermoelectric efficiency of bulk and thin-film materials," *Sensors and Materials*, vol. 8, pp. 389–408, 1996.

[70] A. L. Hsu, P. K. Herring, N. M. Gabor, S. Ha, Y. C. Shin, Y. Song, M. Chin, M. Dubey, A. P. Chandrakasan, J. Kong, *et al.*, "Graphene-based thermopile for thermal imaging applications," *Nano letters*, vol. 15, no. 11, pp. 7211–7216, 2015.

[71] B. C. St-Antoine, D. Ménard, and R. Martel, "Single-walled carbon nanotube thermopile for broadband light detection," *Nano letters*, vol. 11, no. 2, pp. 609–613, 2011.

[72] M. C. Nguyen, V. H. Nguyen, H.-V. Nguyen, J. Saint-Martin, and P. Dollfus, "Enhanced seebeck effect in graphene devices by strain and doping engineering," *Physica E: Low-dimensional Systems and Nanostructures*, vol. 73, pp. 207–212, 2015.

[73] T. A. Amollo, G. T. Mola, M. Kirui, and V. O. Nyamori, "Graphene for thermoelectric applications: prospects and challenges," *Critical Reviews in Solid State and Materials Sciences*, vol. 43, no. 2, pp. 133–157, 2018.

[74] H. Bark, W. Lee, and H. Lee, "Correlation between seebeck coefficients and electronic structures of nitrogen-or boron-doped reduced graphene oxide via thermally activated carrier transport," *Journal of Materials Chemistry A*, vol. 6, no. 32, pp. 15577–15584, 2018.

[75] A. A. Balandin, S. Ghosh, W. Bao, I. Calizo, D. Teweldebrhan, F. Miao, and C. N. Lau, "Superior thermal conductivity of single-layer graphene," *Nano letters*, vol. 8, no. 3, pp. 902–907, 2008.

[76] K. J. Erikson, X. He, A. A. Talin, B. Mills, R. H. Hauge, T. Iguchi, N. Fujimura, Y. Kawano, J. Kono, and F. Léonard, "Figure of merit for carbon nanotube photothermoelectric detectors," *ACS nano*, vol. 9, no. 12, pp. 11618–11627, 2015.

[77] R. Whatmore, "Pyroelectric devices and materials," *Reports on progress in physics*, vol. 49, no. 12, p. 1335, 1986.

[78] J. Zook and S. Liu, "Pyroelectric effects in thin film," *Journal of Applied Physics*, vol. 49, no. 8, pp. 4604–4606, 1978.

[79] D. Zhang, H. Wu, C. R. Bowen, and Y. Yang, "Recent advances in pyroelectric materials and applications," *Small*, vol. 17, no. 51, p. 2103960, 2021.

[80] D. Lingam, A. R. Parikh, J. Huang, A. Jain, and M. Minary-Jolandan, "Nano/microscale pyroelectric energy harvesting: challenges and opportunities," *International Journal of Smart and Nano Materials*, vol. 4, no. 4, pp. 229–245, 2013.

[81] E. Putley, "The pyroelectric detector," in *Semiconductors and Semimetals*, vol. 5, pp. 259–285, Elsevier, 1970.

[82] S. PORTER, "A brief guide to pyroelectric detectors," *SPIE milestone series*, vol. 179, pp. 49–62, 2004.

[83] M. Aleks, C. Jagtap, V. Kadam, G. Kolev, K. Denishev, H. Pathan, *et al.*, "An overview of microelectronic infrared pyroelectric detector," *Engineered Science*, vol. 16, pp. 82–89, 2021.

[84] Z. Liu, T. Lu, X. Dong, G. Wang, and Y. Liu, "Ferroelectric ceramics for pyroelectric detection applications: A review," *IEEE Transactions on Ultrasonics, Ferroelectrics, and Frequency Control*, vol. 68, no. 2, pp. 242–252, 2020.

[85] A. Hossain and M. Rashid, "Pyroelectric detectors and their applications," *IEEE Transactions on Industry Applications*, vol. 27, no. 5, pp. 824–829, 1991.

[86] D. M. Dodd, "The infrared absorption characteristics of ferroelectric triglycine sulfate," *Spectrochimica Acta*, vol. 15, pp. 1072–1084, 1959.

[87] R. Smith and F. Welsh, "Temperature dependence of the elastic, piezoelectric, and dielectric constants of lithium tantalate and lithium niobate," *Journal of applied physics*, vol. 42, no. 6, pp. 2219–2230, 1971.

[88] W. Cook Jr, D. Berlincourt, and F. Scholz, "Thermal expansion and pyroelectricity in lead titanate zirconate and barium titanate," *Journal of Applied Physics*, vol. 34, no. 5, pp. 1392–1398, 1963.

[89] S. Aravazhi, R. Jayavel, and C. Subramanian, "Growth and stability of pure and amino doped tgs crystals," *Materials chemistry and physics*, vol. 50, no. 3, pp. 233–237, 1997.

[90] LASER COMPONENTS, "Pyroelectric DLaTGS detectors." `https://www.lasercomponents.com/en/product/pyroelectric-dlatgs-detectors/`, 2024. Accessed: 2024-10-12.

[91] Gentec-EO, "Thz5i-bl-bnc pyroelectric sensors." `https://www.gentec-eo.com/products/thz5i-bl-bnc`, 2024. Accessed: 2025-05-14.

[92] J. Lehman, E. Theocharous, G. Eppeldauer, and C. Pannell, "Gold-black coatings for freestanding pyroelectric detectors," *Measurement Science and Technology*, vol. 14, no. 7, p. 916, 2003.

[93] S. A. Kuznetsov, A. G. Paulish, M. Navarro-Cía, and A. V. Arzhannikov, "Selective pyroelectric detection of millimetre waves using ultra-thin metasurface absorbers," *Scientific reports*, vol. 6, no. 1, pp. 1–11, 2016.

[94] T. D. Dao, S. Ishii, T. Yokoyama, T. Sawada, R. P. Sugavaneshwar, K. Chen, Y. Wada, T. Nabatame, and T. Nagao, "Hole array perfect absorbers for spectrally selective midwavelength infrared pyroelectric detectors," *Acs Photonics*, vol. 3, no. 7, pp. 1271–1278, 2016.

[95] J. W. Stewart, J. H. Vella, W. Li, S. Fan, and M. H. Mikkelsen, "Ultrafast pyroelectric photodetection with on-chip spectral filters," *Nature materials*, vol. 19, no. 2, pp. 158–162, 2020.

[96] J. Y. Suen, K. Fan, J. Montoya, C. Bingham, V. Stenger, S. Sriram, and W. J. Padilla, "Multifunctional metamaterial pyroelectric infrared detectors," *Optica*, vol. 4, no. 2, pp. 276–279, 2017.

[97] R. C. Jones, "The general theory of bolometer performance," *JOSA*, vol. 43, no. 1, pp. 1–14, 1953.

[98] S. P. Langley, "The bolometer and radiant energy," in *Proceedings of the American Academy of Arts and Sciences*, vol. 16, pp. 342–358, JSTOR, 1880.

[99] F. J. Low, "Low-temperature germanium bolometer," *JOSA*, vol. 51, no. 11, pp. 1300–1304, 1961.

[100] IRLabs, "Bolometers." `https://www.irlabs.com/products/bolometers/`, 2024. Accessed: 2024-10-12.

[101] R. Wood, C. Han, and P. Kruse, "Integrated uncooled ir detector imaging arrays, solid-state sensor and actuator workshop," *Proceedings of the 5th Technical Digest IEEE, Piscataway, NJ, USA*, pp. 22–25, 1992.

[102] Y.-H. Han, I.-H. Choi, H.-K. Kang, J.-Y. Park, K.-T. Kim, H.-J. Shin, and S. Moon, "Fabrication of vanadium oxide thin film with high-temperature coefficient of resistance using v2o5/v/v2o5 multi-layers for uncooled microbolometers," *Thin Solid Films*, vol. 425, no. 1-2, pp. 260–264, 2003.

[103] H. Jerominek, F. Picard, N. R. Swart, M. Renaud, M. Levesque, M. Lehoux, J.-S. Castonguay, M. Pelletier, G. Bilodeau, D. Audet, *et al.*, "Micromachined uncooled vo2-based ir bolometer arrays," in *Infrared Detectors and Focal Plane Arrays IV*, vol. 2746, pp. 60–71, SPIE, 1996.

[104] P. Norton and J. Brandt, "Temperature coefficient of resistance for p-and n-type silicon," *Solid-state electronics*, vol. 21, no. 7, pp. 969–974, 1978.

[105] W. Bullis, F. Brewer, C. Kolstad, and L. Swartzendruber, "Temperature coefficient of resistivity of silicon and germanium near room temperature," *Solid-State Electronics*, vol. 11, no. 7, pp. 639–646, 1968.

[106] F. Warkusz, "The size effect and the temperature coefficient of resistance in thin films," *Journal of Physics D: Applied Physics*, vol. 11, no. 5, p. 689, 1978.

[107] P. K. Yadav, I. Yadav, B. Ajitha, A. Rajasekar, S. Gupta, and Y. A. K. Reddy, "Advancements of uncooled infrared microbolometer materials: A review," *Sensors and Actuators A: Physical*, vol. 342, p. 113611, 2022.

[108] B. Wang, J. Lai, E. Zhao, H. Hu, Q. Liu, and S. Chen, "Vanadium oxide microbolometer with gold black absorbing layer," *Optical Engineering*, vol. 51, no. 7, pp. 074003–074003, 2012.

[109] P. Renoux, S. Æ. Jónsson, L. J. Klein, H. F. Hamann, and S. Ingvarsson, "Sub-wavelength bolometers: Uncooled platinum wires as infrared sensors," *Optics express*, vol. 19, no. 9, pp. 8721–8727, 2011.

[110] Hamamatsu Photonics, "Infrared detectors." `https://www.hamamatsu.com/eu/en/product/optical-sensors/infrared-detector.html`, 2024. Accessed: 2024-10-24.

[111] F. Yi, H. Zhu, J. C. Reed, and E. Cubukcu, "Plasmonically enhanced thermomechanical detection of infrared radiation," *Nano letters*, vol. 13, no. 4, pp. 1638–1643, 2013.

[112] H. Chen, Z.-F. Zhao, W.-J. Li, Z.-D. Cheng, J.-J. Suo, B.-L. Li, M.-L. Guo, B.-Y. Fan, Q. Zhou, Y. Wang, *et al.*, "Gate-tunable bolometer based on strongly coupled graphene mechanical resonators," *Optics Letters*, vol. 48, no. 1, pp. 81–84, 2022.

[113] X. Zou, S. Ahmed, N. Jaber, and H. Fariborzi, "High-sensitivity thermal sensing based on a single strain-assisted resonator," *IEEE Sensors Journal*, vol. 22, no. 14, pp. 13921–13929, 2022.

[114] P. Martini, K. Kanellopulos, S. Emminger, N. Luhmann, M. Piller, R. G. West, and S. Schmid, "Uncooled thermal infrared detection near the fundamental limit using a silicon nitride nanomechanical resonator with a broadband absorber," *Communications Physics*, vol. 8, no. 1, p. 166, 2025.

[115] W. P. Robins, *Phase noise in signal sources: theory and applications*, vol. 9. IET, 1984.

[116] D. J. Inman, *Engineering Vibration*. Boston: Pearson, 4th ed., 2013.

[117] L. D. Landau and E. M. Lifshitz, *Statistical Physics: Volume 5*, vol. 5. Elsevier, 2013.

[118] C. Reinhardt, *Ultralow-noise silicon nitride trampoline resonators for sensing and optomechanics*. McGill University (Canada), 2017.

[119] D. J. Wilson, *Cavity optomechanics with high-stress silicon nitride films*. California Institute of Technology, 2012.

[120] A. Demir, "Understanding fundamental trade-offs in nanomechanical resonant sensors," *J. Appl. Phys.*, vol. 129, no. 4, p. 044503, 2021.

[121] P. Sadeghi, A. Demir, L. G. Villanueva, H. Kähler, and S. Schmid, "Frequency fluctuations in nanomechanical silicon nitride string resonators," *Phys. Rev. B*, vol. 102, no. 21, p. 214106, 2020.

[122] L. G. Villanueva and S. Schmid, "Evidence of surface loss as ubiquitous limiting damping mechanism in sin micro- and nanomechanical resonators," *Phys. Rev. Lett.*, vol. 113, p. 227201, Nov 2014.

[123] S. Chakram, Y. S. Patil, L. Chang, and M. Vengalattore, "Dissipation in ultrahigh quality factor sin membrane resonators," *Phys. Rev. Lett.*, vol. 112, p. 127201, Mar 2014.

[124] M. Yuan, M. A. Cohen, and G. A. Steele, "Silicon nitride membrane resonators at millikelvin temperatures with quality factors exceeding 108," *Applied Physics Letters*, vol. 107, no. 26, 2015.

[125] P. L. Yu, T. P. Purdy, and C. A. Regal, "Control of material damping in High-Q membrane microresonators," *Physical Review Letters*, vol. 108, no. 8, pp. 1–5, 2012.

[126] I. Wilson-Rae, R. Barton, S. Verbridge, D. Southworth, B. Ilic, H. G. Craighead, and J. Parpia, "High-q nanomechanics via destructive interference of elastic waves," *Physical review letters*, vol. 106, no. 4, p. 047205, 2011.

[127] W. D. Callister and D. G. Rethwisch, *Materials science and engineering: an introduction*. Wiley New York, 1999.

[128] L. G. Villanueva and S. Schmid, "Evidence of surface loss as ubiquitous limiting damping mechanism in sin micro-and nanomechanical resonators," *Physical review letters*, vol. 113, no. 22, p. 227201, 2014.

[129] B. Zwickl, W. Shanks, A. Jayich, C. Yang, A. Bleszynski Jayich, J. Thompson, and J. Harris, "High quality mechanical and optical properties of commercial silicon nitride membranes," *Applied Physics Letters*, vol. 92, no. 10, 2008.

[130] G. Cagnoli, J. Hough, D. DeBra, M. Fejer, E. Gustafson, S. Rowan, and V. Mitrofanov, "Damping dilution factor for a pendulum in an interferometric gravitational waves detector," *Physics Letters A*, vol. 272, no. 1-2, pp. 39–45, 2000.

[131] S. Schmid, K. Jensen, K. Nielsen, and A. Boisen, "Damping mechanisms in high-q micro and nanomechanical string resonators," *Physical Review B—Condensed Matter and Materials Physics*, vol. 84, no. 16, p. 165307, 2011.

[132] E. Ventsel, T. Krauthammer, and E. Carrera, "Thin plates and shells: theory, analysis, and applications," *Appl. Mech. Rev.*, vol. 55, no. 4, pp. B72–B73, 2002.

[133] M. Kurek, M. Carnoy, P. E. Larsen, L. H. Nielsen, O. Hansen, T. Rades, S. Schmid, and A. Boisen, "Nanomechanical infrared spectroscopy with vibrating filters for pharmaceutical analysis," *Angewandte Chemie*, vol. 129, no. 14, pp. 3959–3963, 2017.

[134] C. Zhang, M. Giroux, T. A. Nour, and R. St-Gelais, "Radiative Heat Transfer in Freestanding Silicon Nitride Membranes," *Phys. Rev. Applied*, vol. 14, p. 024072, 2020.

[135] T. L. Bergman, F. P. Incropera, D. P. DeWitt, and A. S. Lavine, *Fundamentals of heat and mass transfer*. John Wiley & Sons, 2011.

[136] C. Zhang and R. St-Gelais, "Demonstration of frequency stability limited by thermal fluctuation noise in silicon nitride nanomechanical resonators," *Applied Physics Letters*, vol. 122, no. 19, 2023.

[137] E. W. Weisstein, "Modified bessel function of the first kind," *https://mathworld. wolfram. com/*, 2002.

[138] C. Zhang, E. K. Yalavarthi, M. Giroux, W. Cui, M. Stephan, A. Maleki, A. Weck, J.-M. Ménard, and R. St-Gelais, "High detectivity terahertz radiation sensing using frequency-noise-optimized nanomechanical resonators," *APL Photonics*, vol. 9, no. 12, 2024.

[139] W. P. Robins, *Phase Noise in Signal Sources*. IET, Edison, NJ, 1984.

[140] I. Kovacic and M. J. Brennan, *The Duffing equation: nonlinear oscillators and their behaviour*. John Wiley & Sons, 2011.

[141] R. Lifshitz and M. C. Cross, "Nonlinear dynamics of nanomechanical and micromechanical resonators," *Reviews of nonlinear dynamics and complexity*, vol. 1, no. 1, 2008.

[142] H. Postma, I. Kozinsky, A. Husain, and M. Roukes, "Dynamic range of nanotube- and nanowire-based electromechanical systems," *Applied Physics Letters*, vol. 86, no. 22, 2005.

[143] T. Manzaneque, M. K. Ghatkesar, F. Alijani, M. Xu, R. A. Norte, and P. G. Steeneken, "Resolution limits of resonant sensors," *Physical Review Applied*, vol. 19, no. 5, p. 054074, 2023.

[144] D. Allan, "Statistics of atomic frequency standards," *Proc. IEEE*, vol. 54, p. 221, 1966.

[145] J. Chaste, A. Eichler, J. Moser, G. Ceballos, R. Rurali, and A. Bachtold, "A nanomechanical mass sensor with yoctogram resolution," *Nat. Nanotechnol.*, vol. 7, p. 301, 2012.

[146] M. S. Hanay, S. Kelber, A. K. Naik, D. Chi, S. Hentz, E. C. Bullard, E. Colinet, L. Duraffourg, and M. L. Roukes, "Single-protein nanomechanical mass spectrometry in real time," *Nat. Nanotechnol.*, vol. 7, p. 602, 2012.

[147] E. Buks and B. Yurke, "Mass detection with a nonlinear nanomechanical resonator," *Phys. Rev. E*, vol. 74, p. 046619, 2006.

[148] M. M. Daryani, T. Manzaneque, J. Wei, and M. K. Ghatkesar, "Measuring nanoparticles in liquid with attogram resolution using a microfabricated glass suspended microchannel resonator," *Microsyst Nanoeng*, vol. 8, p. 92, 2022.

[149] J. Moser, J. Güttinger, A. Eichler, M. J. Esplandiu, D. E. Liu, M. I. Dykman, and A. Bachtold, "Ultrasensitive force detection with a nanotube mechanical resonator," *Nat. Nanotechnol.*, vol. 8, no. 7, p. 493, 2013.

[150] D. Hälg, T. Gisler, Y. Tsaturyan, L. Catalini, U. Grob, M.-D. Krass, M. Héritier, H. Mattiat, A.-K. Thamm, R. Schirhagl, E. C. Langman, A. Schliesser, C. L. Degen, and A. Eichler, "Membrane-Based Scanning Force Microscopy," *Phys. Rev. Applied*, vol. 15, no. 2, p. L021001, 2021.

[151] M. Piller, P. Sadeghi, R. G. West, N. Luhmann, P. Martini, O. Hansen, and S. Schmid, "Thermal radiation dominated heat transfer in nanomechanical silicon nitride drum resonators," *Appl. Phys. Lett.*, vol. 117, p. 034101, 2020.

[152] A. Blaikie, D. Miller, and B. J. Alemán, "A fast and sensitive room-temperature graphene nanomechanical bolometer," *Nat. Commun.*, vol. 10, p. 4726, 2019.

[153] X. C. Zhang, E. B. Myers, J. E. Sader, and M. L. Roukes, "Nanomechanical Torsional Resonators for Frequency-Shift Infrared Thermal Sensing," *Nano Lett.*, vol. 13, pp. 1528–1534, 2013.

[154] Y. Zhang, S. Hosono, N. Nagai, S.-H. Song, and K. Hirakawa, "Fast and sensitive bolometric terahertz detection at room temperature through thermomechanical transduction," *J. Appl. Phys.*, vol. 125, p. 151602, 2019.

[155] L. Laurent, J.-J. Yon, J.-S. Moulet, M. Roukes, and L. Duraffourg, "12-μm-Pitch Electromechanical Resonator for Thermal Sensing," *Phys. Rev. Applied*, vol. 9, p. 024016, 2018.

[156] J. R. Vig and Y. Kim, "Noise in microelectromechanical system resonators," *IEEE Trans. Ultrason. Ferroelectr. Freq. Control*, vol. 46, p. 1558, 1999.

[157] M. Sansa, E. Sage, E. C. Bullard, M. Gély, T. Alava, E. Colinet, A. K. Naik, L. G. Villanueva, L. Duraffourg, M. L. Roukes, G. Jourdan, and S. Hentz, "Frequency fluctuations in silicon nanoresonators," *Nat. Nanotechnol.*, vol. 11, no. 6, pp. 552–558, 2016.

[158] S. K. Roy, V. T. K. Sauer, J. N. Westwood-Bachman, A. Venkatasubramanian, and W. K. Hiebert, "Improving mechanical sensor performance through larger damping," *Science*, vol. 360, no. 6394, p. 1203, 2018.

[159] J. M. L. Miller, N. E. Bousse, D. B. Heinz, H. J. K. Kim, H.-K. Kwon, G. D. Vukasin, and T. W. Kenny, "Thermomechanical-Noise-Limited Capacitive Transduction of Encapsulated MEM Resonators," *J. Microelectromechanical Syst.*, vol. 28, p. 965, 2019.

[160] A. N. Cleland, "Thermomechanical noise limits on parametric sensing with nanomechanical resonators," *New J. Phys.*, vol. 7, p. 235, 2005.

[161] N. Snell, C. Zhang, G. Mu, A. Bouchard, and R. St-Gelais, "Heat Transport in Silicon Nitride Drum Resonators and its Influence on Thermal Fluctuation-Induced Frequency Noise," *Phys. Rev. Applied*, vol. 17, p. 044019, 2022.

[162] J. Zhou, N. Moldovan, L. Stan, H. Cai, D. A. Czaplewski, and D. López, "Approaching the strain-free limit in ultrathin nanomechanical resonators," *Nano letters*, vol. 20, no. 8, pp. 5693–5698, 2020.

[163] A. Rogalski, *Infrared detectors*. CRC press, 2000.

[164] K. Kanellopulos, F. Ladinig, S. Emminger, P. Martini, R. G. West, and S. Schmid, "Comparative analysis of nanomechanical resonators: sensitivity, response time, and practical considerations in photothermal sensing," *Microsystems & Nanoengineering*, vol. 11, no. 1, p. 28, 2025.

[165] X. Xie, R. Nikbakht, M. Couillard, R. St-Gelais, and A. Weck, "Laser machining of free-standing silicon nitride membranes," *Journal of Materials Processing Technology*, vol. 318, p. 118001, 2023.

[166] R. Nikbakht, X. Xie, A. Weck, and R. St-Gelais, "High quality factor silicon nitride nanomechanical resonators fabricated by maskless femtosecond laser micromachining," *Journal of Vacuum Science & Technology B*, vol. 41, no. 2, 2023.

[167] L. Laurent, J.-J. Yon, J.-S. Moulet, M. Roukes, and L. Duraffourg, "12- μ m-pitch electromechanical resonator for thermal sensing," *Phys. Rev. Appl.*, vol. 9, no. 2, p. 024016, 2018.

[168] M. Piller, P. Sadeghi, R. G. West, N. Luhmann, P. Martini, O. Hansen, and S. Schmid, "Thermal radiation dominated heat transfer in nanomechanical silicon nitride drum resonators," *Appl. Phys. Lett.*, vol. 117, no. 3, 2020.

[169] X. Zhang, E. Myers, J. Sader, and M. Roukes, "Nanomechanical torsional resonators for frequency-shift infrared thermal sensing," *Nano Lett.*, vol. 13, no. 4, pp. 1528–1534, 2013.

[170] C. Zhang, M. Giroux, T. A. Nour, and R. St-Gelais, "Radiative heat transfer in freestanding silicon nitride membranes," *Phys. Rev. Appl.*, vol. 14, no. 2, p. 024072, 2020.

[171] M. Piller, J. Hiesberger, E. Wistrela, P. Martini, N. Luhmann, and S. Schmid, "Thermal ir detection with nanoelectromechanical silicon nitride trampoline resonators," *IEEE Sens. J.*, vol. 23, no. 2, pp. 1066–1071, 2022.

[172] Y. Hui, J. S. Gomez-Diaz, Z. Qian, A. Alu, and M. Rinaldi, "Plasmonic piezoelectric nanomechanical resonator for spectrally selective infrared sensing," *Nat. Commun.*, vol. 7, no. 1, p. 11249, 2016.

[173] A. Blaikie, D. Miller, and B. J. Alemán, "A fast and sensitive room-temperature graphene nanomechanical bolometer," *Nat. Commun.*, vol. 10, no. 1, p. 4726, 2019.

[174] Y. Zhang, Y. Watanabe, S. Hosono, N. Nagai, and K. Hirakawa, "Room temperature, very sensitive thermometer using a doubly clamped microelectromechanical beam resonator for bolometer applications," *Appl. Phys. Lett.*, vol. 108, no. 16, 2016.

[175] Y. Zhang, S. Hosono, N. Nagai, S.-H. Song, and K. Hirakawa, "Fast and sensitive bolometric terahertz detection at room temperature through thermomechanical transduction," *J. Appl. Phys.*, vol. 125, no. 15, 2019.

[176] L. Vicarelli, A. Tredicucci, and A. Pitanti, "Micromechanical bolometers for subterahertz detection at room temperature," *ACS photonics*, vol. 9, no. 2, pp. 360–367, 2022.

[177] S. K. Roy, V. T. Sauer, J. N. Westwood-Bachman, A. Venkatasubramanian, and W. K. Hiebert, "Improving mechanical sensor performance through larger damping," *Science*, vol. 360, no. 6394, p. eaar5220, 2018.

[178] M. Sansa, E. Sage, E. C. Bullard, M. Gély, T. Alava, E. Colinet, A. K. Naik, L. G. Villanueva, L. Duraffourg, M. L. Roukes, *et al.*, "Frequency fluctuations in silicon nanoresonators," *Nat. Nanotechnol.*, vol. 11, no. 6, pp. 552–558, 2016.

[179] P. Sadeghi, A. Demir, L. G. Villanueva, H. Kähler, and S. Schmid, "Frequency fluctuations in nanomechanical silicon nitride string resonators," *Phys. Rev. B*, vol. 102, no. 21, p. 214106, 2020.

[180] N. Snell, C. Zhang, G. Mu, A. Bouchard, and R. St-Gelais, "Heat transport in silicon nitride drum resonators and its influence on thermal fluctuation-induced frequency noise," *Phys. Rev. Appl.*, vol. 17, no. 4, p. 044019, 2022.

[181] C. Zhang and R. St-Gelais, "Demonstration of frequency stability limited by thermal fluctuation noise in silicon nitride nanomechanical resonators," *Appl. Phys. Lett.*, vol. 122, no. 19, 2023.

[182] R. Lewis, "A review of terahertz detectors," *J. Phys. D*, vol. 52, no. 43, p. 433001, 2019.

[183] "Thz5i-bl-bnc - terahertz power detector." `https://www.gentec-eo.com/products/thz5i-bl-bnc.`, 2024.

[184] "Tydex golay detectors." `https://www.tydexoptics.com/products/thz_devices/golay_cell/.`, 2024.

[185] A. Demir and M. S. Hanay, "Fundamental sensitivity limitations of nanomechanical resonant sensors due to thermomechanical noise," *IEEE Sens. J.*, vol. 20, no. 4, pp. 1947–1961, 2019.

[186] J. R. Vig and Y. Kim, "Noise in microelectromechanical system resonators," *IEEE Trans Ultrason Ferroelectr Freq Control*, vol. 46, no. 6, pp. 1558–1565, 1999.

[187] A. Cleland and M. Roukes, "J. appl. phys.," *Journal of applied physics*, vol. 92, no. 5, pp. 2758–2769, 2002.

[188] S. Schmid, L. G. Villanueva, and M. L. Roukes, *Fundamentals of nanomechanical resonators*, vol. 49. Springer, 2016.

[189] P.-L. Yu, T. Purdy, and C. Regal, "Control of material damping in high-q membrane microresonators," *Phys. Rev. Lett.*, vol. 108, no. 8, p. 083603, 2012.

[190] B. Zwickl, W. Shanks, A. Jayich, C. Yang, A. Bleszynski Jayich, J. Thompson, and J. Harris, "High quality mechanical and optical properties of commercial silicon nitride membranes," *Applied Physics Letters*, vol. 92, no. 10, 2008.

[191] F. Yang, M. Fu, B. Bosnjak, R. H. Blick, Y. Jiang, and E. Scheer, "Mechanically modulated sideband and squeezing effects of membrane resonators," *Physical Review Letters*, vol. 127, no. 18, p. 184301, 2021.

[192] P. Martini, K. Kanellopulos, and S. Schmid, "Towards photon-noise limited thermal ir detection with optomechanical resonators," in *2023 IEEE SENSORS*, pp. 1–4, IEEE, 2023.

[193] K. Kanellopulos, R. G. West, S. Emminger, P. Martini, M. Sauer, A. Foelske, and S. Schmid, "Stress-dependent optical extinction in low-pressure chemical vapor deposition silicon nitride measured by nanomechanical photothermal sensing," *Nano Letters*, 2024.

[194] G. Mu, N. Snell, C. Zhang, X. Xie, R. Tahvildari, A. Weck, M. Godin, and R. St-Gelais, "Remote actuation of silicon nitride nanomechanical resonators using on-chip substrate capacitors," *J Microelectromech Syst*, vol. 32, no. 1, pp. 29–36, 2022.

[195] A. Bouchard, T. Hodges, M. Stephan, L. Wu, T. Koukoulas, R. G. Green, and R. St-Gelais, "Thermal gradients integrated on-chip by passive radiative cooling of silicon nitride nanomechanical resonators," *Appl. Therm. Eng.*, vol. 229, p. 120561, 2023.

[196] D. Rugar, H. J. Mamin, and P. Guethner, "Improved fiber-optic interferometer for atomic force microscopy," *Appl. Phys. Lett.*, vol. 55, no. 25, pp. 2588–2590, 1989.

[197] W. Cui, K. M. Awan, R. Huber, K. Dolgaleva, and J.-M. Ménard, "Broadband and high-sensitivity time-resolved thz system using grating-assisted tilted-pulse-front phase matching," *Adv. Opt. Mater.*, vol. 10, no. 1, p. 2101136, 2022.

[198] H. Sun, J. Liu, C. Zhou, W. Yang, H. Liu, X. Zhang, Z. Li, B. Zhang, W. Jie, and Y. Xu, "Enhanced transmission from visible to terahertz in znte crystals with scalable subwavelength structures," *ACS Appl. Mater. Interfaces*, vol. 13, no. 14, pp. 16997–17005, 2021.

[199] A. Varpula, K. Tappura, J. Tiira, K. Grigoras, O.-P. Kilpi, K. Sovanto, J. Ahopelto, and M. Prunnila, "Nano-thermoelectric infrared bolometers," *APL Photonics*, vol. 6, no. 3, 2021.

[200] A. Das, M. L. Mah, J. Hunt, and J. J. Talghader, "Thermodynamically limited uncooled infrared detector using an ultra-low mass perforated subwavelength absorber," *Optica*, vol. 10, no. 8, pp. 1018–1028, 2023.